Self-Consistent Study of Topological Superconductivity in Two-Dimensional Quasicrystals

A thesis submitted to the
College of Graduate and Postdoctoral Studies
in partial fulfillment of the requirements
for the dual Master of Science program
in the Department of Physics and Engineering Physics
University of Saskatchewan, Saskatoon
and the Department of Applied Physics, Graduate School of Science
Tokyo University of Science, Tokyo, Japan

By
Masahiro Hori

Permission to Use

In presenting this thesis in partial fulfillment of the requirements for a Postgraduate degree from the University of Saskatchewan, I agree that the Libraries of this University may make it freely available for inspection. I further agree that permission for copying of this thesis in any manner, in whole or in part, for scholarly purposes may be granted by the professor or professors who supervised my thesis work or, in their absence, by the Head of the Department or the Dean of the College in which my thesis work was done. It is understood that any copying or publication or use of this thesis or parts thereof for financial gain shall not be allowed without my written permission. It is also understood that due recognition shall be given to me and to the University of Saskatchewan in any scholarly use which may be made of any material in my thesis.

Disclaimer

Reference in this thesis to any specific commercial products, process, or service by trade name, trademark, manufacturer, or otherwise, does not constitute or imply its endorsement, recommendation, or favoring by the University of Saskatchewan. The views and opinions of the author expressed herein do not state or reflect those of the University of Saskatchewan, and shall not be used for advertising or product endorsement purposes.

Requests for permission to copy or to make other uses of materials in this thesis in whole or part should be addressed to:

Head of the Department of Physics and Engineering Physics
116 Science Place, Rm 163
University of Saskatchewan
Saskatoon, Saskatchewan
Canada
S7N 5E2

OR

Dean
College of Graduate and Postdoctoral Studies
University of Saskatchewan
116 Thorvaldson Building, 110 Science Place
Saskatoon, Saskatchewan S7N 5C9 Canada

Abstract

In the past several years, there has been a burst of theoretical and experimental activities in the field of topological superconductors. Topological superconductivity (TSC) results in a novel superconducting state characterized by a nonzero topological invariant in the bulk. There is a relation between the bulk and edges or surfaces, which is called the bulk-edge correspondence. The bulk-edge correspondence implies that the topological invariant in the bulk is equivalent to the number of zero-energy excitations per edge or surface. Due to particle-hole symmetry inherent in a superconductor, in the case of TSC, the edge or surface modes in a topological superconductor are zero-energy Majorana fermions. Majorana fermions are their own antiparticles and due to the non-Abelian exchange statistics that they obey, they open the door to new and powerful methods of topological quantum computing. Majorana fermions have been detected, e.g., along the edges of a two-dimensional topological superconductor. Theoretically, so far TSC has only been studied in periodic crystals such as square lattice systems. In such systems with translational symmetry, the superconducting order parameter is uniformly distributed.

Motivated by the recent discovery of superconductivity in a quasicrystal (QC), we investigate the occurrence of TSC in two-dimensional QCs. Although QCs present Bragg peaks, they have no periodicity. We generalize a tight-binding model for TSC in two dimensions, which was originally proposed for square lattice systems, for QCs. As the most fundamental examples, the Penrose and Ammann-Beenker QCs are studied. QCs are inherently fractal, and characterized by self-similarity. It is interesting to ask whether a stable TSC phase can exist in QCs, despite their aperiodic and fractal structure.

In this thesis, we solve the Bogoliubov-de Gennes (BdG) equations — coupled Schrödinger-like equations for the electron and hole components of quasiparticle excitation — on the tight-binding model for TSC generalized for QCs. This model describes two-dimensional TSC with broken time-reversal symmetry, whose topological nature is governed by the first Chern number in periodic systems. For QCs, we calculate the Bott index as the topological invariant of the system, which is equivalent to the first Chern number in the presence of translational symmetry. The mean-field approximation is applied to the model Hamilto-

nian of TSC and the superconducting order parameter as well as the spin-dependent Hartree potential are obtained self-consistently.

Our numerical results confirm the existence of a stable TSC state in QCs and the appearance of a Majorana zero mode along edges of a QC, despite the lack of translational symmetry. However, we find that the self-consistently obtained mean fields are both spatially inhomogeneous. In particular, we examine how the underlying aperiodic structure of a QC is reflected in the superconducting order parameter.

Acknowledgements

I am deeply grateful to my supervisor Prof. Kaori Tanaka. Without her tremendous support, it was not possible to continue the research and finish writing this thesis. Because of the coronavirus crisis, my life at the University of Saskatchewan as a master's student was not following the regular style. Especially, I could never visit the University of Saskatchewan even once and I stay in Japan. Accordingly, there were many obstacles to continuing the research, such as the time difference between Japan and Canada, the difficulties of the research discussion on the web, and I could not work as a teaching assistant, etc. Even in such an irregular situation, she flexibly supports my research. In addition, I appreciate that she dedicated her tremendous efforts to realizing the dual master's degree program between the University of Saskatchewan and Tokyo University of Science, Japan.

I also wish to thank my committee members Prof. Glenn Hussey, Prof. Tom Steele, and Dr. Lenaic Couedel, and the external examiner Dr. Steven Rayan for their contributions. I am also grateful to Prof. Takami Tohyama, Dr. Takanori Sugimoto, Dr. Rasoul Ghadimi for supporting my research at Tokyo University of Science, Japan.

For my parents, Mitsuo and Chieko Hori.

Contents

List of Tables

List of Figures

List of Abbreviations

AB	Ammann-Beenker
BCS	Bardeen-Cooper-Schriefer
BdG	Bogoliubov-de Gennes
DOS	density of states
OBC	open boundary condition
PBC	periodic boundary condition
QC	quasicrystal
SC	superconductivity
TSC	topological superconductivity

1 Introduction

1.1 Topological Insulators and Topological Superconductors

Topological insulating behavior and topological superconductivity (TSC) [1, 2, 3] are two of the most fundamental topological quantum phenomena. Recently, these topological quantum phenomena have been paid intensive attention in the field of materials science. A piece of supporting evidence is that the founders of this research area were awarded the Nobel Prize in Physics in 2016 [4]. As a first example, topological insulators are unconventional insulators, whose interior is an insulator while the surface is a conductor [5, 6]. An example of the topological insulator is $(Bi_{1-x}Sb_x)_2Te_3$ thin films, where a current without energy loss has been experimentally observed [7]. In analysis of the wave functions of electrons, the concept of topology is imported from mathematics and is made good use of [8, 9]. The topological insulating phase can be explained in terms of nontrivial topology associated with the occupied single-electron states. The second example, TSC, results in a novel superconducting state also characterized by a nonzero topological invariant in the bulk [10, 11, 12]. In a topological material, there is a relation between the bulk and edges or surfaces, which is called the bulk-edge correspondence [13, 14]. The bulk-edge correspondence implies that the topological invariant in the bulk is equivalent to the number of edge or surface zero-energy modes. The edge or surface modes in topological superconductors are Majorana fermions, which has been first proposed in Ref. [15].

The emergence of Majorana fermions as elementary excitations in topological superconductors is what makes this research field significant not only from the fundamental point of view, but also for technological applications. Majorana fermions are their own antiparticles [16] and due to the non-Abelian exchange statistics that they obey, they open the door to new

and powerful methods of topological quantum computing [17, 18]. Majorana fermions have been detected in both one-dimensional systems [10] and two-dimensional systems [11, 12] using scanning tunneling microscopy. A conceptual diagram of a scanning tunneling microscope is shown in Fig. 1.1 (a). By getting a metal probe closer to the surface of a material, the tunneling current I occurs and is measured by a current measurement system. By changing bias voltage V induced to the metal probe, the differential tunneling conductance defined as $\frac{\mathrm{dI}}{\mathrm{dV}}$ is measured as shown in Fig. 1.1 (b). Such measurement is called scanning tunneling spectroscopy. Because the differential tunneling conductance is proportional to the density of states (DOS) at the Fermi level [19], this technique can be used to obtain the spatial and energy dependence of the local DOS. In particular, a peak in the differential tunneling conductance at an edge or a surface of the material with no bias energy indicates the existence of a zero-energy edge or surface mode. A Majorana fermion appears as a zero-energy bound state at an edge or a surface of a topological superconductor. A Majorana zero mode can also appear at the interface between a topological superconductor and a trivial material: It will be trapped at the interface and can go into the bulk of neither material.

For example, as a one-dimensional system, on top of a lead surface, ferromagnetic Fe atomic chains were deposited in the experiment of Ref. [10]. Lead is a conventional s-wave superconductor that intrinsically has strong Rashba spin-orbit coupling. The detection of a Majorana zero-energy mode was conducted using a scanning tunneling microscope. The spatial and energy dependence of the differential tunneling conductance was obtained. At zero energy where there is no bias voltage, the differential tunneling conductance was observed to peak at the end of the chain, indicating the existence of a zero-energy bound state. Also, as a two-dimensional system, a monolayer lead was grown on a silicon substrate with a magnetic disk of cobalt in the experiment of Ref. [11]. This s-wave superconducting and ferromagnetic hybrid system was investigated using a scanning tunneling microscope. Along the surface of the disk, Majorana fermions were detected as zero-energy bound states. In our study, we use the model Hamiltonian of TSC with broken time-reversal symmetry which is directly applicable to this system. In addition, a Majorana zero-energy vortex bound state has been detected in the topological superconductor $FeTe_{0.6}Se_{0.4}$ by scanning tunneling microscopy [12]. Because a scanning tunneling microscope with a high energy resolution was used, the

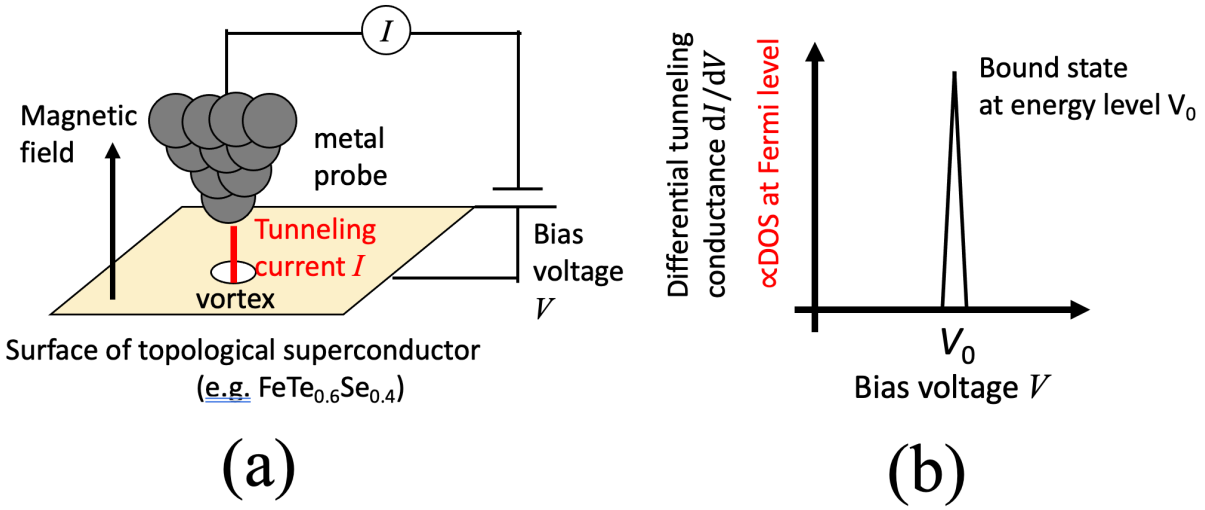

Figure 1.1: (a) A conceptual diagram of the scanning tunneling microscope. (b) A conceptual diagram of a result of scanning tunneling spectroscopy.

detected zero-energy state could be distinguished from low-energy, but nonzero-energy bound states of regular quasiparticles. Topological quantum computing using Majorana fermions as qubits is possible by braiding Majorana vortex bound states [20].

Topological materials can be classified according to the topological invariant in the bulk, which is in turn determined by the symmetries of the system [21, 22]. For example, in the presence of translational symmetry, a two-dimensional topological system with particle-hole symmetry and without time-reversal and chiral symmetries is characterized by the Thouless-Kohmoto-Nightingale-Nijs (TKNN) number [23] or the first Chern number [24, 9], which are essentially the same.

Superconductivity (SC) is a quantum phenomenon defined by two key features, zero resistance and perfect diamagnetism. Since the first discovery in 1911 [25], many attempts have been made for revealing the mechanism of SC [26, 27, 28, 29, 30, 31]. One of the most significant accomplishments is the Bardeen-Cooper-Schrieffer (BCS) theory of SC [32], which microscopically describes the superconducting state as a quantum-mechanical many-body collective phenomenon. In the superconducting state, the gauge symmetry is spontaneously broken, as the phase of the condensate wave function is fixed macroscopically [19]. Due to perfect diamagnetism which originates from the spontaneously broken gauge symmetry, SC is distinguished from perfect conductivity which merely means zero resistance. The difference

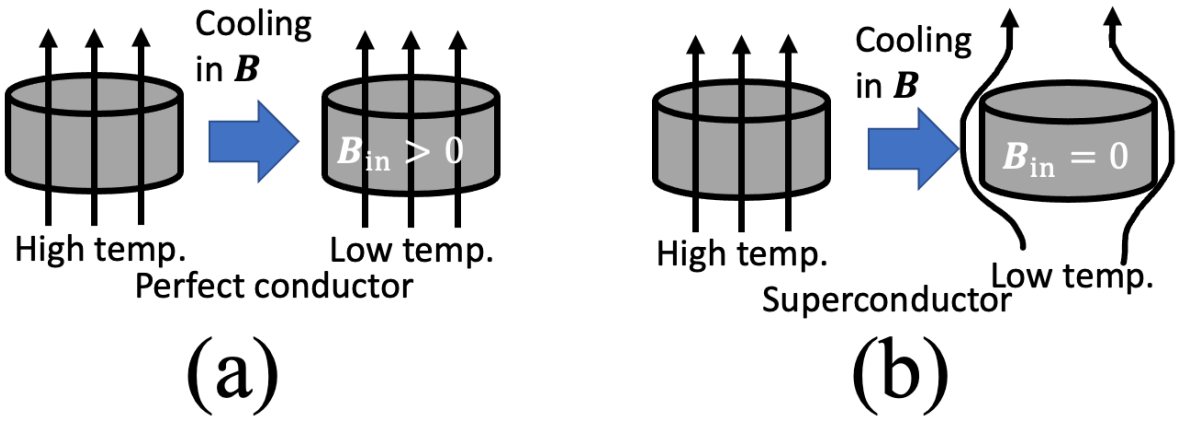

Figure 1.2: Cooling (a) a perfect conductor and (b) a superconductor under external magnetic field.

between a perfect conductor and a superconductor as they are cooled under external magnetic field is illustrated in Fig. 1.2. When the external magnetic field $\boldsymbol{B}$ is applied to a material, the magnetic field inside the material $\boldsymbol{B}_{\text{in}}$ is

$$\boldsymbol{B}_{\text{in}} = \boldsymbol{B}(1 + 4\pi\chi), \tag{1.1}$$

where χ is the magnetic susceptibility. Diamagnetism occurs when $\chi < 0$ and perfect diamagnetism when $\chi = -\dfrac{1}{4\pi}$. In the case of a perfect conductor, $\boldsymbol{B}_{\text{in}} > 0$ after the cooling. In contrast, in the case of a superconductor, the magnetic field cannot penetrate inside due to perfect diamagnetism and $\boldsymbol{B}_{\text{in}} = 0$ after the cooling.

SC is a result of spontaneously broken gauge symmetry, and it is different from ferromagnetism in metals [33, 34, 35] which is a result of spontaneously broken rotational symmetry of spin. Both phenomena are due to the spontaneous breaking of the continuous symmetry; however, behind SC is the Anderson-Higgs mechanism [36, 37, 38], which results in the energy gap (i.e., a 'massive' excitation). On the other hand, the massless Nambu-Goldstone mode [39, 40] appears in the case of ferromagnetism in metals. The massless Nambu-Goldstone mode (boson) is associated with collective excitation of the electrons' spin called a magnon [41, 42], whose energy dispersion is linear and vanishes as wave vector approaches zero.

While SC is a result of spontaneously broken gauge symmetry, topological materials present fundamentally different quantum collective phenomena. These topological phenomena emerge not as a result of the spontaneous breaking of any symmetry, but rather due

to the presence of nontrivial topology in the bulk [21]. Thus, SC and topological phenomena are fundamentally different in their origin and can coexist, as is realized in TSC. The topological invariant describing TSC is conventionally defined in momentum space [43]. The momentum-space representation is based on the periodicity or translational invariance of the system [44]. Conventional crystals have translational symmetry and are periodic. Meanwhile, the so-called quasicrystals (QCs) [45, 46] without translational symmetry have recently been studied intensively [47, 48, 49, 50, 51, 52]. QCs are introduced in the subsequent section, which form a new class of topological materials altogether.

1.2 Quasicrystals

QCs are unconventional materials which show Bragg peaks even though their structure has no periodicity and possess peculiar rotational symmetry that is forbidden by crystallography [53]. X-ray diffraction of a QC will exhibit Bragg peaks with such unusual symmetry, which would fill the entire momentum space in the limit of infinite system size [54]. It was Shechtman who discovered the first QC with icosahedral diffraction symmetry in Al-Mn alloys in 1984 [45, 55], for which he was awarded the Nobel Prize in Chemistry in 2011 [56]. Such materials showing Bragg peaks without periodic order that defy the laws of crystallography were dubbed as QCs [46]. One of the astonishing features of icosahedral QCs is fivefold diffraction symmetry, which is not realizable in conventional crystals. Other than two, three, four, or sixfold rotational symmetry, there are no single unit cells that can fill the entire plane or space without any gap. Fivefold rotational symmetry can be realized by two or more kinds of unit cells in a QC. For example, Penrose tiling has a two-dimensional quasiperiodic structure, which is composed of two kinds of unit cells and shows fivefold rotational symmetry. The Ammann-Beenker (AB) tiling is another example of a two-dimensional QC with two kinds of unit cells, which shows eightfold rotational symmetry.

QCs have a high potential to be applied for useful products [57]. There are mainly five good properties of QCs; high resistance metal, low thermal conductance [58], hardness even at high temperatures, low friction [59, 60], and high water repellency. Utilizing these properties, QCs can be applied for coating a frying pan, automotive parts, razor blades,

needles and surgical tools, and so on, and also they can be used for air-space applications [61]. The French company Sitram Cybernox used to produce quasicrystalline-coated frying pans [62]. Using electron beam vapor deposition in vacuum, the surface of a frying pan can be coated by Al-Fe-Cu QC. The electron beam vapor deposition is a method that by irradiating a material with an electron beam emitted from an electron gun, the material is heated and vaporized in vacuum, and a substrate is covered by the material. The Al-Fe-Cu-coated frying pan can stand high temperatures such as 700 to 800 degrees Celsius, in contrast to Teflon, a commonly used, coated frying pan without QCs, which can sustain up to 400 to 500 degrees Celsius. In comparison with Al-Fe-Cu QC, Al itself heats up too quickly and non-uniformly. Due to the low thermal conductivity of Al-Fe-Cu QC, the temperature of an Al-Fe-Cu-coated frying pan remains relatively uniform when heated.

There are many unanswered important questions about QCs. For instance, a superconducting state in QCs is interesting. Soon after Shechtman's discovery, in 1987, the icosahedral phase of $Mg_3Zn_3Al_2$ was reported to show SC [63], although this alloy was not a QC despite its icosahedral symmetry. Recently, however, SC has been confirmed in an Al-Zn-Mg QC [49]. The BCS theory can explain the observed thermodynamic properties of SC in the Al-Zn-Mg QC, implying that it is conventional SC originating in electron-phonon interactions. It is fascinating that even in a quasicrystalline system a superconducting state is realizable, considering that the conventional BCS theory assumes translational symmetry and is formulated in momentum space. In the BCS theory, not only the electron-electron attraction via exchange of phonons, but also a sufficiently high DOS at the Fermi energy are key. In a QC, however, there may or may not be single-particle states at the Fermi level in the normal state, depending on the electron density. In particular, QCs tend to have pseudogaps in their energy spectrum. Moreover, both Penrose and AB QCs are known to have families of strictly localized states at zero energy. A Penrose QC has an energy gap above and below zero energy, and would be insulating if the Fermi level is placed in one of those gaps.

While there have been theoretical studies of conventional s-wave SC in Penrose [64, 65] and AB [66] QCs, it is interesting to examine the possible occurrence of TSC in QCs. Theoretically, so far TSC has only been studied in periodic crystals such as square lattice systems. Thanks to translational symmetry in such systems, topological invariants such as the first

Chern number are calculated in momentum space. Is translational symmetry required for the existence of TSC? This question was first addressed in the Fibonacci-Kitaev model as the simplest example of a one-dimensional quasicrystalline topological superconductor [67]. This work has recently been generalized for two spatial dimensions in Ref. [68], where topological phase transitions and TSC have been demonstrated to occur in both Penrose and AB QCs. For calculating a topological invariant, periodic boundary condition (PBC) is required. QC approximant is an approximated quasicrystal, which can be considered with PBC. In QC approximants, the Bott index [69, 70] has been calculated as the topological invariant, which is equivalent to the first Chern number in translationally symmetric systems. The Bott index has been shown to signify the non-Abelian nature of the TSC phase in QCs, where Majorana fermions appear along surfaces or in a vortex [68].

In the work of Ref. [68], however, the superconducting order parameter was assumed to be uniform. While the order parameter is uniformly distributed in periodic systems, there is no good reason to assume a uniform order parameter in aperiodic systems such as QCs. So the question still remains, as to whether a stable TSC phase can occur in QCs, despite their aperiodic and fractal structure. QCs are inherently fractal, characterized by self-similarity. This particular feature of QCs is sure to affect the topological superconducting state if it is realizable, and most likely the possible existence of TSC itself. The goal of this thesis is to address these questions by solving for the order parameter self-consistently in Penrose and AB QC approximants; whether TSC can exist stably in QCs and what the properties of such TSC states are. We use the microscopic mean-field theory of SC formulated in real space, the Bogoliubov-de Gennes (BdG) theory [71].

1.3 Motivation for Research

Both TSC and QCs are fascinating areas of studies, both from fundamental and application perspectives. Meanwhile, not much research has been done in the new area interfacing these two areas. The major obstacle for research combining TSC and QCs is the absence of translational symmetry in QCs. In QC systems, due to the lack of translational symmetry, methods frequently adopted in conventional crystallography such as Fourier transform are not

applicable. In this thesis, we generalize the tight-binding model for 2D TSC of Sato, Takahashi, and Fujimoto [72] for QC approximants, and we solve the BdG equations [71] directly and self-consistently [73, 74]. A self-consistent approach can be applied even if the system does not hold translational symmetry. The considered model describes 2D TSC with broken time-reversal symmetry as experimentally realized in Pb/Co island on Si(111) [11], whose topological nature is governed by the first Chern number. For QC approximants, the Bott index is calculated as the topological invariant of the system, which plays the role of the first Chern number in the absence of translational symmetry. By solving for the superconducting order parameter self-consistently, the stability of TSC in QC approximants is examined. The possible applications would be topological quantum computing using quasicrystals.

1.4 Layout of Thesis

This thesis aims to introduce TSC and to examine how the aperiodic and fractal nature of QCs affects the TSC states. The thesis is organized as follows. In Chapter 2, the microscopic mean-field theory of SC as the theoretical background is briefly described. Chapter 3 introduces the concept of topology in condensed matter physics. Chapter 4 provides the basic background knowledge on QCs. The outcomes of the calculation are shown and discussed in Chapter 5. Finally, Chapter 6 concludes the thesis and discusses the main results obtained.

2 Superconductivity Theory

TSC, the topic of this thesis, is a certain kind of SC. SC is a quantum phenomenon experimentally discovered in 1911 [25]. The microscopic theory proposed by Bardeen, Cooper, and Schrieffer (BCS) in 1957 [32], which earned them the Nobel prize in Physics in 1972 [75], can explain the so-called low-temperature or conventional s-wave SC arising from electron-phonon interactions. In this chapter, first the BCS theory is briefly described for a better understanding of TSC introduced later [19]. Then, the BdG theory [71] for the extended Hubbard model for conventional s-wave SC is discussed.

2.1 The Bardeen-Cooper-Schrieffer Theory of Superconductivity

The BCS theory [32] is one of the most fundamental theories of SC, based upon the Landau-Fermi liquid theory [76, 77]. The Landau-Fermi liquid theory is an effective theory proposed by Landau in 1956 [76], describing interacting Fermi systems (Fermi 'liquid') such as a group of electrons residing in a substance. Without interactions, free electrons spread through the substance, each being characterized by a wave number and spin. When the Landau-Fermi liquid theory is applicable the coherence of electrons as waves is not lost even in the presence of electron-electron interactions, and the system of interacting electrons can be described as a gas of free electrons, albeit with a different mass compared to the bare electron mass. Most importantly, the system is characterized by the existence of a well-defined Fermi surface, similarly to the case of free electrons.

Based on the Landau-Fermi liquid theory, Bardeen, Cooper, and Schrieffer developed the theory of SC, now known as the BCS theory [32]. Some important parts of the BCS theory

are briefly explained below [78]. The starting point is the "reduced Hamiltonian",

$$\hat{H}_{\text{red}} = 2\sum_{\boldsymbol{k}} \epsilon_{\boldsymbol{k}} \hat{b}^{\dagger}_{\boldsymbol{k}} \hat{b}_{\boldsymbol{k}} + \sum_{\boldsymbol{k},\boldsymbol{k}'} V_{\boldsymbol{k}',\boldsymbol{k}} \hat{b}^{\dagger}_{\boldsymbol{k}'} \hat{b}_{\boldsymbol{k}}, \tag{2.1}$$

where $\hat{b}^{\dagger}_{\boldsymbol{k}}$ ($\hat{b}_{\boldsymbol{k}}$) is the creation (annihilation) operator of a Cooper pair in a state $(\boldsymbol{k}\uparrow, -\boldsymbol{k}\downarrow)$, and $V_{\boldsymbol{k}',\boldsymbol{k}}$ is the weak electron-phonon interaction that scatters a Cooper pair from $\boldsymbol{k}$ to $\boldsymbol{k}'$. The annihilation operator of a Cooper pair $(\boldsymbol{k}\uparrow, -\boldsymbol{k}\downarrow)$ is $\hat{b}_{\boldsymbol{k}} = \hat{c}_{-\boldsymbol{k}\downarrow}\hat{c}_{\boldsymbol{k}\uparrow}$, governed by the commutation relations,

$$\left[\hat{b}_{\boldsymbol{k}}, \hat{b}^{\dagger}_{\boldsymbol{k}'}\right] = 0; \boldsymbol{k} \neq \boldsymbol{k}', \tag{2.2}$$

$$\left[\hat{b}_{\boldsymbol{k}}, \hat{b}_{\boldsymbol{k}'}\right] = 0 = \left[\hat{b}^{\dagger}_{\boldsymbol{k}}, \hat{b}^{\dagger}_{\boldsymbol{k}'}\right], \tag{2.3}$$

$$\left[\hat{b}_{\boldsymbol{k}}, \hat{b}^{\dagger}_{\boldsymbol{k}}\right] = 1 - \left(\hat{n}_{\boldsymbol{k}\uparrow} + \hat{n}_{-\boldsymbol{k}\downarrow}\right), \tag{2.4}$$

where the number operator $\hat{n}_{\boldsymbol{k}\sigma} = \hat{c}^{\dagger}_{\boldsymbol{k}\sigma}\hat{c}_{\boldsymbol{k}\sigma}$ counts the number of the electrons in $(\boldsymbol{k}, \sigma)$. Equation. (2.4) clearly shows that the Cooper pair operators are not bosonic. BCS proposed a trial many-body wave function as

$$|\Psi_0\rangle \propto \prod_{k} \left(1 + \alpha_{\boldsymbol{k}} \hat{b}^{\dagger}_{\boldsymbol{k}}\right)|0\rangle \tag{2.5}$$

for the groud state of the reduced Hamiltonian, where $\{\alpha_{\boldsymbol{k}}\}$ are the parameters to be determined by the variational principle to minimize the ground-state energy. It is the simplest to normalize this wave function by normalizing it for each state $\boldsymbol{k}$ and write it as

$$|\Psi_0\rangle = \prod_{k} \left(u_{\boldsymbol{k}} + v_{\boldsymbol{k}} \hat{b}^{\dagger}_{\boldsymbol{k}}\right)|0\rangle, \tag{2.6}$$

where,

$$u_{\boldsymbol{k}} = \frac{1}{1 + |\alpha_{\boldsymbol{k}}|^2} \tag{2.7}$$

is the probability amplitude for the ground state not to contain a Cooper pair (a pair of electrons in $(\boldsymbol{k}\uparrow, -\boldsymbol{k}\downarrow)$) in state $\boldsymbol{k}$ and

$$v_{\boldsymbol{k}} = \frac{\alpha_{\boldsymbol{k}}}{1 + |\alpha_{\boldsymbol{k}}|^2} \tag{2.8}$$

is for the ground state to contain a Cooper pair in state $\boldsymbol{k}$. These $u_{\boldsymbol{k}}$ and $v_{\boldsymbol{k}}$ satisfy the normalization condition,

$$|u_{\boldsymbol{k}}|^2+|v_{\boldsymbol{k}}|^2= 1. \tag{2.9}$$

Using the method of Lagrange multipliers,

$$\delta E = \delta \left\langle \Psi_0 \left| \hat{H}_{\rm red} - \mu \hat{N} \right| \Psi_0 \right\rangle = 0 \tag{2.10}$$

gives

$$\begin{pmatrix} \epsilon_{\boldsymbol{k}} - \mu & \Delta_{\boldsymbol{k}} \\ \Delta^*_{\boldsymbol{k}} & -(\epsilon_{\boldsymbol{k}} - \mu) \end{pmatrix} \begin{pmatrix} u_{\boldsymbol{k}} \\ v_{\boldsymbol{k}} \end{pmatrix} = E_{\boldsymbol{k}} \begin{pmatrix} u_{\boldsymbol{k}} \\ v_{\boldsymbol{k}} \end{pmatrix}. \tag{2.11}$$

Here, μ is the chemical potential which is the Lagrange multiplier, $\hat{N}$ is the number operator to count the number of electrons in the system, and the order parameter $\Delta_{\boldsymbol{k}}$ is self-consistently determined by

$$\Delta_{\boldsymbol{k}} = -\sum_{\boldsymbol{k}'} V_{\boldsymbol{k}',\boldsymbol{k}} u_{\boldsymbol{k}'} v^*_{\boldsymbol{k}'}. \tag{2.12}$$

This turns out to be the energy gap to break up a Cooper pair $(\boldsymbol{k}\uparrow, -\boldsymbol{k}\downarrow)$. Accordingly,

$$E_{\boldsymbol{k}} = \sqrt{(\epsilon_{\boldsymbol{k}} - \mu)^2 + |\Delta_{\boldsymbol{k}}|^2} \tag{2.13}$$

is the energy required to create a single-particle (‘ quasiparticle ’) excitation.

The $\boldsymbol{k}$ dependence of the superconducting order parameter is determined by the pairing interaction $V_{\boldsymbol{k}',\boldsymbol{k}}$ leading to SC, which can have, for example, s-, p-, or d-wave pairing symmetry. Here s, p, and d refer to the relative angular momentum of a Cooper pair $\ell = 0$, 1, and 2, respectively. Due to the Pauli exclusion principle, s- and d-wave SC has a spin-singlet Cooper pair, while p-wave SC has spin-triplet pairing. For isotropic s-wave SC, $V_{\boldsymbol{k}'\boldsymbol{k}} = -V$ $(V > 0)$ and $\Delta_{\boldsymbol{k}} \equiv \Delta$ (constant), then the self-consistent equation of the order parameter in Eq. (2.12) reduces to

$$\Delta = \sum_{\boldsymbol{k}'} V \frac{\Delta}{2E_{\boldsymbol{k}'}}, \tag{2.14}$$

namely,

$$1 = \frac{V}{2} \sum_{\boldsymbol{k}'} \frac{1}{E_{\boldsymbol{k}'}}. \tag{2.15}$$

In the continuum model as used by BCS, it is assumed that the electron-phonon interaction is nonzero within $\pm\hbar\omega_D$ about the Fermi surface:

$$\frac{V}{2}\sum_{\boldsymbol{k}'}\frac{1}{E_{\boldsymbol{k}'}} \simeq \frac{V}{2}D(\epsilon_F)\int_{-\hbar\omega_D}^{\hbar\omega_D}\frac{d\epsilon}{\sqrt{\epsilon^2+\Delta^2}}, \tag{2.16}$$

where ω_D is the Debye frequency and $D(\epsilon_F)$ is the density of states (DOS) at the Fermi energy assumed to be constant in this narrow energy range. In the weak-coupling limit, $VD(\epsilon_F) \ll 1$, and the BCS value of the energy gap at zero temperature is given by

$$\Delta = 2\hbar\omega_D e^{-\frac{1}{VD(\epsilon_F)}}. \tag{2.17}$$

The BCS theory can explain the experimental results on conventional or low-temperature superconductors. For example, the BCS theory predicts the ratio of the minimum excitation energy from the ground state and the critical temperature of the phase transition between the normal and superconducting states as [19]

$$\frac{2\Delta}{k_{\mathrm{B}}T_{\mathrm{c}}} = \frac{2\pi}{e^{\gamma}} \approx 3.53. \tag{2.18}$$

Thus, according to the BCS theory, this value is independent of material parameters and can be used for testing the BCS theory. Table. 2.1 lists experimentally observed values for some conventional superconductors in comparison with the prediction of the BCS theory [79, 80]. Considering that the observation error is of the order of ± 0.1, the BCS theory well explains the experimental results except in the case of Hg and Pb. The reason why the BCS theory does not work well for Hg and Pb is the relatively large $VD(\epsilon_F)$ in Hg and Pb. The BCS theory can also explain other thermodynamic properties such as $\left.\frac{\Delta C}{C_{\mathrm{n}}}\right|_{T=T_{\mathrm{c}}}$. Here, $\Delta C = (C_{\mathrm{s}} - C_{\mathrm{n}})_{T\to T_{\mathrm{c}}-0}$, where C_{s} and C_{n} are the specific heat at constant volume in the superconducting and normal state, respectively. The BCS theory predicts

$$\left.\frac{\Delta C}{C_{\mathrm{n}}}\right|_{T=T_{\mathrm{c}}} = \frac{12}{7\zeta(3)} \approx 1.43, \tag{2.19}$$

which is also universal and a good test of the BCS theory. Table. 2.1 also compares experimentally observed $\left.\frac{\Delta C}{C_{\mathrm{n}}}\right|_{T=T_{\mathrm{c}}}$ and the prediction of the BCS theory [79, 80]. Expect for Nb, Hg, and Pb, the BCS theory reproduces the experimental results well.

In summary, the BCS theory can explain the properties of conventional or low-temperature superconductors with weak electron-phonon coupling with smaller $VD(\epsilon_F)$. However, the

Table 2.1: Comparison of the prediction of the BCS theory and experimental results [79, 80] The "BCS" listed as "Elements" in the last column represents the prediction of the BCS.

Elements	Al	V	Zn	Nb	Cd	In
T_c [K]	1.196	5.30	0.852	9.23	0.56	3.40
$\hbar\omega_D/k_B$ [K]	428	380	327	275	209	108
$2\Delta/k_BT_c$	3.4	3.4	3.2	3.8	3.2	3.6
$\Delta C/C_n\|_{T=T_c}$	1.45	1.5	1.3	1.9	1.4	1.7
Elements	Sn (β)	Ta	Hg (α)	Tl	Pb	BCS
T_c [K]	3.72	4.39	4.15	2.39	7.19	-
$\hbar\omega_D/k_B$ [K]	199	240	71.9	78.5	105	-
$2\Delta/k_BT_c$	3.5	3.6	4.6	3.6	4.3	3.53
$\Delta C/C_n\|_{T=T_c}$	1.6	1.6	2.4	1.5	2.7	1.43

BCS theory assumes translational symmetry and is formulated in momentum space, and thus cannot deal with spatial inhomogeneities or applied magnetic field.

2.2 Bogoliubov-de Gennes Theory for the Extended Hubbard Model for Conventional s-wave Superconductivity

In this section, the BdG theory [71] is described for the extended Hubbard model for conventional s-wave SC. The BdG theory is a generalization of the BCS theory and formulated in coordinate space. While it is equivalent to the BCS theory for translationally invariant systems, it is more general and powerful than the BCS theory as it can incorporate inhomogeneities and applied magnetic field. The extended Hubbard model is a tight-binding model to describe SC. The extended Hubbard Hamiltonian is

$$H = H_0 + H_1, \tag{2.20}$$

where

$$H_0 = \sum_{\langle ij\rangle\sigma} t_{ij}\hat{c}^\dagger_{i\sigma}\hat{c}_{j\sigma} + \sum_{i\sigma}(\epsilon_i - \mu)\hat{n}_{i\sigma}, \tag{2.21}$$

$$H_1 = \sum_i U_{ii}\hat{n}_{i\uparrow}\hat{n}_{i\downarrow} + \frac{1}{2}\sum_{\langle ij\rangle}\sum_{\sigma\sigma'} U_{ij}\hat{n}_{i\sigma}\hat{n}_{j\sigma'}. \tag{2.22}$$

Here t_{ij} is the probability amplitude for the electron to hop from site j to site i, which we set to be the uniform nonzero value $-t(t > 0)$ only for the hopping between nearest-neighbor sites and $t_{ij} = t_{ji}$. The notation $\langle ij\rangle$ above means that the sum is over all lattice sites i and only nearest-neighbor sites j for each i. $\hat{c}^\dagger_{i\sigma}$ and $\hat{c}_{i\sigma}$ are the creation and annihilation operators of an electron at lattice site i with spin orientation $\sigma = \uparrow or \downarrow$ which satisfy the anticommutation relations $\left\{\hat{c}^\dagger_{i\sigma}, \hat{c}^\dagger_{j\tau}\right\} = \{\hat{c}_{i\sigma}, \hat{c}_{j\tau}\} = 0$ and $\left\{\hat{c}_{i\sigma}, \hat{c}^\dagger_{j\tau}\right\} = \delta_{i,j}\delta_{\sigma,\tau}$ where $\delta_{i,j}$ is the Kronecker delta for i and j, $\hat{n}_{i\sigma} = \hat{c}^\dagger_{i\sigma}\hat{c}_{i\sigma}$ counts the number of electrons at lattice site i with spin σ, ϵ_i is a single-impurity (nonmagnetic) potential at site i, μ is the chemical potential, U_{ii} is the on-site interaction at site i, and U_{ij} is the off-site interaction between nearest-neighbor sites.

Let $\epsilon_i = 0$ at all sites and consider the uniform and attractive on-site interaction $U_{ii} = -U(U > 0)$ and let $U_{ij} = 0; \forall j \neq i$. Here, $U > 0$ means that the total energy is lowered due to the on-site interaction. The Hamiltonian in Eq.(2.20) then reduces to the attractive Hubbard Hamiltonian,

$$H_{\text{att}} = -t\sum_{\langle i,j\rangle\sigma} \hat{c}^\dagger_{i\sigma}\hat{c}_{j\sigma} - \mu\sum_{i\sigma}\hat{n}_{i\sigma} - U\sum_i \hat{n}_{i\uparrow}\hat{n}_{i\downarrow}. \tag{2.23}$$

The mean-field approximation is applied to the interaction term in Eq.(2.23) which contains four operators. The mean-field approximation assumes that the difference between operators and their average value, such as $\hat{c}^\dagger_{i\uparrow}\hat{c}_{i\uparrow} - \left\langle \hat{c}^\dagger_{i\uparrow}\hat{c}_{i\uparrow}\right\rangle$ or $\hat{c}^\dagger_{i\downarrow}\hat{c}_{i\downarrow} - \left\langle \hat{c}^\dagger_{i\downarrow}\hat{c}_{i\downarrow}\right\rangle$, is small and neglects its square. Using the mean-field approximation and the anticommutation relations that the creation and annihilation operators of an electron satisfy, the attractive Hubbard Hamiltonian

in Eq.(2.23) can be reduced to the effective Hamiltonian expressed in the matrix form,

$$\mathcal{H}_{\text{eff}} = \sum_{ij} \begin{pmatrix} \hat{c}^\dagger_{i\uparrow} & \hat{c}_{i\downarrow} \end{pmatrix} \begin{pmatrix} t_{ij} + V^{\text{diag}}_{ii} & \Delta^{\downarrow\uparrow}_{ii} \\ (\Delta^{\downarrow\uparrow}_{ii})^* & -t_{ij} - V^{\text{diag}}_{ii} \end{pmatrix} \begin{pmatrix} \hat{c}_{j\uparrow} \\ \hat{c}^\dagger_{j\downarrow} \end{pmatrix} + \sum_i V^{\text{diag}}_{ii} + \frac{1}{U} \sum_i \left[(V^{(\text{H})}_{ii})^2 + |\Delta^{\downarrow\uparrow}_{ii}|^2 \right], \tag{2.24}$$

where the Hartree potential created by electrons with either spin at lattice site i is defined as

$$V^{(\text{H})}_{ii} = -U \left\langle \hat{c}^\dagger_{i\uparrow} \hat{c}_{i\uparrow} \right\rangle = -U \left\langle \hat{c}^\dagger_{i\downarrow} \hat{c}_{i\downarrow} \right\rangle, \tag{2.25}$$

and the superconducting order parameter at lattice site i is defined as

$$\Delta^{\downarrow\uparrow}_{ii} = -U \left\langle \hat{c}_{i\downarrow} \hat{c}_{i\uparrow} \right\rangle. \tag{2.26}$$

Here, $V^{\text{diag}}_{ii} = -\mu + V^{(\text{H})}_{ii}$ and the Kronecker delta $\delta_{i,j}$ is implicit for V^{diag}_{ii} and $\Delta^{\downarrow\uparrow}_{ii}$.

The $(1,1)$ element ($(2,2)$ element) of the matrix in the first term in Eq. (2.24) represents the single-electron (single-hole) part of the Hamiltonian, while the $(1,2)$ element ($(2,1)$ element) represents the interaction between an electron at lattice site j and a hole at lattice site i (an electron at lattice site i and a hole at lattice site j). Here, a hole is defined so that $\hat{c}^\dagger_{i\sigma}$ ($\hat{c}_{i\sigma}$) is the annihilation (creation) operator of a hole at lattice site i with spin σ. In the superconducting state where the electron-hole interaction is present, the Hamiltonian in Eq. (2.24) is not diagonalized in the basis of the creation and annihilation operators of electrons due to the superconducting order parameter in the off-diagonal elements. Thus, a unitary transformation is required for diagonalizing the Hamiltonian in Eq. (2.24), which means that the eigenstates of the Hamiltonian in Eq. (2.24) are expressed as linear superpositions of an electron and a hole. This implies that electrons and holes are not distinguishable in the superconducting state and a single-particle excitation in a superconductor is always part electron and part hole, which is called a quasiparticle excitation. In the BdG theory [71], the eigenvalue equations of the Hamiltonian are called the BdG equations, where the mean-field Hamiltonian is called the BdG Hamiltonian. The BdG equations are coupled Schrödinger-like equations for the electron and hole component of a quasiparticle.

By performing a unitary transformation, the first term in Eq. (2.24) can be diagonalized as

$$\begin{aligned}\sum_{ij}\begin{pmatrix}\hat{c}^{\dagger}_{i\uparrow} & \hat{c}_{i\downarrow}\end{pmatrix}\begin{pmatrix}t_{ij}+V^{\mathrm{diag}}_{ii} & \Delta^{\downarrow\uparrow}_{ii}\\ (\Delta^{\downarrow\uparrow}_{ii})^{*} & -t_{ij}-V^{\mathrm{diag}}_{ii}\end{pmatrix}\begin{pmatrix}\hat{c}_{j\uparrow}\\ \hat{c}^{\dagger}_{j\downarrow}\end{pmatrix}\\ =\sum_{n,m}\begin{pmatrix}\hat{\gamma}^{\dagger}_{n} & \hat{\gamma}_{n}\end{pmatrix}\begin{pmatrix}E_n\delta_{n,m} & 0\\ 0 & -E_n\delta_{n,m}\end{pmatrix}\begin{pmatrix}\hat{\gamma}_{m}\\ \hat{\gamma}^{\dagger}_{m}\end{pmatrix},\end{aligned} \tag{2.27}$$

where $\hat{\gamma}^{\dagger}_{m}$ ($\hat{\gamma}_{m}$) is the creation (annihilation) operator of a quasiparticle in a single-particle state m, which is a linear superposition of the operators of an electron and a hole. After the diagonalization, the $(1,1)$ element of the matrix on the right hand side in Eq. (2.27) is the positive energy required to create a quasiparticle excitation, which is measured from the chemical potential. All the negative-energy single-particle states are occupied at zero temperature.

The BdG theory is an expression of the BCS theory in coordinate space, overcoming the major weak point of the BCS theory. That is, the BCS theory assumes that the system is homogeneous and momentum is a good quantum number, in which case the superconducting order parameter is uniformly distributed in space. In the presence of spatial inhomogeneities as due to impurities or applied magnetic field, however, the superconducting order parameter cannot be assumed to be uniformly distributed. Because momentum is no longer a good quantum number, the Hamiltonian should be expressed in coordinate space, and the BdG theory is helpful.

The Hartree potential in Eq. (2.25) and the superconducting order parameter in Eq.(2.26) are determined self-consistently using the following method. First, we give an initial guess for the Hartree potential and superconducting order parameter, and generate the BdG Hamiltonian using the initial guess. Then diagonalize the BdG Hamiltonian and obtain the eigenenergies and normalized eigenstates. Then, using these eigenenergies and eigenstates, we calculate the Hartree potential and the superconducting order parameter as in Eq. (2.25) and Eq.(2.26), which are the next guess for the Hartree potential and superconducting order parameter. We repeat this procedure, obtaining the guess for the Hartree potential and superconducting order parameter at the lth (l is a natural number) iteration step by using the guess at the

$(l-1)$th iteration step, until the convergence criterion is satisfied. The convergence criterion for the lth iteration step is given by

$$\frac{\|\vec{\Delta}^{(l)} - \vec{\Delta}^{(l-1)}\|}{\|\vec{\Delta}^{(l-1)}\|} < 10^{-6}, \tag{2.28}$$

where $\vec{\Delta}^{(l)}$ is a complex vector of length N whose ith element is Δ_i of the lth iteration step and $\|\vec{\Delta}^{(l)}\|$ is the norm of $\vec{\Delta}^{(l)}$, where N is the total number of lattice sites. The Hartree potential must also satisfy the analogous convergence criterion as a real vector of length N. The self-consistent iterations are repeated until both mean fields are converged under the given criterion.

2.3 Bogoliubov-de Gennes Theory for Topological Superconductivity

In this section, by adding a magnetic field for Zeeman coupling and Rashba spin-orbit coupling to the effective Hamiltonian in Eq. (2.24), the tight-binding Hamiltonian for TSC [72, 74] is introduced. With the Zeeman magnetic coupling and Rashba spin-orbit coupling terms, the Hartree potential becomes spin-dependent and the Hartree potential at lattice site i felt by an electron with spin $\bar{\sigma} \neq \sigma$ is defined as

$$V_{ii\sigma}^{(\mathrm{H})} = -U \langle \hat{n}_{i\sigma} \rangle = -U \left\langle \hat{c}_{i\sigma}^{\dagger} \hat{c}_{i\sigma} \right\rangle. \tag{2.29}$$

Due to the spin dependence, the effective Hamiltonian now has a 4×4 structure:

$$\begin{aligned}
&\mathcal{H}_{\mathrm{eff}} \\
&= \frac{1}{2} \sum_{ij} \begin{pmatrix} \hat{c}_{i\uparrow}^{\dagger} & \hat{c}_{i\downarrow}^{\dagger} & \hat{c}_{i\uparrow} & \hat{c}_{i\downarrow} \end{pmatrix} \begin{pmatrix} t_{ij} + V_{ii\uparrow}^{\mathrm{diag}} & (V_{ij}^{\mathrm{SO}})^{\dagger} & 0 & \Delta_{ii}^{\downarrow\uparrow} \\ V_{ij}^{\mathrm{SO}} & t_{ij} + V_{ii\downarrow}^{\mathrm{diag}} & \Delta_{ii}^{\uparrow\downarrow} & 0 \\ 0 & (\Delta_{ii}^{\uparrow\downarrow})^{*} & -t_{ij} - V_{ii\uparrow}^{\mathrm{diag}} & -(V_{ij}^{\mathrm{SO}})^{\mathsf{T}} \\ (\Delta_{ii}^{\downarrow\uparrow})^{*} & 0 & -(V_{ij}^{\mathrm{SO}})^{*} & -t_{ij} - V_{ii\downarrow}^{\mathrm{diag}} \end{pmatrix} \begin{pmatrix} \hat{c}_{j\uparrow} \\ \hat{c}_{j\downarrow} \\ \hat{c}_{j\uparrow}^{\dagger} \\ \hat{c}_{j\downarrow}^{\dagger} \end{pmatrix} \\
&\quad + \frac{1}{2} \sum_{i\sigma} \left(-\mu + h_{\sigma} + V_{ii\bar{\sigma}}^{(\mathrm{H})} \right) + \frac{1}{U} \sum_{i} \left[V_{ii\uparrow}^{(\mathrm{H})} V_{ii\downarrow}^{(\mathrm{H})} + |\Delta_{ii}^{\downarrow\uparrow}|^2 \right],
\end{aligned} \tag{2.30}$$

where $h_{\sigma} = -h$ $(+h)$ for $\sigma = \uparrow$ $(\sigma = \downarrow)$, V_{ij}^{SO} represents the Rashba spin-orbit coupling which acts between an electron at lattice site i with spin $\downarrow$ and an electron at lattice site j with

spin $\uparrow$, $\bar{\sigma}$ is the opposite spin of σ, $V_{ii\sigma}^{\mathrm{diag}} = -\mu + h_\sigma + V_{ii\bar{\sigma}}^{(\mathrm{H})}$, and the Kronecker delta $\delta_{i,j}$ is implicit for $V_{ii\sigma}^{\mathrm{diag}}$, $\Delta_{ii}^{\downarrow\uparrow}$ and $\Delta_{ii}^{\uparrow\downarrow}$.

By defining the average of the Hartree potential in a system of N lattice sites,

$$\bar{V}_\sigma^{(\mathrm{H})} = \frac{1}{N}\sum_i V_{ii\sigma}^{(\mathrm{H})}, \tag{2.31}$$

the effective Hamiltonian in Eq. (2.30) can be rewritten as

$$\begin{aligned}
&\mathcal{H}_{\mathrm{eff}} \\
&= \frac{1}{2}\sum_{ij}\begin{pmatrix}\hat{c}_{i\uparrow}^\dagger & \hat{c}_{i\downarrow}^\dagger & \hat{c}_{i\uparrow} & \hat{c}_{i\downarrow}\end{pmatrix}\begin{pmatrix} t_{ij}+V_{ii\uparrow}^{\mathrm{diag}} & (V_{ij}^{\mathrm{SO}})^\dagger & 0 & \Delta_{ii}^{\downarrow\uparrow} \\ V_{ij}^{\mathrm{SO}} & t_{ij}+V_{ii\downarrow}^{\mathrm{diag}} & \Delta_{ii}^{\uparrow\downarrow} & 0 \\ 0 & (\Delta_{ii}^{\uparrow\downarrow})^* & -t_{ij}-V_{ii\uparrow}^{\mathrm{diag}} & -(V_{ij}^{\mathrm{SO}})^{\mathsf{T}} \\ (\Delta_{ii}^{\downarrow\uparrow})^* & 0 & -(V_{ij}^{\mathrm{SO}})^* & -t_{ij}-V_{ii\downarrow}^{\mathrm{diag}}\end{pmatrix}\begin{pmatrix}\hat{c}_{j\uparrow} \\ \hat{c}_{j\downarrow} \\ \hat{c}_{j\uparrow}^\dagger \\ \hat{c}_{j\downarrow}^\dagger\end{pmatrix} \\
&\quad + \frac{1}{2}\sum_{i\sigma}\left(\epsilon_{i\sigma} - \tilde{\mu} + \delta\bar{V}_\sigma + h_\sigma + V_{ii\bar{\sigma}}^{(\mathrm{H})} - \bar{V}_{\bar{\sigma}}^{(\mathrm{H})}\right) + \frac{1}{U}\sum_i\left[V_{ii\uparrow}^{(\mathrm{H})}V_{ii\downarrow}^{(\mathrm{H})} + |\Delta_{ii}^{\downarrow\uparrow}|^2\right],
\end{aligned} \tag{2.32}$$

where

$$\tilde{\mu} = \mu - \frac{\bar{V}_\uparrow^{(\mathrm{H})} + \bar{V}_\downarrow^{(\mathrm{H})}}{2}, \tag{2.33}$$

$$\delta\bar{V} = \frac{\bar{V}_\uparrow^{(\mathrm{H})} - \bar{V}_\downarrow^{(\mathrm{H})}}{2}, \tag{2.34}$$

$$\bar{V}_{ii\uparrow}^{\mathrm{diag}} = -\tilde{\mu} - \delta\bar{V} - h + V_{ii\downarrow}^{(\mathrm{H})} - \bar{V}_\downarrow^{(\mathrm{H})}, \tag{2.35}$$

and

$$\bar{V}_{ii\downarrow}^{\mathrm{diag}} = -\tilde{\mu} + \delta\bar{V} + h + V_{ii\uparrow}^{(\mathrm{H})} - \bar{V}_\uparrow^{(\mathrm{H})}. \tag{2.36}$$

3 Topological States of Matter

TSC, the topic of this thesis, is characterized by topology. Topology has been originally developed in mathematics and later utilized in physics [8, 9]. Classification of quantum-mechanical many-body states of topological materials can be achieved in terms of topology [21]. In this chapter, fundamental concepts used in the topological analysis of physical phenomena are introduced [19]. Also, the topological analysis is illustrated in some example systems such as the model for the integer quantum Hall effect [81, 82, 83, 84, 23, 85, 9], Haldane model [86], and Kitaev model [87].

3.1 Parameter-Dependent Hamiltonian

In this section, the fundamental concepts utilized in the analysis of topological quantum phenomena are briefly introduced [19].

3.1.1 Berry Connection, Berry Curvature, Berry Phase

As an example for the illustration, let a parameter-dependent Hamiltonian be $\mathcal{H}(\boldsymbol{R})$, described by M real parameters $\boldsymbol{R} = (R_1, R_1, \ldots, R_M)$. The corresponding Schrödinger equation is

$$\mathcal{H}(\boldsymbol{R}) \left| m; \boldsymbol{R} \right\rangle = E_m(\boldsymbol{R}) \left| m; \boldsymbol{R} \right\rangle , \tag{3.1}$$

where m is an index for distinguishing different eigenstates. If it were not for any band crossings, a complete orthonormal set $\{|m; \boldsymbol{R}\rangle\}$ can be chosen so that

$$\left\langle m; \boldsymbol{R} \middle| n; \boldsymbol{R} \right\rangle = \delta_{mn}, \quad \sum_m \left| m; \boldsymbol{R} \right\rangle \left\langle m; \boldsymbol{R} \right| = 1. \tag{3.2}$$

Here, the Berry connection $A_n(\boldsymbol{R})$ is introduced as

$$A_n(\boldsymbol{R}) = \frac{1}{i} \left\langle n; \boldsymbol{R} \middle| \left(\nabla_{\boldsymbol{R}} \middle| n; \boldsymbol{R} \right\rangle \right), \tag{3.3}$$

where $\imath = \sqrt{-1}$. Let us consider the time development of the state. Suppose that $\boldsymbol{R}$ starts from $\boldsymbol{R} = \boldsymbol{R}_0$ at time $t = 0$, and returns to $\boldsymbol{R} = \boldsymbol{R}_0$ at $t = \tau$. Using the dimensionless time $s = \dfrac{t}{\tau}$, the corresponding time-dependent Schrödinger equation is

$$\imath\hbar\frac{d}{ds}\left|\psi(s)\right\rangle = \mathcal{H}(\boldsymbol{R}(s))\tau\left|\psi(s)\right\rangle. \tag{3.4}$$

The initial state is $\left|\psi(s=0)\right\rangle = \left|n;\boldsymbol{R}_0\right\rangle$, and the final state is

$$\left|\psi(s=1)\right\rangle = \exp\left(-\frac{\imath}{\hbar}\int_0^\tau E_n(\boldsymbol{R}(t))dt\right)\exp\left(-\imath\gamma_n(C)\right)\left|n;\boldsymbol{R}_0\right\rangle. \tag{3.5}$$

These two states are the same state with different phases. The effect of the movement of $\boldsymbol{R}$ on the phase difference is

$$\gamma_n(C) = \oint_C \boldsymbol{A}_n(\boldsymbol{R})\cdot d\boldsymbol{R}, \tag{3.6}$$

dubbed as the Berry phase [43].

Here, $\exp\left(-\imath\gamma_n(C)\right)$ is a gauge-invariant quantity, namely, invariant under the gauge transformation. In general, for a given function $\Lambda(\boldsymbol{r},t)$, the gauge transformation changes a scalar potential $\phi(\boldsymbol{r},t)$ and a vector potential $\boldsymbol{A}_n(\boldsymbol{R})$ as

$$\phi(\boldsymbol{r},t) \mapsto \psi(\boldsymbol{r},t) - \frac{1}{c}\frac{\partial\Lambda}{\partial t} \tag{3.7}$$

and

$$\boldsymbol{A}(\boldsymbol{r},t) \mapsto \boldsymbol{A}(\boldsymbol{r},t) + \nabla\Lambda(\boldsymbol{r},t), \tag{3.8}$$

respectively. The electric field $\boldsymbol{E}(\boldsymbol{r},t)$ and the magnetic flux density $\boldsymbol{B}(\boldsymbol{r},t)$, which are written by $\phi(\boldsymbol{r},t)$ and $\boldsymbol{A}_n(\boldsymbol{R})$, are gauge invariant. By changing $\left|n;\boldsymbol{R}\right\rangle$ to $\exp\left(i\Lambda_n(\boldsymbol{R})\right)\left|n;\boldsymbol{R}\right\rangle$, the Berry connection is changed by $\nabla_{\boldsymbol{R}}\Lambda_n(\boldsymbol{R})$. This changing does not affect $\exp\left(-\imath\gamma_n(C)\right)$ when both $\left|n;\boldsymbol{R}\right\rangle$ and $\exp\left(\imath\Lambda_n(\boldsymbol{R})\right)\left|n;\boldsymbol{R}\right\rangle$ are uniquely defined on C. Also, the Berry curvature is defined as

$$\boldsymbol{B}_n(\boldsymbol{R}) = \nabla_{\boldsymbol{R}}\times\boldsymbol{A}_n(\boldsymbol{R}), \tag{3.9}$$

which is related with the Berry phase by Stokes' theorem as

$$\gamma_n(C) = \int_S \boldsymbol{B}_n(\boldsymbol{R})\cdot d\boldsymbol{S}. \tag{3.10}$$

3.1.2 An Example in Two Level System

For instance, a two-level system

$$\hat{H}(\boldsymbol{R}) = \boldsymbol{R} \cdot \hat{\boldsymbol{\sigma}} \tag{3.11}$$

can be considered [19] with $\boldsymbol{R} = (X, Y, Z)$ and $\hat{\boldsymbol{\sigma}} = 2\frac{\boldsymbol{s}}{\hbar}$. The corresponding Schrödinger equation is

$$\hat{H}(\boldsymbol{R}) \left|\pm; \boldsymbol{R}\right\rangle = \pm R \left|\pm; \boldsymbol{R}\right\rangle . \tag{3.12}$$

In this case, the Berry curvature is $\boldsymbol{B}_{\pm}(\boldsymbol{R}) = \pm\dfrac{\boldsymbol{R}}{2R^3}$, and thus

$$\nabla_{\boldsymbol{R}} \cdot \boldsymbol{B}_{\pm}(\boldsymbol{R}) = \pm 2\pi\delta(\boldsymbol{R}). \tag{3.13}$$

Here, there are two expressions for $\left|\pm; \boldsymbol{R}\right\rangle$ with different singularities:

$$\left|+; \boldsymbol{R}\right\rangle^{(A)} = \frac{1}{\sqrt{2R(R+Z)}}((R+Z)\left|+\right\rangle + (X+\imath Y)\left|-\right\rangle), \tag{3.14}$$

$$\left|-; \boldsymbol{R}\right\rangle^{(A)} = \frac{1}{\sqrt{2R(R+Z)}}(-(X-\imath Y)\left|+\right\rangle + (R-Z)\left|-\right\rangle), \tag{3.15}$$

and

$$\left|+; \boldsymbol{R}\right\rangle^{(B)} = \frac{1}{\sqrt{2R(R-Z)}}((X-\imath Y)\left|+\right\rangle + (R-Z)\left|-\right\rangle), \tag{3.16}$$

$$\left|-; \boldsymbol{R}\right\rangle^{(B)} = \frac{1}{\sqrt{2R(R-Z)}}(-(R-Z)\left|+\right\rangle + (X+\imath Y)\left|-\right\rangle). \tag{3.17}$$

In the limit of $\boldsymbol{R}$ approaching the positive (negative) part of the z-axis, $\left|+; \boldsymbol{R}\right\rangle^{(A)}$ ($\left|+; \boldsymbol{R}\right\rangle^{(B)}$) is not uniquely determined. These two states are related as

$$\left|+; \boldsymbol{R}\right\rangle^{(B)} = \exp\left(-\imath\phi\right)\left|+; \boldsymbol{R}\right\rangle^{(A)} \tag{3.18}$$

and

$$\left|-; \boldsymbol{R}\right\rangle^{(B)} = \exp\left(\imath\phi\right)\left|-; \boldsymbol{R}\right\rangle^{(A)}, \tag{3.19}$$

where $\phi = \mathrm{Arg}(X + \imath Y)$ is the argment of $X + \imath Y$. Put differently, the singular gauge transformation

$$\boldsymbol{A}_{\pm}^{(B)}(\boldsymbol{R}) = \boldsymbol{A}_{\pm}^{(A)}(\boldsymbol{R}) \mp \nabla_{\boldsymbol{R}}\phi \tag{3.20}$$

maps the singularity in the negative part of the z-axis onto the positive part of it. In general, $|n;\boldsymbol{R}\rangle$ is not uniquely determined on the line started from the band crossing point (Dirac string [88]) and $\boldsymbol{A}_n(\boldsymbol{R})$ diverges. The shape of the Dirac string can be transformed under the singular gauge transformation; however, it can never be removed. Accordingly, Stokes' theorem can be applied to calculation of the Berry phase in Eq. (3.10) only when the band crossings never occur on the surface S and the phase of $|n;\boldsymbol{R}\rangle$ needs to be selected so that S does not cross the Dirac strings. Under these conditions, the quantity $\Phi_n = \int_S \boldsymbol{B}_n(\boldsymbol{R}) \cdot dS$ is quantized as an integer multiple of 2π. Here, let S be divided into two surfaces $S^{(A)}$ and $S^{(B)}$ and the phase of $|n;\boldsymbol{R}\rangle$ is selected so that Dirac strings do not cross $S^{(A)}$ or $S^{(B)}$. Then,

$$\begin{aligned}\Phi_n &= \int_S \boldsymbol{B}_n(\boldsymbol{R}) \cdot d\boldsymbol{S} \\ &= \int_{S^{(A)}} \boldsymbol{B}_n(\boldsymbol{R}) \cdot d\boldsymbol{S} + \int_{S^{(B)}} \boldsymbol{B}_n(\boldsymbol{R}) \cdot d\boldsymbol{S} \\ &= \oint_C \boldsymbol{A}_n^{(A)}(\boldsymbol{R}) \cdot d\boldsymbol{R} - \oint_C \boldsymbol{A}_n^{(B)}(\boldsymbol{R}) \cdot d\boldsymbol{R}.\end{aligned} \tag{3.21}$$

Because both $|n;\boldsymbol{R}\rangle^{(A)}$ and $|n;\boldsymbol{R}\rangle^{(B)}$ are uniquely determined on C and connected via the singular gauge transformation, the difference between $\oint_C \boldsymbol{A}_n^{(A)}(\boldsymbol{R}) \cdot d\boldsymbol{R}$ and $\oint_C \boldsymbol{A}_n^{(B)}(\boldsymbol{R}) \cdot d\boldsymbol{R}$ are an integer multiple of 2π. Therefore, the (first) Chern number $\dfrac{\Phi_n}{2\pi}$ is an integer quantity, and an example of a topological invariant. A topological invariant is a quantity that is preserved under a continuous transformation. It is known that the Chern number is the bulk topological invariant for all insulators with broken time-reversal symmetry. As long as the gap does not close, any continuous deformation of the Hamiltonian does not affect the Chern number.

3.2 Integer Quantum Hall Effect

In this section, the integer quantum Hall effect [81, 82, 83, 84, 23, 85] is briefly described from the perspective of topology [9, 19]. The integer quantum Hall effect is the precise quantization of the Hall conductance in a two-dimensional electron gas in a strong magnetic field at low temperature, the very first example discovered of a two-dimensional topological insulator. It belongs to the same class as two-dimensional TSC with broken time-reversal

symmetry of the model used in this thesis and is characterized by the first Chern number [21]. In the original experiment conducted by Hall, a magnetic field was applied to a gold leaf, and a current was found to flow longitudinally in the leaf. The electric voltage between the conductor's lateral edges is called the "Hall voltage". In the integer quantum Hall systems, the Hall conductance is quantized as $\frac{ne^2}{h}$, where n is an integer characterizing each plateau as a function of the applied magnetic field.

In a model of the integer quantum Hall effect, the Schödinger equation for a single electron is

$$\hat{H}\left|\alpha\right\rangle = \epsilon_\alpha \left|\alpha\right\rangle, \quad \hat{H} = \frac{\boldsymbol{\pi}^2}{2m_e} + V(\hat{\boldsymbol{r}}) + \frac{g_e \mu_B B}{\hbar}\hat{s}_z. \tag{3.22}$$

The so-called twisted boundary condition

$$\hat{T}_{-L\boldsymbol{e}_\mu}\left|\alpha\right\rangle = \exp\left(\imath\theta_\mu\right)\left|\alpha\right\rangle, \quad (\mu = x, y) \tag{3.23}$$

is imposed where $L\boldsymbol{e}_x$ and $L\boldsymbol{e}_y$ are periodic vectors, and $\hat{T}_{-L\boldsymbol{e}_\mu}$ is a translation operator. Under the singular gauge transformation

$$\left|\tilde{\alpha;\boldsymbol{\theta}}\right\rangle = \hat{U}(\boldsymbol{\theta})\left|\alpha;\boldsymbol{\theta}\right\rangle, \quad \hat{U}(\boldsymbol{\theta}) = \exp\left(-\imath\frac{\boldsymbol{\theta}\cdot\boldsymbol{r}}{L}\right), \tag{3.24}$$

the Schrödinger equation is changed to

$$\hat{\tilde{H}}(\boldsymbol{\theta})\left|\tilde{\alpha;\boldsymbol{\theta}}\right\rangle = \epsilon_\alpha(\boldsymbol{\theta})\left|\tilde{\alpha;\boldsymbol{\theta}}\right\rangle, \quad \hat{\tilde{H}}(\boldsymbol{\theta}) = \hat{U}(\boldsymbol{\theta})\hat{H}\hat{U}^{-1}(\boldsymbol{\theta}) = \hat{H}|_{\boldsymbol{\pi}\mapsto\boldsymbol{\pi}+\frac{\hbar}{L}\boldsymbol{\theta}}. \tag{3.25}$$

The singular gauge transformation maps the twisted boundary condition to the periodic one since $\hat{T}_{-L\boldsymbol{e}_\mu}\left|\tilde{\alpha;\boldsymbol{\theta}}\right\rangle = \left|\tilde{\alpha;\boldsymbol{\theta}}\right\rangle$, and the single-electron Hamiltonian with the periodic boundary condition depends on $\boldsymbol{\theta}$. In the thermodynamic limit, the Hall conductivity $\sigma_{xy}(\boldsymbol{\theta})$ is averaged over θ as

$$\overline{\sigma}_{xy}(\boldsymbol{\theta}) = \int_0^{2\pi}\frac{d\theta_x}{2\pi}\int_0^{2\pi}\frac{d\theta_y}{2\pi}\sigma_{xy}(\boldsymbol{\theta}), \tag{3.26}$$

which can be calculated by the TKNN formula [23],

$$\overline{\sigma}_{xy} = \frac{e^2}{\hbar}\sum_{\epsilon_\alpha\le\mu}\int_0^{2\pi}\frac{d\theta_x}{2\pi}\int_0^{2\pi}\frac{d\theta_y}{2\pi}B_\alpha(\boldsymbol{\theta}). \tag{3.27}$$

Here, $B_\alpha(\boldsymbol{\theta})$ is the Berry curvature calculated from $\hat{H}(\boldsymbol{\theta})$. The twisted boundary condition in Eq. (3.23) makes $B_\alpha(\boldsymbol{\theta})$ periodic:

$$B_\alpha(\theta_x + 2\pi, \theta_y) = B_\alpha(\theta_x, \theta_y + 2\pi) = B_\alpha(\theta_x, \theta_y). \tag{3.28}$$

The Chern number N_α is

$$N_\alpha = \frac{1}{2\pi}\int_0^{2\pi} d\theta_x \int_0^{2\pi} d\theta_y B_\alpha(\boldsymbol{\theta}). \tag{3.29}$$

Using Eq. (3.27),

$$\overline{\sigma}_{xy} = N_{Ch}\frac{e^2}{\hbar}, \quad N_{Ch} = \sum_{\epsilon_\alpha \leq \mu} N_\alpha. \tag{3.30}$$

Since the Chern number is quantized as an integer, the θ-averaged Hall conductivity is also quantized as an integer multiple of $\frac{e^2}{\hbar}$. More detailed description of the integer quantum Hall effect including the existence of the plateaus can be constructed when the energy distribution of the so-called edge states is taken into account.

3.3 Haldane Model

In this section, the Haldane model [86] is introduced as an example of a topological system whose phase is classified by the Chern number.

3.3.1 Basics of Graphene

The Haldane model is based upon the structure of graphene. Graphene is made out of carbon atoms arranged in hexagonal structure, as illustrated in Fig. 3.1. The red and blue dots represent the lattice points, and the black lines represent the nearest-neighbor connections between lattice points. Every red (blue) point is connected to blue (red) point, thus the structure of graphene is said to be bipartite. The lattice vectors of grapene, $\boldsymbol{c}_1$ and $\boldsymbol{c}_2$, and the corresponding reciprocal lattice vectors, $\boldsymbol{b}_1$ and $\boldsymbol{b}_2$, and the vectors connecting nearest-neighbor sites $\boldsymbol{\delta}_1, \boldsymbol{\delta}_2$ and $\boldsymbol{\delta}_3$ are shown in Fig. 3.4. These are written as

$$\boldsymbol{c}_1 = \frac{c}{2}(3, \sqrt{3}), \quad \boldsymbol{c}_2 = \frac{a}{2}(3, -\sqrt{3}), \tag{3.31}$$

$$\boldsymbol{b}_1 = \frac{2\pi}{3a}(1, \sqrt{3}), \quad \boldsymbol{b}_2 = \frac{2\pi}{3a}(1, -\sqrt{3}), \tag{3.32}$$

and

$$\boldsymbol{\delta}_1 = \frac{a}{2}(1, \sqrt{3}), \quad \boldsymbol{\delta}_2 = \frac{a}{2}(1, -\sqrt{3}), \quad \boldsymbol{\delta}_3 = -a(1, 0). \tag{3.33}$$

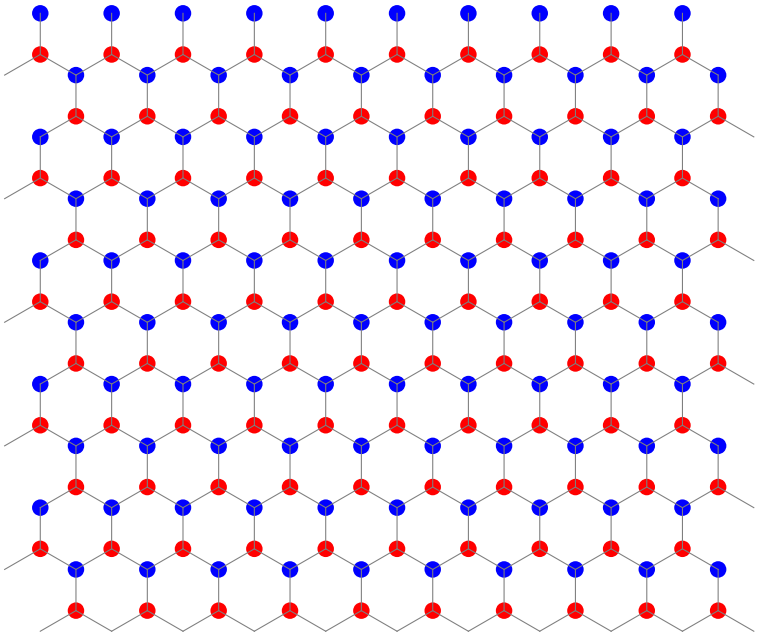

Figure 3.1: The structure of graphene.

Here, $a \approx 1.42$ Å is an atomic length between the nearest-neighbor sites, and the reciprocal lattice vectors are defined by $\boldsymbol{c}_i \cdot \boldsymbol{b}_j = 2\pi\delta_{ij}$. Two points of the first Brillouin zone illustrated as $\boldsymbol{K}$ and $\boldsymbol{K'}$ in Fig. 3.4 are called the Dirac points,

$$\boldsymbol{K} = \left(\frac{2\pi}{3a}, \frac{2\pi}{3\sqrt{3}a}\right), \quad \boldsymbol{K}' = \left(\frac{2\pi}{3a}, -\frac{2\pi}{3\sqrt{3}a}\right). \tag{3.34}$$

The open boundary condition (OBC) in one direction and PBC in the other direction, called the ribbon boundary condition, is applied. There are several graphene ribbons whose edges are different from each other. Among them, two of the most fundamental ribbons are called armchair-type and zigzag-type, illustrated in Fig. 3.2 and Fig. 3.3, respectively. The edge of an armchair-type ribbon resembles an armchair and the edge of a zigzag-type ribbon is zigzag.

3.3.2 Tight-Binding Model with Nearest-Neighbor Hopping

In this subsection, the energy spectrum of graphene is considered in the scheme of Fig. 3.5. The unit cell includes two atoms A and B, colored by blue and red. Utilizing the system's bipartite symmetry, the wave function has a form of $(\Psi_A, \Psi_B)^{\mathsf{T}}$. Here, $|\Psi_A|^2$ ($|\Psi_B|^2$) represents the probability amplitude for the electron to be at the site A (B). First, by considering

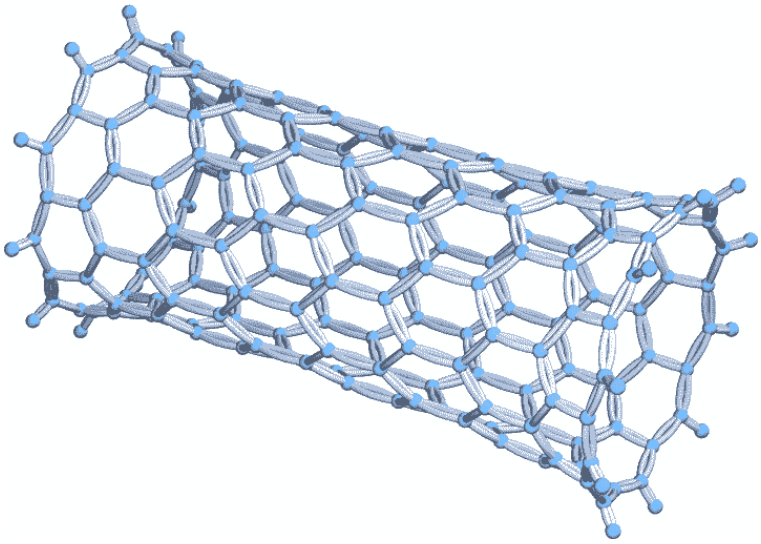

Figure 3.2: Armchair-type ribbon of graphene.

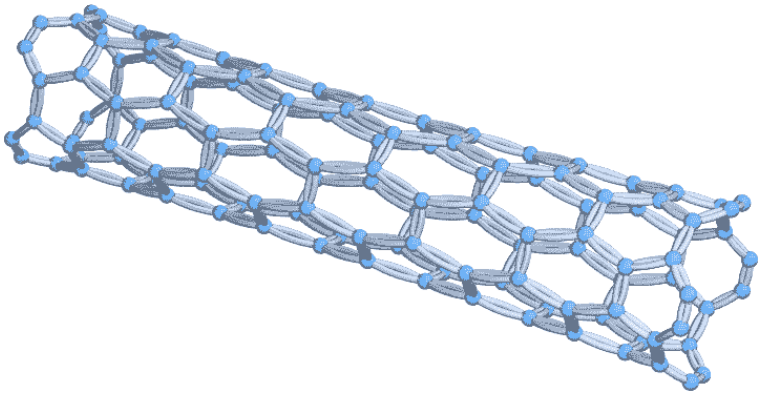

Figure 3.3: Zigzag-type ribbon of graphene.

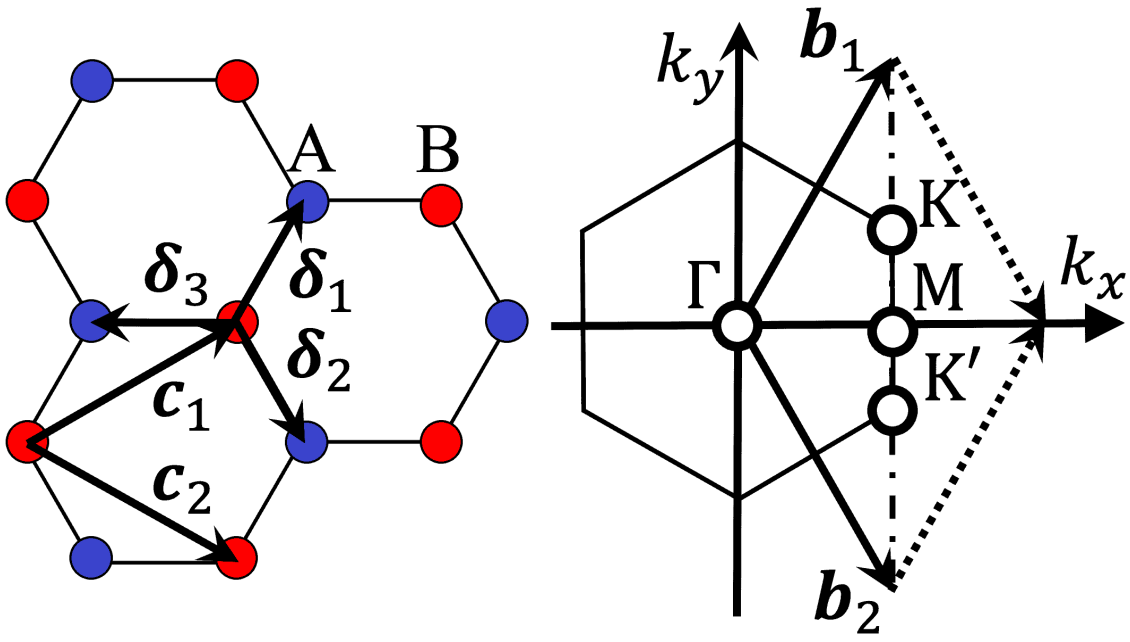

Figure 3.4: The lattice vectors $\boldsymbol{c}_1$ and $\boldsymbol{c}_2$, the corresponding reciprocal lattice vectors $\boldsymbol{b}_1$ and $\boldsymbol{b}_2$, and nearest-neighbor vectors $\boldsymbol{\delta}_1, \boldsymbol{\delta}_2$ and $\boldsymbol{\delta}_3$.

only the nearest-neighbor hopping with amplitude t_1, the tight-binding Bloch Hamiltonian is

$$H_0(\boldsymbol{k}) = \begin{pmatrix} 0 & h(\boldsymbol{k}) \\ h^\dagger(\boldsymbol{k}) & 0 \end{pmatrix}, \tag{3.35}$$

with $\boldsymbol{k} = (k_x, k_y)$ and

$$h(\boldsymbol{k}) = t_1 \sum_i \exp\left(i\boldsymbol{k} \cdot \boldsymbol{a}_i\right). \tag{3.36}$$

For simplicity, let the lattice spacing be unity. For $i = 1, 2$ and 3,

$$\boldsymbol{a}_i = \left(\cos\frac{2(i-1)}{3}\pi, \sin\frac{2(i-1)}{3}\pi\right) \tag{3.37}$$

are the vectors connecting nearest-neighbors.

The Hamiltonian in Eq. (3.35) has three important symmetries. First, because the Hamiltonian in Eq. (3.35) does not include the σ_z component of the Pauli matrices, the bipartite symmetry is preserved. Put differently, this Hamiltonian is block off-diagonal and

$$\sigma_z H_0(\boldsymbol{k}) \sigma_z = -H_0(\boldsymbol{k}). \tag{3.38}$$

The bipartite symmetry protects the closed gap at the Dirac points, which is explained later within this subsection. Second, the Hamiltonian has a threefold rotational symmetry. The

inside of the exponential in Eq. (3.35) is invariant under the $\frac{2\pi}{3}$ rotation, as the set of $\{\boldsymbol{a}_i\}_{i=1,2,3}$ is invariant. Actually, from Eq. (3.37), the $\frac{2\pi}{3}$ rotation maps $\boldsymbol{a}_i$ to $\boldsymbol{a}_{i+1}$, with the periodic condition $\boldsymbol{a}_4 = \boldsymbol{a}_1$. There are six gap closing points in momentum space, among which two of them are essential due to the threefold rotational symmetry. Finally, the system has time-reversal symmetry. As Eq. (3.37) does not include any spin terms, the time-reversal symmetry operator in momentum space is equivalent to the complex conjugation with $\boldsymbol{k} \mapsto -\boldsymbol{k}$. Using $\sigma_y^* = \sigma_y^{\mathsf{T}}$,

$$H_0(\boldsymbol{k}) = H_0^*(-\boldsymbol{k}) \tag{3.39}$$

is obtained from Eq. (3.37). The time-reversal symmetry operator maps one Dirac point $\boldsymbol{K}$ to the other point $\boldsymbol{K}$' and vice versa. Combining the bipartite symmetry and time-reversal symmetry yields particle-hole symmetry,

$$\sigma_z H_0^*(-\boldsymbol{k})\sigma_z = -H_0(\boldsymbol{k}) \tag{3.40}$$

By diagonalizing the Bloch Hamiltonian in Eq. (3.35), the energy spectrum $E(\boldsymbol{k})$ can be obtained as follows:

$$\begin{vmatrix} -E(\boldsymbol{k}) & h(\boldsymbol{k}) \\ h^\dagger(\boldsymbol{k}) & -E(\boldsymbol{k}) \end{vmatrix} = 0, \tag{3.41}$$

$$\begin{aligned}
E(\boldsymbol{k}) &= \pm|h(\boldsymbol{k})| \\
&= \pm|t_1| \left| \sum_{i=1}^{3} \exp\left(\imath \boldsymbol{k} \cdot \boldsymbol{a}_i\right) \right| \\
&= \pm|t_1| \left| \exp\left(\imath \boldsymbol{k} \cdot (1,0)\right) + \exp\left(\imath \boldsymbol{k} \cdot \left(-\frac{1}{2}, \frac{\sqrt{3}}{2}\right)\right) + \exp\left(\imath \boldsymbol{k} \cdot \left(-\frac{1}{2}, -\frac{\sqrt{3}}{2}\right)\right) \right| \\
&= \pm|t_1| \left| \exp\left(\imath k_x\right) + \exp\left(-\frac{i}{2}k_x\right) 2\cos\frac{\sqrt{3}}{2}k_y \right| \\
&= \pm|t_1| \left| \exp\left(-\frac{\imath}{2}k_x\right) \right| \left| \exp\left(\frac{3\imath}{2}k_x\right) + 2\cos\frac{\sqrt{3}}{2}k_y \right| \\
&= \pm|t_1| \left| \exp\left(\frac{3\imath}{2}k_x\right) + 2\cos\frac{\sqrt{3}}{2}k_y \right|.
\end{aligned} \tag{3.42}$$

This energy spectrum is illustrated in Fig. 3.6, plotted for $k_x, k_y \in [-\pi, \pi]$. The two bands are touching at the six corners of the Brillouin zone. The corresponding gap closing condition

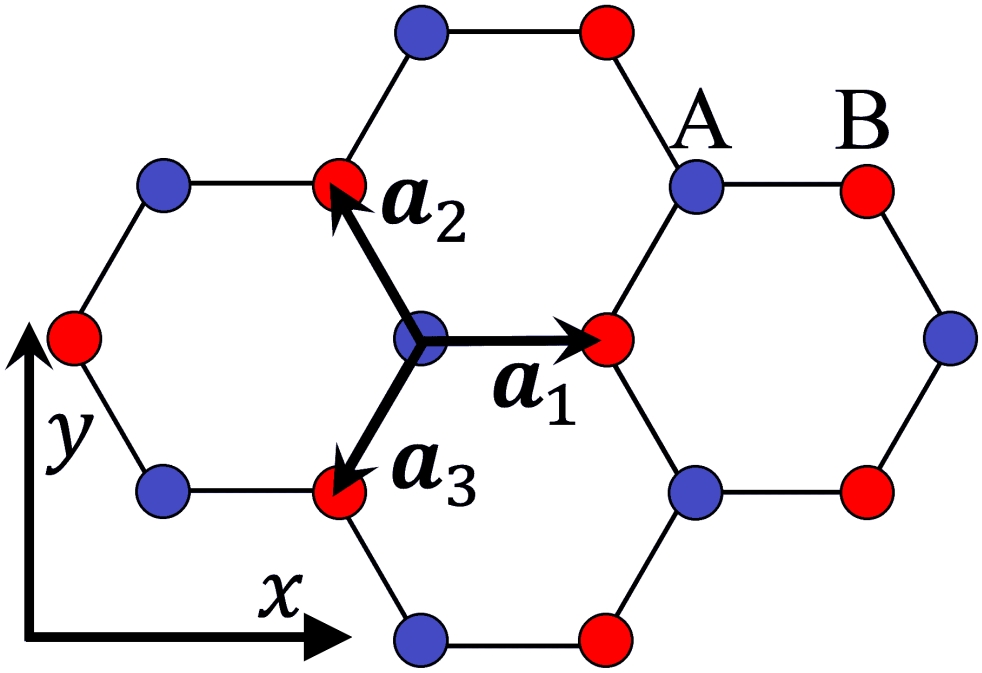

Figure 3.5: Structure of graphene and vectors connecting nearest-neighbor sites. The bipartite lattice sites A and B are colored by blue and red, respectively.

$E(\boldsymbol{k}) = 0$ gives $\left|\exp\left(\frac{3i}{2}k_x\right) + 2\cos\frac{\sqrt{3}}{2}k_y\right| = 0$. Two of the solutions for this equation are so-called the Dirac points,

$$\boldsymbol{K} = \left(\frac{2\pi}{3}, \frac{2\pi}{3\sqrt{3}}\right), \boldsymbol{K}' = \left(\frac{2\pi}{3}, -\frac{2\pi}{3\sqrt{3}}\right), \tag{3.43}$$

which coincides with Eq. (3.34) when $a = 1$. Due to the threefold symmetry, the six gap closing points are essentially the same as the two Dirac points. Actually, by adding a certain reciprocal lattice vector, $\boldsymbol{K}$ or $\boldsymbol{K}$' can coincide with any gap closing points. Around the Dirac points, the two bands are crossing linearly. As this shape resembles a cone, these are called the Dirac cones. Each Dirac cone corresponds to a massless Dirac fermion.

3.3.3 System with the Broken Bipartite Symmetry

The Dirac cones in Fig. 3.6 are protected by both bipartite and time-reversal symmetries. Thus, the system does not show any topological feature. The bipartite symmetry can be broken by introducing an opposite on-site energy M and $-M$ to the sites A and B, respectively.

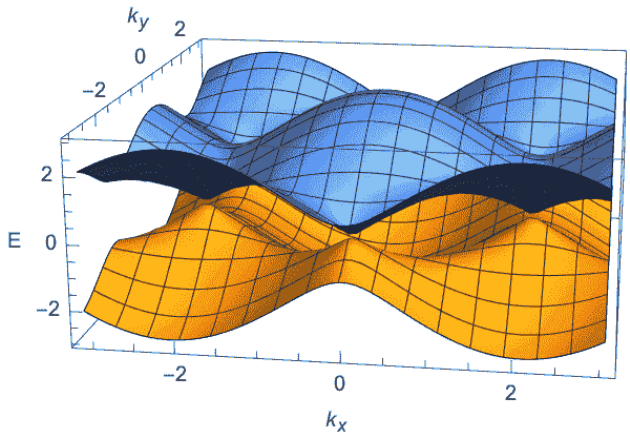

Figure 3.6: The energy spectrum of graphene $E(\boldsymbol{k})$ plotted for $k_x, k_y \in [-\pi, \pi]$. The Dirac cones reside on the Dirac points $\boldsymbol{K}$, $\boldsymbol{K}$'.

The corresponding Hamiltonian $H_M(\boldsymbol{k})$ is expressed by

$$H_M(\boldsymbol{k}) = H_0(\boldsymbol{k}) + M\sigma_z. \tag{3.44}$$

The energy spectrum is changed to

$$E(\boldsymbol{k}) = \pm\sqrt{|h(\boldsymbol{k})|^2+M^2}. \tag{3.45}$$

Accordingly, the energy spectrum at the Dirac point $\boldsymbol{K}$ is changed to

$$E(\boldsymbol{K}) = \pm\sqrt{|h(\boldsymbol{K})|^2+M^2} = \pm\sqrt{|0|^2+M^2} = \pm M. \tag{3.46}$$

The corresponding closed gap at the Dirac point $\boldsymbol{K}$ is now gapped out due to $|M|$. Also, at the other Dirac point $\boldsymbol{K}$',

$$E(\boldsymbol{K}') = \pm\sqrt{|h(\boldsymbol{K}')|^2+M^2} = \pm\sqrt{|0|^2+M^2} = \pm M. \tag{3.47}$$

Thus, both Dirac cones are gapped out due to $|M|$. Put differently, $|M|$ turns the massless Dirac fermions into massive ones.

The effect of $|M|$ is to make the electrons to be localized in sites A or B. Note that the time-reversal symmetry is conserved. Mathematically, this is because the added mass term is not an odd function of $\boldsymbol{k}$. Due to the time-reversal symmetry, chiral edge states can never exist. To break the time-reversal symmetry, an odd function of $\boldsymbol{k}$ should be added to the σ_z component of the Hamiltonian.

3.3.4 System with Broken Time-Reversal Symmetry

In order to break the time-reversal symmetry of the system, Haldane in 1988 introduced a staggered magnetic field so that the net field in the system is zero [86]. This staggered magnetic field is illustrated in Fig. 3.7. The staggered magnetic field is expressed by an imaginary next-nearest-neighbor hopping $\imath t_2$ between the A-A sites or B-B sites, with the shown counterclockwise pattern. The hopping directions are shown with the orientations of the arrows. The hopping in the opposite direction is expressed by changing the sign of the hopping amplitude. Note that all hoppings share the same chirality, and hence the net magnetic field is zero. The next-nearest-neighbor vectors $\boldsymbol{d}_1, \boldsymbol{d}_2$, and $\boldsymbol{d}_3$ are given by

$$\boldsymbol{d}_j = \sqrt{3}\left(\cos\left(\frac{\pi}{2}+\frac{2\pi}{3}j\right), \sin\left(\frac{\pi}{2}+\frac{2\pi}{3}j\right)\right), \tag{3.48}$$

for $j = 1, 2$ and 3. The corresponding Hamiltoninan $H_{\mathrm{Hal}}(\boldsymbol{k})$ is

$$H_{\mathrm{Hal}}(\boldsymbol{k}) = H_0(\boldsymbol{k}) + M\sigma_z + 2t_2 \sum_j \sigma_z \sin(\boldsymbol{k}\cdot\boldsymbol{d}_j). \tag{3.49}$$

The second term breaks the bipartite symmetry, and the third term breaks the time-reversal symmetry. Mathematically, the reason why the third term breaks the time-reversal symmetry is that it is an odd function of $\boldsymbol{k}$.

At one of the Dirac points, $\boldsymbol{k}$=$\boldsymbol{K}$, the σ_z component of $H_{\mathrm{Hal}}(\boldsymbol{K})$ is

$$\begin{aligned} M + 2t_2 \sum_i \sin\left(\boldsymbol{K}\cdot\boldsymbol{d}_i\right) &= M + 2t_2\left(\sin\left(0+\frac{2\pi}{3}\right) + \sin\left(-\pi-\frac{\pi}{3}\right) + \sin\left(\pi-\frac{\pi}{3}\right)\right) \\ &= M + 2t_2\left(\frac{\sqrt{3}}{2}+\frac{\sqrt{3}}{2}+\frac{\sqrt{3}}{2}\right) \\ &= M + 3\sqrt{3}t_2. \end{aligned} \tag{3.50}$$

Thus, when $t_2 = -\dfrac{M}{3\sqrt{3}}$, $H_{\mathrm{Hal}}(\boldsymbol{K}) = H_0(\boldsymbol{K}) = 0$ and the gap closes at the Dirac point $\boldsymbol{K}$. Similarly, at the other Dirac point, $\boldsymbol{k}$=$\boldsymbol{K}$', the σ_z component of $H_{\mathrm{Hal}}(\boldsymbol{K}')$ is

$$\begin{aligned} M + 2t_2 \sum_i \sin\left(\boldsymbol{K}' \cdot \boldsymbol{d}_i\right) &= M + 2t_2 \left(\sin\left(0 - \frac{2\pi}{3}\right) + \sin\left(-\pi + \frac{\pi}{3}\right) + \sin\left(\pi + \frac{\pi}{3}\right) \right) \\ &= M + 2t_2 \left(-\frac{\sqrt{3}}{2} - \frac{\sqrt{3}}{2} - \frac{\sqrt{3}}{2} \right) \\ &= M - 3\sqrt{3}t_2. \end{aligned} \tag{3.51}$$

Thus, when $t_2 = \dfrac{M}{3\sqrt{3}}$, $H_{\mathrm{Hal}}(\boldsymbol{K}') = H_0(\boldsymbol{K}') = 0$ and the gap also closes at $\boldsymbol{K}$'. Except for these conditions, two bands do not touch each other. This fact indicates that the topological invariant can be defined so that it detects the change of the phase of the system only at $t_2 = \pm\dfrac{M}{3\sqrt{3}}$. The existence of chiral edge states can be understood by drawing the band structure. The band structures for ribbons with two different lattice terminations, armchair and zigzag, are illustrated in Fig. 3.8 and Fig. 3.9, respectively. Here, $t_1 = 1, M = 0.2$, and $k_x \in [-\pi, \pi]$. The next-nearest neighbor hopping amplitudes t_2 are 0, 0.2, and 0.4 from the left to the right. The edge or surface states appear when the gap closes, which indicates that the system is in the topological phase. The band crossing occurs at $k_x = 0$ for an armchair-type ribbon, and $k_x = \pi$ for a zigzag-type ribbon. These topologically protected Dirac cones appear when the system enters the topological phase. An example of the corresponding edge state in an armchair-type ribbon of graphene with 1800-site is shown in Fig. 3.10. The size of red dots represents the relative electron amplitude (probability amplitude magnitude squared) of one of the zero-energy modes at each lattice site and the gray dots represent the lattice points. PBC and OBC are used for the horizontal and vertical direction, respectively. The electron amplitude of the zero-energy mode is high along the edges.

3.3.5 Chern Number in the Haldane Model

As discussed in the previous subsection, the topological invariant can be defined to classify the topology of the Haldane model. In this subsection, one of the most fundamental topological invariants, the Chern number, is introduced to express the topological feature of the Haldane

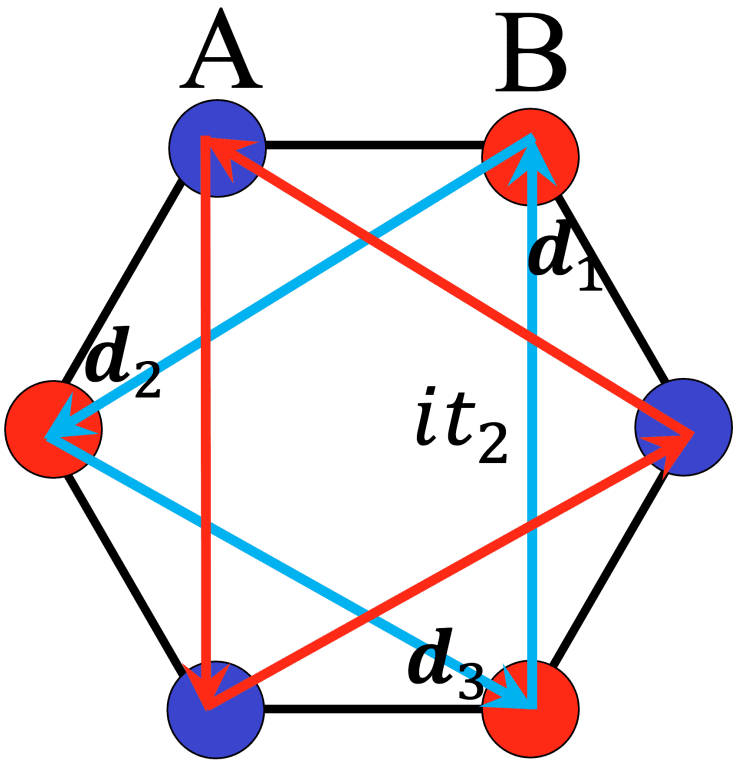

Figure 3.7: The staggered magnetic field introduced by Haldane [86].

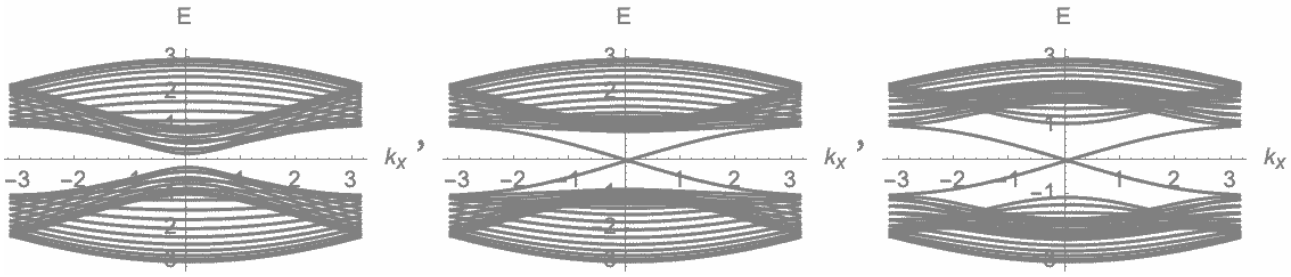

Figure 3.8: The band structures of an armchair-type ribbon. The next-nearest-neighbor hopping amplitudes t_2 are 0, 0.2, 0.4 from the left to the right. The band crossing occurs at $k_x = 0$ when the system enters the topological phase. The corresponding Dirac cone is topologically protected.

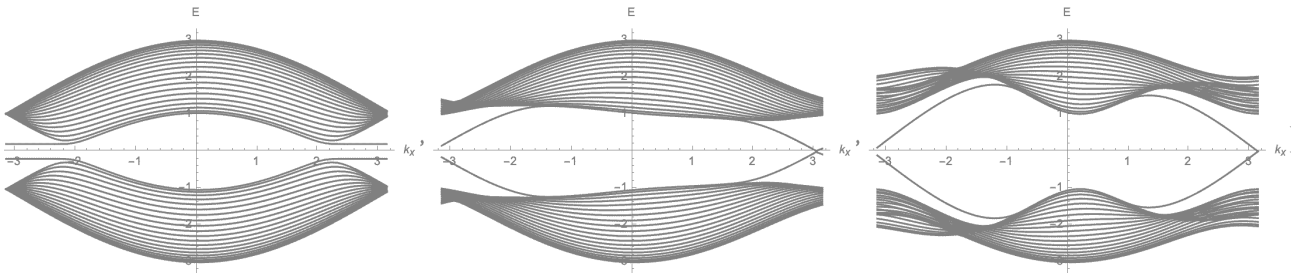

Figure 3.9: The band structures of a zigzag-type ribbon. The next-nearest-neighbor hopping amplitudes t_2 are 0, 0.2, 0.4 from the left to the right. The band crossing occurs at $k_x = \pi$ when the system enters the topological phase. The corresponding Dirac cone is topologically protected.

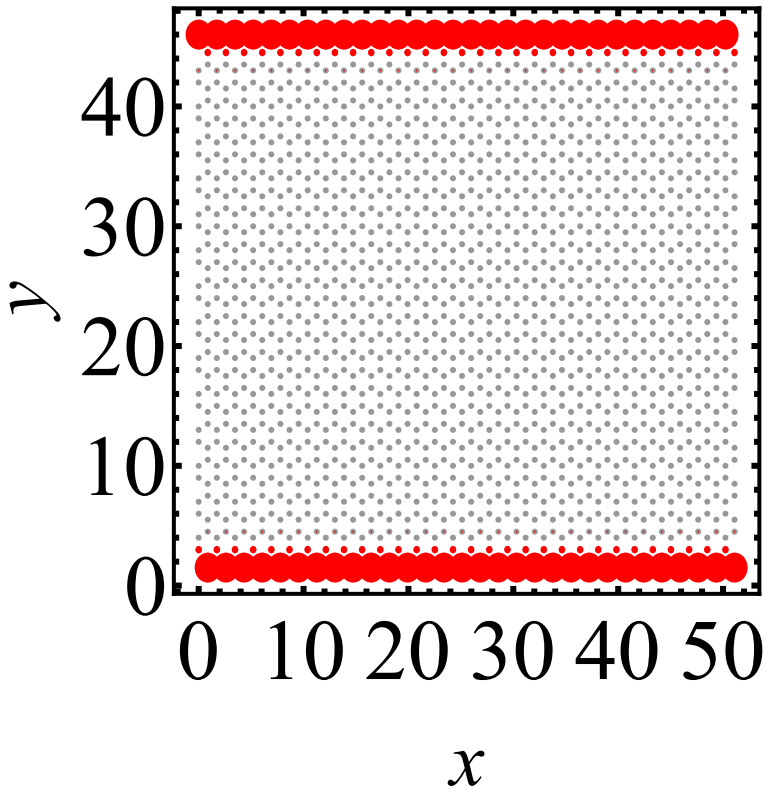

Figure 3.10: The edge state found in an armchair-type ribbon of graphene.

model.

The basics of the Chern number, and related topics such as the Berry phase and the Berry curvature are already explained in Section 3.1. Once again, the Berry phase $\gamma(C)$ for a closed loop C in parameter (momentum) space is

$$\gamma(C) = \oint_C \boldsymbol{A}(\boldsymbol{k}) \cdot \mathrm{d}\boldsymbol{k}, \tag{3.52}$$

with the Berry connection

$$\boldsymbol{A}(\boldsymbol{k}) = \imath \left\langle \psi(\boldsymbol{k}) \middle| \nabla_{\boldsymbol{k}} \psi(\boldsymbol{k}) \right\rangle . \tag{3.53}$$

Here the Berry connection is obtained by the following steps. First, take the derivatives of $|\psi(\boldsymbol{k})\rangle$ with respect to k_x and k_y. Then, take the inner product with $\langle\psi(\boldsymbol{k})|$. For simplicity, C is chosen to be a closed path such that k_x is fixed, and k_y slowly changes from 0 to 2π. After adiabatic time-evolution of an eigenstate $|\psi(\boldsymbol{k})\rangle$ from $t = 0$ to $t = T$ with energy $E(\boldsymbol{k})$, the final quantum state is

$$\exp\left[\imath\gamma(k_x)\right] \exp\left(-\imath \int_0^T E[\boldsymbol{k}(t)]\mathrm{d}t\right) |\psi(\boldsymbol{k})\rangle . \tag{3.54}$$

It is convenient to choose

$$|\psi(n, t=0)\rangle = \int_0^{2\pi} \mathrm{d}k_x \exp\left(\imath k_x n\right) |\psi(k_x, k_y = 0)\rangle \tag{3.55}$$

as an initial state. This initial state expresses a localized state in a single unit cell n. The coefficient for the site n, $\exp\left(\imath k_y n\right)$ is integrated over the first Brillouin zone $k_x \in [0, 2\pi]$. The corresponding final state is given by

$$\begin{aligned} |\psi(n, t=T)\rangle &= \int_0^{2\pi} \mathrm{d}k_x \exp\left(\imath k_x n\right) |\psi(k_x, k_y = 2\pi)\rangle \\ &= \int_0^{2\pi} \mathrm{d}k_x \exp\left(\imath k_x n\right) \exp\left(\imath\gamma(k_x) - \imath\theta(k_x)\right) |\psi(k_x, k_y = 0)\rangle . \end{aligned} \tag{3.56}$$

Here, $\theta(k_x) = \displaystyle\int_0^T E[k_x, k_y(t)]\mathrm{d}t$ is called the dynamical phase. Due to $E(k_x) = E(k_x + 2\pi)$, $\theta(k_x)$ is a periodic function of k_x:

$$\begin{aligned} \theta(k_x + 2\pi) &= \int_0^T E[k_x + 2\pi, k_y(t)]\mathrm{d}t \\ &= \int_0^T E[k_x, k_y(t)]\mathrm{d}t \\ &= \theta(k_x). \end{aligned} \tag{3.57}$$

Then paying attention to the inside of the exponential in Eq. (3.56), the Berry phase needs to be a periodic function modulo 2π. Put differently, there is a freedom of choosing the Berry phase with the restriction

$$\gamma(k_x + 2\pi) - \gamma(k_x) = 2\pi W. \tag{3.58}$$

Here W is an integer, corresponding to the Chern number explained earlier in this chapter. For simplicity, by choosing $\theta(k_x)$ so that

$$\theta(k_x) = \gamma(k_x) - W k_x, \tag{3.59}$$

Eq. (3.56) can be rewritten as

$$\begin{aligned} |\psi(n, t = T)\rangle &= \int_0^{2\pi} \mathrm{d}k_x \exp\left(\imath k_x (n + W)\right) |\psi(k_x, k_y = 0)\rangle \\ &= |\psi(n + W, t = 0)\rangle \,. \end{aligned} \tag{3.60}$$

At the initial state $t = 0$, $W = 0$. After the adiabatic cycle, $t = T$, and the wave function is shifted over by W unit cells, which indicates the pumping of W units of charge.

The above discussion can be stated concisely using the Berry curvature $\Omega(\boldsymbol{k})$ as elaborated below. The Berry curvature $\Omega(\boldsymbol{k})$ is gauge-independently defined by

$$\begin{aligned} \Omega(\boldsymbol{k}) &= \nabla_{\boldsymbol{k}} \times \boldsymbol{A}(\boldsymbol{k}) \\ &= [\left\langle \frac{\partial \psi(\boldsymbol{k})}{\partial k_x} \middle| \frac{\partial \psi(\boldsymbol{k})}{\partial k_y} \right\rangle - \left\langle \frac{\partial \psi(\boldsymbol{k})}{\partial k_y} \middle| \frac{\partial \psi(\boldsymbol{k})}{\partial k_x} \right\rangle]. \end{aligned} \tag{3.61}$$

The Stokes theorem gives

$$\begin{aligned} 2\pi W &= \gamma(2\pi) - \gamma(0) \\ &= \iint_{\mathrm{BZ}} \Omega(\boldsymbol{k}) \cdot \mathrm{d}\boldsymbol{S}. \end{aligned} \tag{3.62}$$

The phase diagram of the system is drawn using the Chern number. The Chern number W is calculated by conducting the area integration of the Berry curvature over the first Brillouin zone as

$$W = \frac{1}{2} \iint_{\mathrm{BZ}} \boldsymbol{\Omega}(\boldsymbol{k}) \cdot \mathrm{d}\boldsymbol{S}. \tag{3.63}$$

In the Haldane model, the Berry curvature contributes to this integral only around the Dirac points. In fact, the sign of the Berry curvature for the two Dirac points changes at the

phase boundary $t_2 = \pm\frac{M}{3\sqrt{3}}$. The examples of the Berry curvature for the Haldane model are plotted for $k_x \in [-\pi, \pi], k_y \in [-\pi, \pi]$ in Fig. 3.11. The fixed parameters are $t_1 = 1$ and $M = 0.2$. The next-nearest-neighbor hopping amplitude t_2 is -0.1, -0.05, 0.0, 0.05 and 0.1 from the upper left to the lower right. When $\frac{t_2}{M} > \frac{1}{3\sqrt{3}}$, the Berry curvature for the two Dirac points are both positive (to be specific, the contributions to the Chern number are both $\frac{1}{2}$). At $\frac{t_2}{M} = \frac{1}{3\sqrt{3}}$, the Berry curvature for one of the Dirac points is zero. When $\frac{1}{3\sqrt{3}} > \frac{t_2}{M} > -\frac{1}{3\sqrt{3}}$, the Berry curvature for one of the two Dirac points is positive, while the other is negative (one of them contributes to the Chern number by $\frac{1}{2}$, and the other by $-\frac{1}{2}$). At $\frac{t_2}{M} = -\frac{1}{3\sqrt{3}}$, the Berry curvature for one of the two Dirac points is zero (the opposite one compared to the $\frac{t_2}{M} = \frac{1}{3\sqrt{3}}$ case). When $\frac{t_2}{M} < -\frac{1}{3\sqrt{3}}$, the Berry curvature for the two Dirac points are both negative (the contributions to the Chern number are both $-\frac{1}{2}$). The phase diagram can be drawn efficiently by neglecting the integration other than around the Dirac points.

3.3.6 Parameter Dependence of Chern Number

In this subsection, the parameter dependence of the Chern number is illustrated. The topology of the system depends upon the system parameters, namely, the on-site energy M and the next-nearest-neighbor hopping amplitude t_2. Here, t_1 is set to be unity and the energy units of M and t_2 are commonly t_1. For calculating the dependence of the parameters of the Chern number, there is an efficient method proposed by Fukui *et al.* in 2005 [89]. The essence of Fukui's method is briefly explained below. In this scheme, the Brillouin zone is approximated by a coarsely discretized one. The Hamiltonian is numerically calculated only on a set of discrete points chosen appropriately within the Brillouin zone. Let the lattice points $k_l = (k_{j_1}, k_{j_2})(l = 1, \ldots, N_1 N_2)$ on the discrete Brillouin zone to be described by

$$k_{j_\mu} = \frac{2\pi j_\mu}{q_\mu N_\mu}, \tag{3.64}$$

where j_μ runs from 0 to $N_\mu - 1$. Assuming that $|n(k_l + N_\mu \hat{\mu})\rangle = |n(k_l)\rangle$, where $\hat{\mu}$ is a vector along the μ axis with the magnitude $\frac{2\pi}{q_\mu N_\mu}$. Setting $N_\mu = q_\nu N_B (\mu \neq \nu)$, the unit plaquette

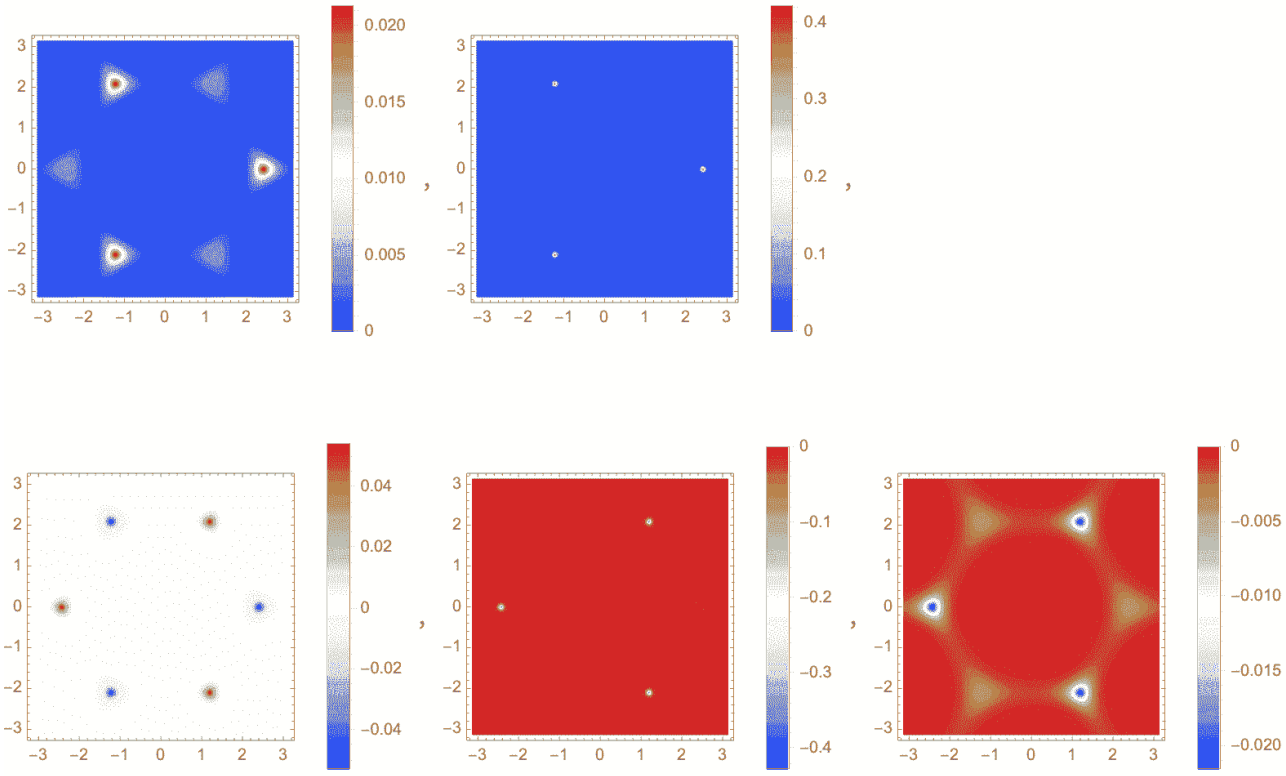

Figure 3.11: The Berry curvature of the Haldane model plotted for $k_x \in [-\pi, \pi]$ and $k_y \in [-\pi, \pi]$. The fixed parameters are $t_1 = 1$ and $M = 0.2$. The next-nearest-neighbor hopping amplitude t_2 is -0.1, -0.05, 0.0, 0.05, and 0.1 from the upper left to the lower right.

is a square of the area $\frac{2\pi}{q_1 q_2 N_B}$. First, the link variable is defined as

$$U_\mu(k_l) = \frac{1}{\mathcal{N}_\mu(k_l)} \langle n(k_l) \,|\, n(k_l + \hat{\mu}) \rangle \,, \tag{3.65}$$

where the normalization constant is

$$\mathcal{N}_\mu(k_l) = |\langle n(k_l) \,|\, n(k_l + \hat{\mu}) \rangle| \neq 0. \tag{3.66}$$

Using this link variable, a lattice field strength $\tilde{F}_{12}(k_l)$ is defined within the principal branch of the logarithm specified in $-\pi < \frac{1}{\imath}\tilde{F}_{12}(k_l) \leq \pi$ by

$$\tilde{F}_{12}(k_l) = \ln U_1(k_l) U_2(k_l + \hat{1}) U_1(k_l + \hat{2})^{-1} U_2(k_l)^{-1}. \tag{3.67}$$

The Chern number $\tilde{c}_n$ associated with the nth band is gauge-invariantly defined as

$$\tilde{c}_n = \frac{1}{2\pi\imath} \sum_l \tilde{F}_{12}(k_l). \tag{3.68}$$

In the case of the Haldane model, the phase diagram can be approximately obtained by Eq. (3.68) and focusing around the Dirac points. The calculated phase diagram is illustrated in Fig. 3.12. The Chern number is calculated for different t_2 and M. The horizontal axis and the vertical axis are t_2 and M, respectively. In Fig. 3.13 the phase diagram is compared with the analytically derived phase boundaries $t_2 = \pm\frac{M}{3\sqrt{3}}$. The phase diagram is well reproduced by the numerical calculation.

3.4 Kitaev Model

The Kitaev model is the simplest model which exhibits unpaired zero-energy Majorana fermions (Majorana 'zero modes'), proposed by Kitaev in 2001 [87]. Majorana fermions are their own antiparticles, described by the Majorana operator γ, which satisfies $\gamma^\dagger = \gamma$. Namely, the Hermitian conjugate of the Majorana operator is itself, and γ is neither creation nor annihilation operator in the usual sense. Due to this property, Majorana operators obey unusual anticommutation relations. The Kitaev model describes a one-dimensional p-wave superconducting wire of spinless fermions,

$$\mathcal{H}_{\text{1Dwire}} = \sum_j [-t(c_j^\dagger c_{j+1} + c_{j+1}^\dagger c_j) - \mu c_j^\dagger c_j + |\Delta|(c_{j+1}^\dagger c_j^\dagger + c_j c_{j+1})]. \tag{3.69}$$

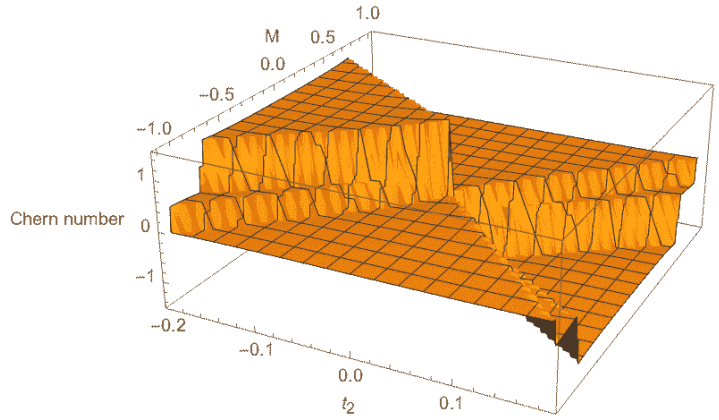

Figure 3.12: Topological phase diagram of the Haldane model for an armchair-type ribbon of graphene, where the first Chern number is plotted as a function of t_2 and M. Topological phase transitions can be seen where the Chern number changes between 1 and -1.

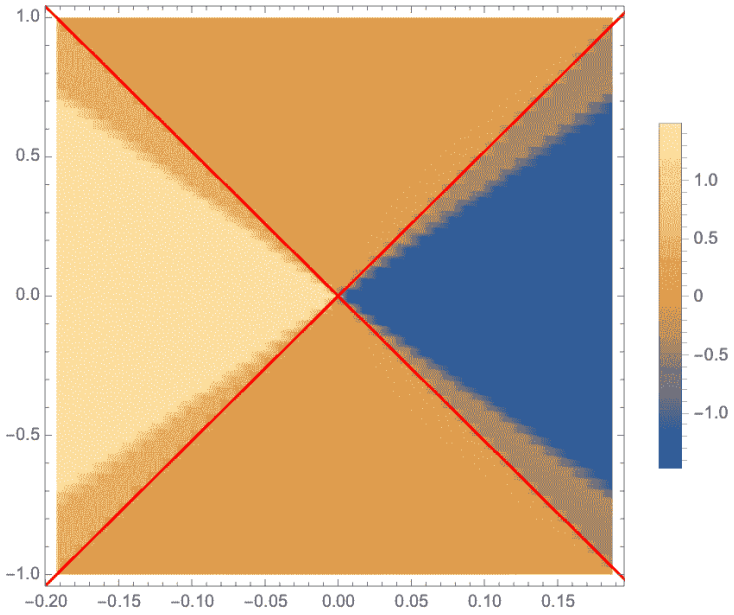

Figure 3.13: Top view of Fig. 3.12, in comparison with the analytically derived phase boundaries (red lines).

The operator $c_j^\dagger(c_j)$ corresponds to the creation (annihilation) operator of a fermion at the jth site. Here, j runs from 1 to L where L is the length of the system. We set the lattice constant to unity. Using the transformation,

$$c_j = \frac{1}{2}(\gamma_{2j-1} + \imath\gamma_{2j}) \tag{3.70}$$

or

$$c_j^\dagger = \frac{1}{2}(\gamma_{2j-1} - \imath\gamma_{2j}), \tag{3.71}$$

the fermion operators are replaced by Majorana operators γ_j. Here, $\gamma_j^\dagger(\gamma_j)$ corresponds to the creation (annihilation) operator of a Majorana fermion at the jth site. The $2j$ runs from 1 to $2L$. Using the usual anticommutation relations for fermion operators, one finds the anticommutation relations for the Majorana operators as

$$\{\gamma_j^\dagger, \gamma_{j'}\} = \{\gamma_j, \gamma_{j'}\} = \{\gamma_j^\dagger, \gamma_{j'}^\dagger\} = 2\delta_{jj'}. \tag{3.72}$$

The Kitaev Hamiltonian can be rewritten in terms of Majorana operators γ_j as

$$\mathcal{H}_{\text{1Dwire}} = \frac{\imath}{2}\sum_j(-\mu\gamma_{2j-1}\gamma_{2j} + (t + |\Delta|)\gamma_{2j}\gamma_{2j+1} + (-t + |\Delta|)\gamma_{2j-1}\gamma_{2j+2}). \tag{3.73}$$

Note that for $j = 1, 2, 3, \ldots, L$,

$$\gamma_{2j-1} = c_j + c_j^\dagger = 2\Re c_j \tag{3.74}$$

and

$$\gamma_{2j} = \frac{1}{\imath}(c_j - c_j^\dagger) = 2\Im c_j. \tag{3.75}$$

Put differently, the fermion operator at the jth site is decomposed into two Majorana fermions: The real part of the fermion operator is mapped onto the $(2j-1)$th Majorana operator and the imaginary part of the fermion operator is mapped onto the $(2j)$th Majorana operator. Thus, a Majorana fermion is half of a normal fermion. As a result, a fermionic state can be obtained as a superposition of two Majorana fermions.

The Kitaev model exhibits Majorana edge modes with the condition $|\mu| < 2t$, as explained below. First consider one of the simplest cases, (i) $\mu < 0, |\Delta| = t = 0$:

$$\mathcal{H}_{\text{1Dwire}} = -\mu\frac{\imath}{2}\sum_j \gamma_{2j-1}\gamma_{2j} = -\mu\frac{\imath}{2}(\gamma_1\gamma_2 + \gamma_3\gamma_4 + \gamma_5\gamma_6 + \ldots + \gamma_{2L-1}\gamma_{2L}). \tag{3.76}$$

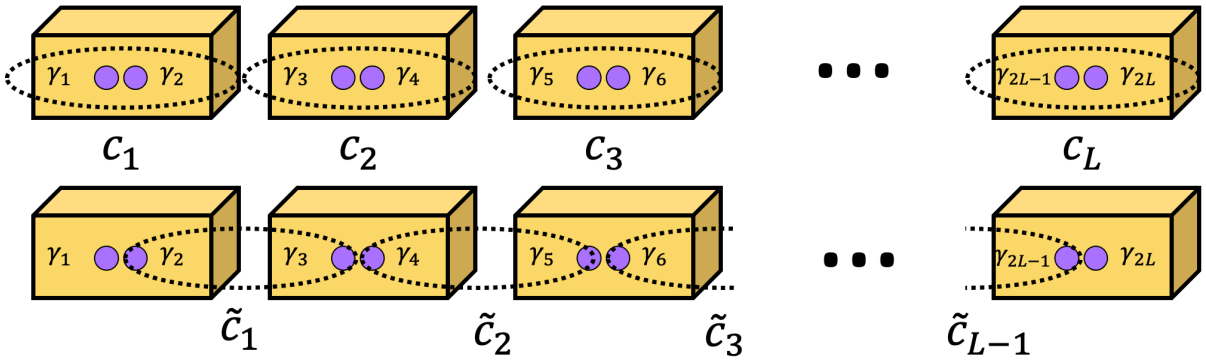

Figure 3.14: Majorana fermions in the Kitaev model.

Note that the adjacent Majorana operators are coupled to each other including the edges and this is a trivial phase. This situation is illustrated in the upper graph of Fig. 3.14. Next consider (ii) $\mu = 0, |\Delta| = t > 0$. The Hamiltonian in Eq. (3.73) reduces to

$$\mathcal{H}_{\text{1Dwire}} = \imath t \sum_j \gamma_{2j}\gamma_{2j+1} = \imath t(\gamma_2\gamma_3 + \gamma_4\gamma_5 + \gamma_6\gamma_7 + \ldots + \gamma_{2L-2}\gamma_{2L-1}). \tag{3.77}$$

Note that two adjacent Majorana operators on adjacent sites are coupled to each other; however, two spatially separated Majorana operators at the edges of the system γ_1 and γ_{2L} have disappeared from the Hamiltonian. Therefore, a Majorana fermion can occupy either site without any energy cost. This implies the existence of the zero-energy Majorana edge modes. This situation is illustrated in the lower graph of Fig. 3.14.

The question that immediately arises is what condition is required for the system to allow the Majorana edge or surface modes. In order to provide the answer, the BdG equations of the Kitaev model need to be considered. Utilizing translational symmetry of the system, Fourier transform is conducted as follows:

$$\sum_i c_i^\dagger c_i = \sum_k c_k^\dagger c_k, \tag{3.78}$$

$$\sum_i c_{i+1}^\dagger c_i = \sum_k \mathrm{e}^{\imath k} c_k^\dagger c_k, \tag{3.79}$$

$$\sum_i c_i c_{i+1} = \sum_k (\mathrm{e}^{-\imath k} c_k c_{-k} + \mathrm{e}^{\imath k} c_{-k} c_k) = -\sum_k c_k c_{-k} 2\imath \sin k. \tag{3.80}$$

As a result, the BdG representation is obtained as

$$H_{\mathrm{BdG}} = \begin{pmatrix} -\mu - 2t\cos k & 2\imath|\Delta|\sin k \\ -2\imath|\Delta|\sin k & \mu + 2t\cos k \end{pmatrix} \tag{3.81}$$

The bulk spectrum $\epsilon(k)$ is given by the eigenvalues of this BdG Hamiltonian, which are

$$\epsilon(k) = \pm\sqrt{(2t\cos k + \mu)^2 + 4|\Delta|^2\sin^2 k}. \tag{3.82}$$

Note that this bulk spectrum is invariant under transformation $q \mapsto q+\pi$ and $\mu \mapsto -\mu$. This means $(2t\cos k + \mu)^2 \mapsto (-2t\cos k - \mu)^2 = (2t\cos k + \mu)^2$, $\sin^2 k \mapsto (-\sin k)^2 = \sin^2 k$, thus the inside of the square root in the bulk spectrum does not change under the transformation. Also, the bulk spectrum is invariant under transformation $t \mapsto -t$ and $\mu \mapsto -\mu$, which yields $(2t\cos k+\mu)^2 \mapsto (-2t\cos k-\mu)^2 = (2t\cos k+\mu)^2$, $\sin^2 k \mapsto \sin^2 k$. These invariant properties indicate that the sign of μ and t does not affect the gap closing condition $\epsilon(k) = 0$, which is $2|t| = |\mu|$. Paying attention to $k = 0, \pi/2$, and π, the corresponding bulk spectrum is $\epsilon(0) = \pm\sqrt{(2t+\mu)^2} = \pm|2t+\mu|$, $\epsilon(\pi/2) = \pm\sqrt{\mu^2 + 4|\Delta|^2}$, and $\epsilon(\pi) = \pm\sqrt{(2t-\mu)^2} = \pm|2t-\mu|$. Thus the gap at $k = 0$ and π closes when $2t = -\mu$ and $2t = \mu$, respectively. And the gap at $k = \pi/2$ closes when $\mu = 0$ and $\Delta = 0$.

Using the Pauli matrices,

$$\sigma_x = \begin{pmatrix} 0 & 1 \\ 1 & 0 \end{pmatrix}, \quad \sigma_y = \begin{pmatrix} 0 & -\imath \\ \imath & 0 \end{pmatrix}, \quad \sigma_z = \begin{pmatrix} 1 & 0 \\ 0 & -1 \end{pmatrix}, \tag{3.83}$$

the BdG Hamiltonian in Eq. (3.81) can be rewritten as

$$H_{\mathrm{BdG}} = (-\mu - 2t\cos k)\sigma_z - 2\Delta\sin k\sigma_y = \begin{pmatrix} 0 & -2\Delta\sin k & -\mu - 2t\cos k \end{pmatrix} \begin{pmatrix} \sigma_x \\ \sigma_y \\ \sigma_z \end{pmatrix}. \tag{3.84}$$

Thus the projection of the BdG Hamiltonian onto the Pauli matrix space yields the σ_x component zero, the σ_y component $-2\Delta\sin k$, and the σ_z component $-\mu - 2t\cos k$. The parametric plot of these components in $\sigma_y - \sigma_z$ two-dimensional space yields an ellipse as illurstrated in Fig. 3.15, where the wave number k runs from $-\pi$ to π, for $t = 1, \Delta = 0.5$. The ellipse becomes a circle when $\Delta = t$. When $|\mu| > 2t$, the ellipse does not enclose the

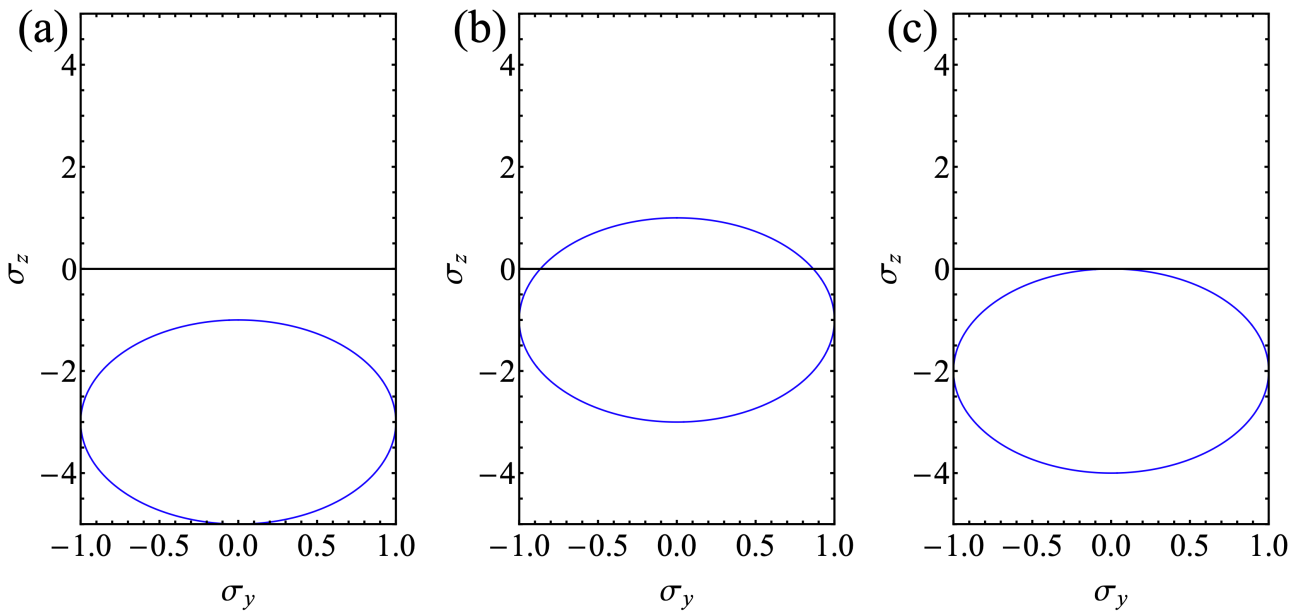

Figure 3.15: The Kitaev model BdG Hamiltonian projected onto the Pauli matrix space is represented by an ellipse (or a circle when $\Delta = t$). The parametric plot is drawn for $k \in [-\pi, \pi]$. The fixed parameters are $\Delta/t = 0.5$, (a) $\mu/t = 3$, (b) $\mu/t = 1$, and (c) $\mu/t = 2$.

origin of the Pauli matrix space. On the other hand, when $|\mu| < 2t$, the ellipse encloses the origin. When $\mu = \pm 2t$, the ellipse just touches the origin. This critical condition $\mu = \pm 2t$ corresponds to vanishing of the vector $\Big(0, \quad -2\Delta \sin k, \quad -\mu - 2t \cos k\Big)$ at $k = 0$ for $\mu = -2t$ and at $k = \pi$ for $\mu = 2t$. As mentioned earlier in this section, the Kitaev model exhibits Majorana edge modes when $|\mu| < 2t$. In terms of the Pauli matrix space representation, zero-energy Majorana edge modes appear when the ellipse does not enclose the origin of the Pauli matrix space. Unless $|\mu| < 2t$, the ellipse never encloses the origin of the Pauli matrix space. As a summary of this section, the Kitaev model exhibits zero-energy Majorana edge modes, and its Pauli matrix space representation helps understanding the topological features of the system.

4 Properties of Quasicrystals

QCs, the main subject of this thesis, are unconventional materials whose structures are without any periodicity, but show Bragg peaks and peculiar rotational symmetry that is forbidden by traditional crystallography. These unconventional characters lead to interesting physical properties, such as interplay of fractality and topology. This chapter aims to give an overview of the definition and basic properties of QCs and their approximants. As examples of QCs, one-dimensional Fibonacci lattice, two-dimensional Penrose QC, and two-dimensional AB QC are briefly explained. Finally, as a preliminary study, conventional s-wave SC in AB QC is examined by solving the BdG equations self-consistently.

4.1 Definition of Quasicrystals

As introduced in Ch. 1, QCs exhibit Bragg peaks without periodic structure and are defined by quasiperiodicity. They are in stark contrast to conventional crystals that have periodic structures accompanied by a set of corresponding unit vectors. Such conventional crystals are generated by repeatedly translating the unit cell, which allows one to utilize Fourier transform. Meanwhile, QCs do not have any periodicity and accordingly, Fourier transform is not applicable. Thus, the Bloch theorem [44] does not hold, and interesting electronic properties such as unusual conductive, thermal, and vibrational properties, strictly localized states, and pseudogaps emerge. QCs have rotational symmetry such as fivefold, eightfold, and tenfold, which are impossible in ordinary crystals. Most fundamental examples of QCs are, Fibonacci lattice, Penrose QC, and AB QC. Penrose QC has fivefold rotational symmetry while AB QC has eightfold rotational symmetry. Although there are several ways to generate a given QC, in general, a QC can be expressed as a projection of periodic lattice structure in higher dimensions onto lower-dimensional space. For example, the Fibonacci lattice or chain can be generated by taking a projection of a two-dimensional square lattice onto a one-

dimensional line. The number of nearest-neighbor sites around a given lattice site ('vertex') is called the coordination number and labeled as z, which varies from site to site. For example, in the case of AB QC, $z = 3, 4, 5, 6, 7, 8$.

4.2 Fibonacci Lattice

Fibonacci lattice is a system where the on-site chemical potentials on the lattice sites are associated with the Fibonacci sequence. The Fibonacci sequence goes as 0, 1, 1, 2, 3, 5, 8, 13, 21, 34, 55, 89, 144, ... With the initial condition, $F_0 = 0, F_1 = 1$, the nth number in the Fibonacci sequence F_n is given by $F_n = F_{n-1} + F_{n-2}$. The golden ratio has a strong connection with the Fibonacci sequence. The ratio of two consecutive Fibonacci numbers approaches the golden ratio in the limit of index n going to infinity.

The on-site chemical potentials in a Fibonacci lattice are generated as follows. First, let two kinds of chemical potentials be μ_A and μ_B, and the first generation of the chemical potential be μ_A. Using the substitution rule, $\mu_A \to \mu_B$, $\mu_B \to \mu_A\mu_B$, subsequent generations are generated. The gth generation sequence has length N_g which satisfies $N_g = N_{g-1} + N_{g-2}$. Thus, the lattice length N_g forms the Fibonacci sequence, and this sequence of on-site chemical potentials is called the Fibonacci potential. In Fig. 4.1, the on-site chemical potentials in a Fibonacci lattice are shown for $g = 1, 2, 3, 4, 5$. The red (blue) component of the gth generation sequence matches with the $(g-2)$th ($(g-1)$th) generation sequence.

It is important to note that the Fibonacci lattice is an example of a one-dimensional quasiperiodic system. In Fig. 4.2, the Fibonacci lattice is shown to be composed of red and blue line segments ('tiles'). These two line segments are the fundamental building blocks of the Fibonacci lattice, generating a never-repeating aperiodic pattern. Projection of a strip in a two-dimensional square lattice (gray area in Fig. 4.2) onto a straight line generates a Fibonacci lattice/chain. The two-dimensional space where the square lattice is used for projection and generating the Fibonacci lattice in one dimension is called superspace or hyperspace.

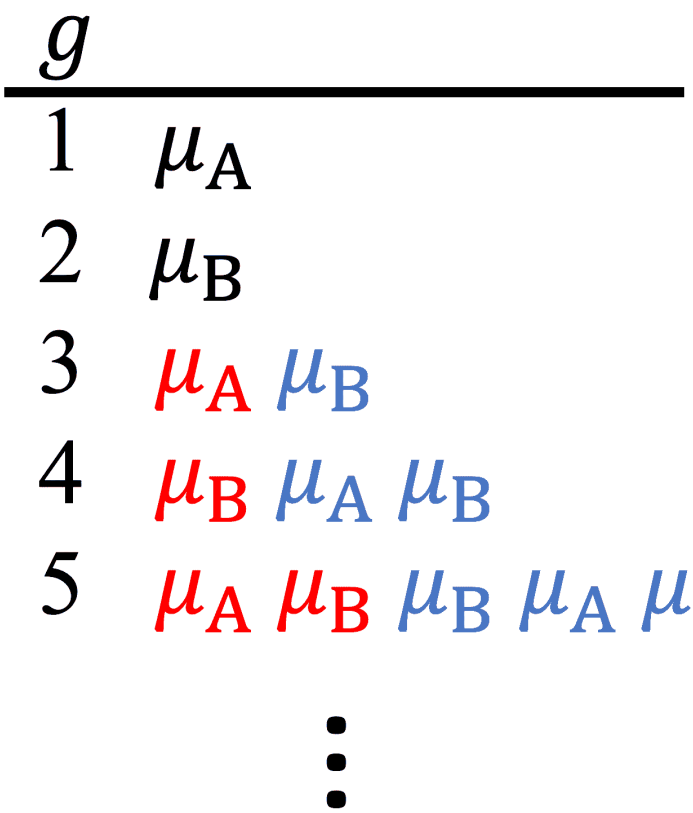

Figure 4.1: The on-site chemical potentials in a Fibonacci lattice for $g = 1, 2, 3, 4, 5$.

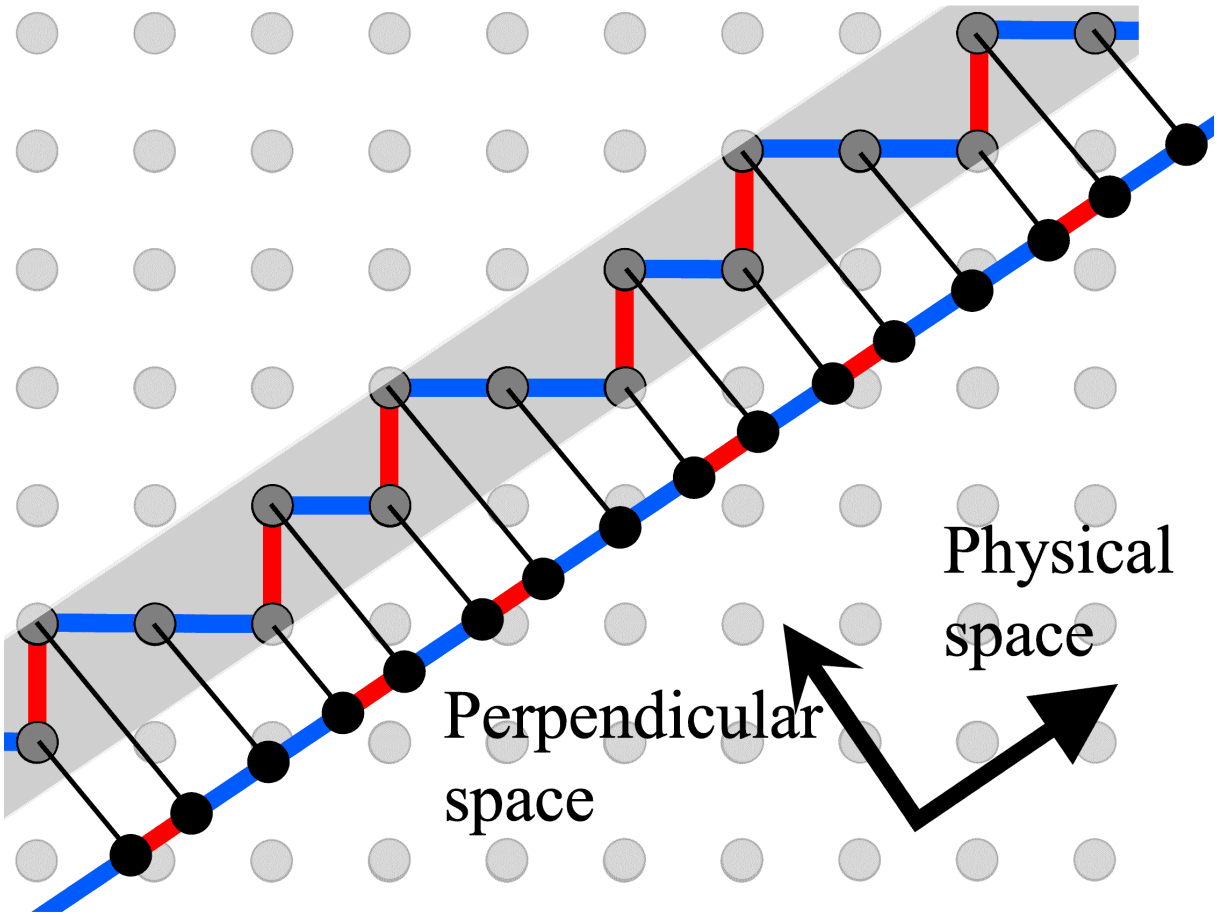

Figure 4.2: Projection method for generating a Fibonacci lattice.

4.3 Fibonacci-Kitaev Model

The Fibonacci-Kitaev model is introduced below as one of the first examples of QCs where TSC has been shown to exist [67]. The Fibonacci-Kitaev model is based upon the Kitaev model. As introduced in Ch. 3, the Kitaev model can be described in terms of the Hamiltonian,

$$\mathcal{H} = \sum_{i=1}^{N-1}(-c_i^\dagger c_{i+1} + \Delta c_i c_{i+1} + \text{H.c.}) + \mu \sum_{i=1}^{N} c_i^\dagger c_i. \tag{4.1}$$

Here, Δ is assumed to be real and $|\Delta| = \Delta$, as this assumption does not lose generality. The hopping amplitude t is set to be unity. In Eq. (4.1), the chemical potential μ is independent of the lattice coordinate i. By replacing the uniform chemical potential μ with the site-dependent chemical potential in a Fibonacci lattice, μ_i,

$$\mathcal{H} = \sum_{i=1}^{N-1}(-c_i^\dagger c_{i+1} + \Delta c_i c_{i+1} + \text{H.c.}) + \sum_{i=1}^{N} \mu_i c_i^\dagger c_i. \tag{4.2}$$

This Hamiltonian describes the Fibonacci-Kitaev model. As mentioned in the previous section, the arrangement of the on-site chemical potentials in a Fibonacci lattice is quasiperiodic. As a result, the Fibonacci-Kitaev model exhibits unconventional physical properties, and its topological phase diagram shows a self-similar fractal structure.

The Fibonacci-Kitaev model in Eq. (4.2) can be rewritten with Majorana fermion operators as the basis using the transformation $c_i = \dfrac{a_i + \imath b_i}{2}$, where a_i and b_i are Majorana operators, $a_i^\dagger = a_i$ and $b_i^\dagger = b_i$. In the TSC phase of this system, two Majorana fermions $Q_a = \sum_i \alpha_i a_i$ and $Q_b = \sum_i \beta_i b_i$ can appear as zero energy modes, where α_i and β_i are the probability amplitudes. The zero energy modes exist when (i) $[Q_a, \mathcal{H}] = [Q_b, \mathcal{H}] = 0$ and (ii) both Q_a and Q_b are normalizable in an infinitely large system. The condition (i) is equivalent to

$$\begin{pmatrix} \alpha_{i+1} \\ \alpha_i \end{pmatrix} = A_i \begin{pmatrix} \alpha_i \\ \alpha_{i-1} \end{pmatrix} \text{ with } A_i = \begin{pmatrix} \dfrac{\mu_i}{1+\Delta} & \dfrac{\Delta - 1}{1+\Delta} \\ 1 & 0 \end{pmatrix}. \tag{4.3}$$

The condition (ii) is examined in terms of the topological invariant $\nu = (-1)^{n_f - 1}$. Only when $\nu = -1$, the condition (ii) is satisfied and the system is in topological phase. Here n_f is the number of eigenstates of $\Lambda^g = \prod_{i=1}^{N_g} A_i$ whose eigenvalues are smaller than unity. Since Λ^g is a

2×2 matrix, $n_f = 0, 1, 2$: $\nu = -1$ for $n_f = 0, 2$ and $\nu = 1$ for $n_f = 1$. Let the two eigenvalues of Λ^g be λ_1, λ_2 where $|\lambda_1| < |\lambda_2|$. Without loss of generality, Δ can be assumed to be real and $\Delta \geq 0$. In order to examine self-similarity, the Lyapunov exponent $\gamma^g(\{\mu_i\}, \Delta)$ can be utilized. The Lyapunov exponent is defined as

$$\gamma^g(\{\mu_i\}, \Delta) = \frac{1}{N_g} \ln |\lambda_2(\{\mu_i\}, \Delta)|. \tag{4.4}$$

Here, $\{\mu_i\}$ is the on-site chemical potential of the Fibonacci lattice. Assuming $0 < \Delta < 1$,

$$\gamma^g(\{\mu_i\}, \Delta) = \gamma^g \left(\left\{ \frac{\mu_i}{\sqrt{1-\Delta^2}} \right\}, 0 \right) - \frac{1}{2} \ln \left(\frac{1+\Delta}{1-\Delta} \right). \tag{4.5}$$

Thus the Lyapunov exponent is given by $\gamma_0^g(\{\mu_i\}) = \gamma^g(\{\mu_i\}, 0)$ with rescaling of μ_i to $\frac{\mu_i}{\sqrt{1-\Delta^2}}$ and a shift by $\frac{1}{2} \ln \left(\frac{1+\Delta}{1-\Delta} \right)$.

The phase boundary between the topological phase and the trivial phase is $|\lambda_2| = 0$ or $\gamma^g = 0$. The critical pairing potential Δ_c obeys the self-consistent equation $\Delta_c = \tanh \gamma_0^g \left(\left\{ \frac{\mu_i}{\sqrt{1-\Delta^2}} \right\} \right)$. The critical pairing potential for the 17th generation is illustrated in Fig. 4.3. The horizontal and the vertical axes are μ_A and μ_B, respectively. When $\Delta = 0$, $\lambda_1 \lambda_2 = \det[\Lambda^g] = \left(\frac{1-\Delta}{1+\Delta} \right)^{N_g} = 1$. Thus $\lambda_2 = \frac{1}{\lambda_1} = \frac{|\mathrm{Tr}[\Lambda^g]| + \sqrt{(\mathrm{Tr}[\Lambda^g])^2 - 4}}{2}$. As a consequence,

$$\gamma_0^g = \begin{cases} \frac{1}{N_g} \cosh^{-1} (|\frac{1}{2} \mathrm{Tr}[\Lambda^g]|) & (|\mathrm{Tr}[\Lambda^g]| > 2), \\ 0 & (|\mathrm{Tr}[\Lambda^g]| \leq 2). \end{cases} \tag{4.6}$$

Here, the nonlinear recursive relation,

$$\mathrm{Tr}[\Lambda^g] = \mathrm{Tr}[\Lambda^{g-1}] \mathrm{Tr}[\Lambda^{g-2}] - \mathrm{Tr}[\Lambda^{g-3}], \tag{4.7}$$

is held, which indicates fractal structure. The fractal dimension is measured using the box-counting method as follows. First step is to rasterize Fig. 4.3 with

$$\overline{c}_\epsilon(\boldsymbol{\mu}) = \epsilon^{-2} \int_{\mathcal{R}_\epsilon(\boldsymbol{\mu})} c(\boldsymbol{\mu}') \mathrm{d}^2 \boldsymbol{\mu}'. \tag{4.8}$$

The integrated region $\mathcal{R}_\epsilon(\boldsymbol{\mu})$ above is a box of side length ϵ centered at $\boldsymbol{\mu} = (\mu_A, \mu_B)$,

$$\mathcal{R}_\epsilon(\boldsymbol{\mu}) = \left[\mu_A - \frac{\epsilon}{2}, \mu_A + \frac{\epsilon}{2} \right] \otimes \left[\mu_B - \frac{\epsilon}{2}, \mu_B + \frac{\epsilon}{2} \right]. \tag{4.9}$$

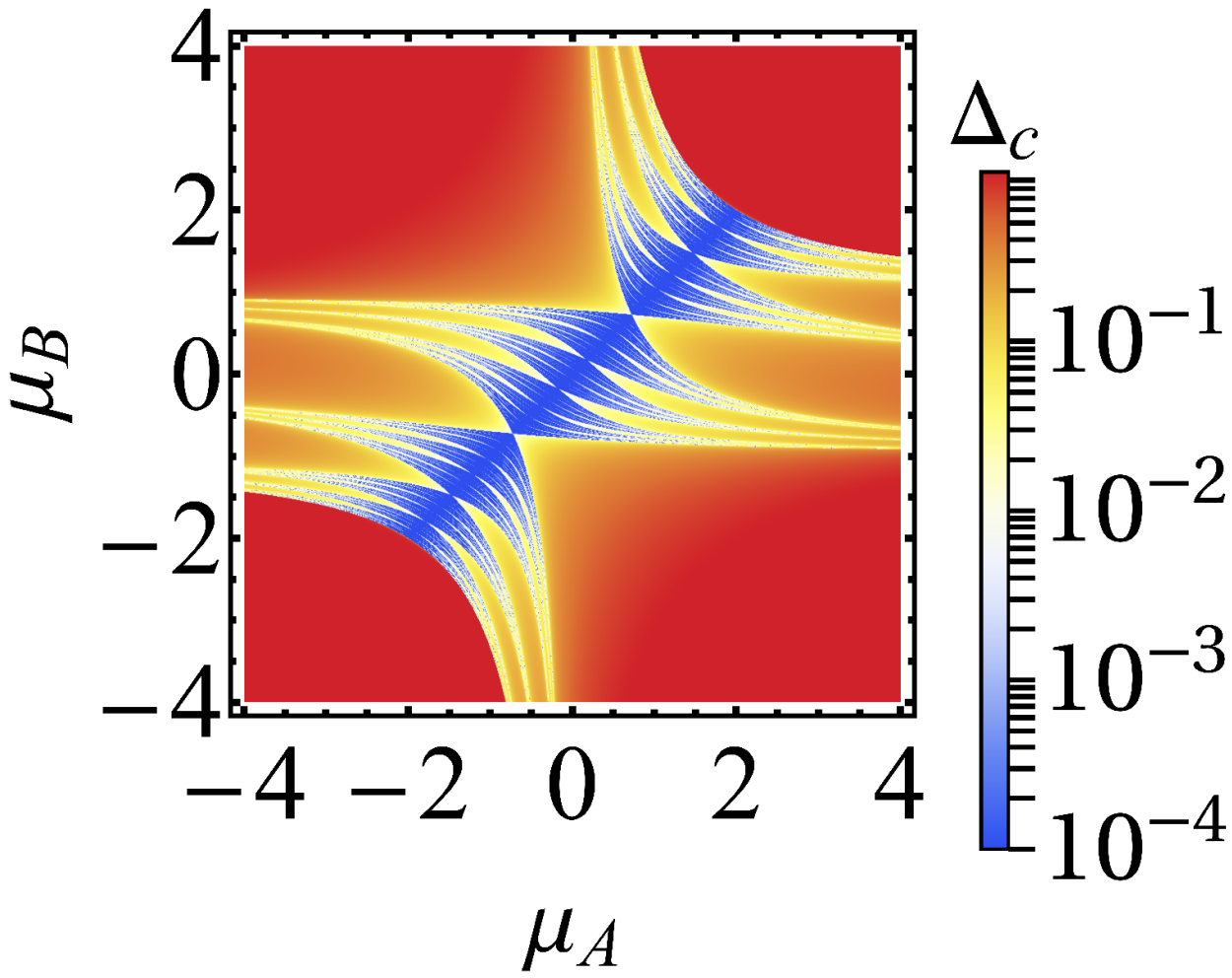

Figure 4.3: Critical pairing potential of the Fibonacci-Kitaev model for the 17th generation exhibiting fractal phase boundaries. The data points with values lower than 10^{-4} are colored by the same color as for 10^{-4}.

From the relation between the box size ϵ and the number of boxes $n(\epsilon)$, $n(\epsilon) \propto \epsilon^{-D}$ determines the box-counting dimension D. The extrapolated value of D in the thermodynamic limit is found to be around 1.7 [67]. This non-integer box-counting dimension indicates that the Fibonacci-Kitaev model exhibits a self-similar fractal structure in its topological phase diagram.

4.4 Penrose Quasicrystal and Approximant

Two of the most well-known examples of QCs are Penrose QC and AB QC. In this section, some basic properties of Penrose QC and approximant are briefly explained.

4.4.1 Basics of Penrose Quasicrystal and Approximant

Penrose QC is a famous example of two-dimensional QCs, whose tiling is illustrated in Fig. 4.4. The vertices of Penrose tiling are the lattice sites of Penrose QC. Penrose tiling was proposed by Penrose in 1974 [90]. After the discovery of Penrose tiling, de Brujin developed an algebraic approach to produce Penrose tiling [91]. As is shown in Fig. 4.4, Penrose tiling can be composed of two rhombuses. One of the two rhombuses is a rhombus with angles of 72 degrees and 108 degrees (colored in blue in Fig. 4.4), and the other rhombus is with angles of 36 degrees and 144 degrees (colored in green in Fig. 4.4). Area ratio of the two rhombuses is $\frac{1+\sqrt{5}}{2}$. This ratio is the well-known golden ratio. The golden ratio is one of the roots of the quadratic equation $x^2 - x - 1 = 0$.

It is impossible to consider a QC with PBC since a QC is not periodic. Therefore, to consider a QC with the PBC, an approximation is required. Approximants are parts of QCs, whose right (upper) and left (lower) edges can be connected with PBC. A QC can be regarded as an infinitely large approximant, and the physical properties of QCs are expected to be similar to that of large approximants. Penrose approximant can be generated, for example, using multigrid algorithm [92, 93], which is used for the results shown below. Coordination numbers in Penrose approximant with PBC are represented by colors in Fig. 4.5. Coordination numbers in Penrose QC and approximant range from 3 to 7. The average coordination number in Penrose QC is exactly four.

Penrose QC is modeled as a quasicrystalline lattice of vertices of Penrose tiling and we use a tight-binding vertex model, whose Hamiltonian is given by

$$\mathcal{H}_0 = -t \sum_{\langle i,j\rangle,\sigma} (c^\dagger_{i\sigma} c_{j\sigma} + c^\dagger_{j\sigma} c_{i\sigma}), \tag{4.10}$$

in which the conduction electron hops from vertex to vertex, along the side of a rhombus. Note that as the side lengths of the two rhombuses are the same, all links connecting vertices

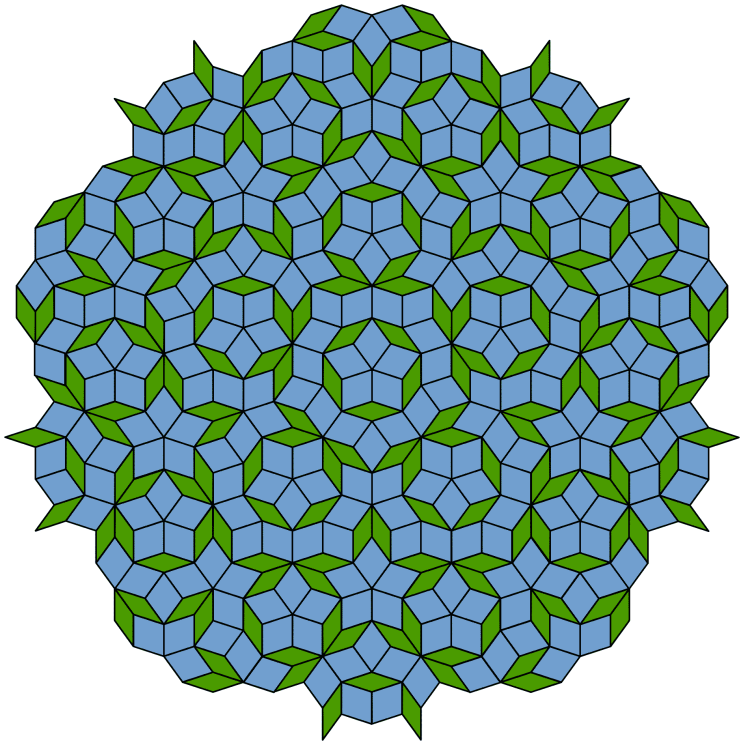

Figure 4.4: A small patch of Penrose tiling, composed of two rhombuses. This figure is a public domain image adopted from Wikipedia. https://en.wikipedia.org/wiki/File:Penrose_Tiling_(Rhombi).svg

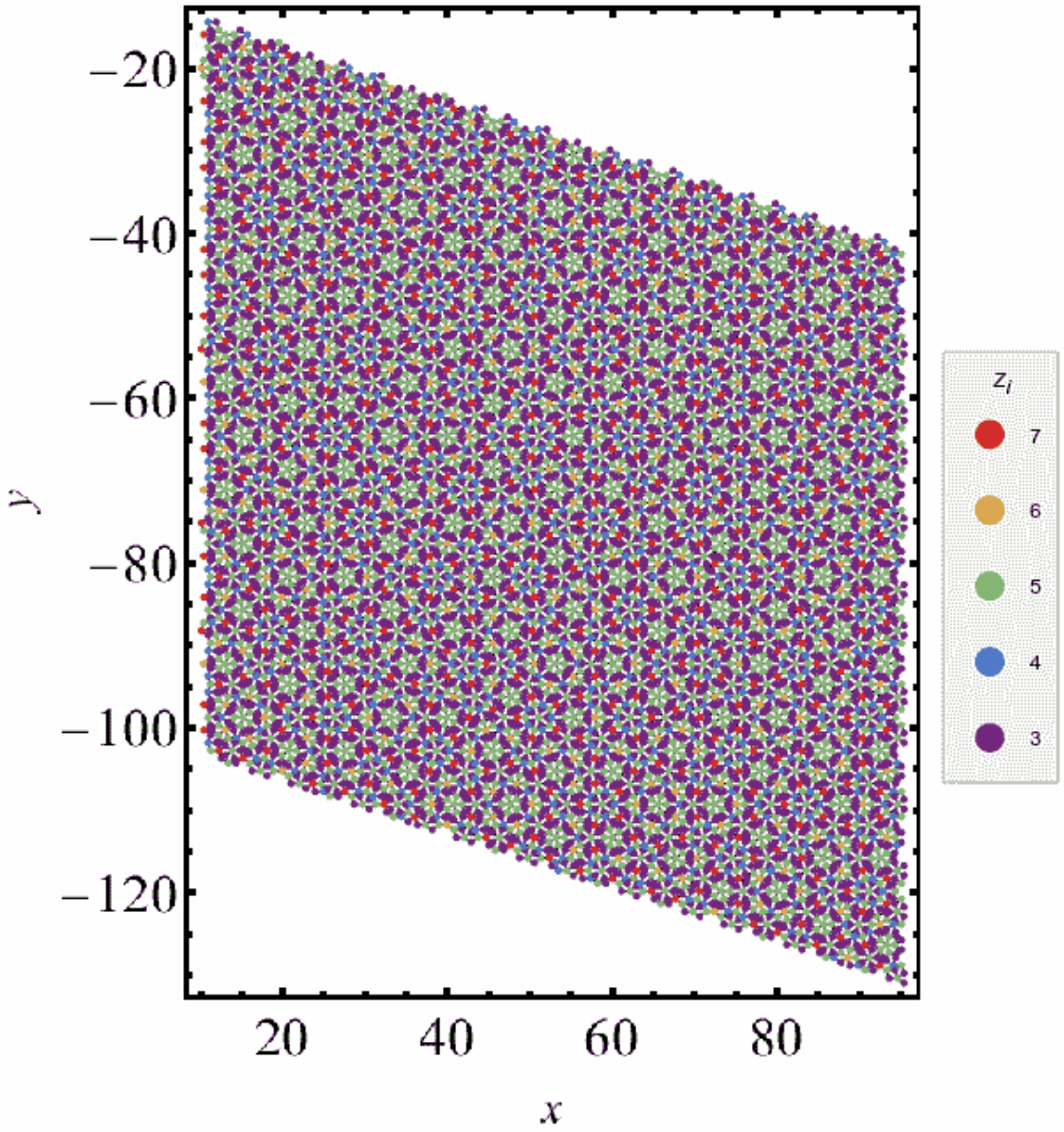

Figure 4.5: Coordination numbers in Penrose approximant with PBC represented by colors.

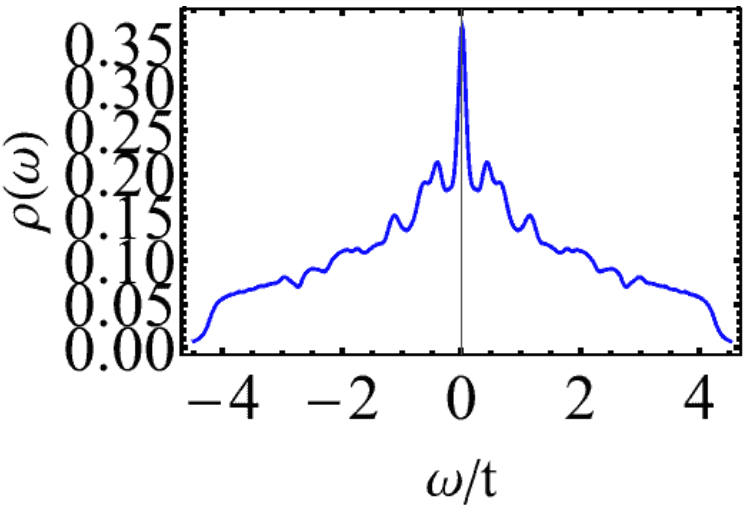

Figure 4.6: The DOS of Penrose QC with 3571 lattice points.

are of the same length. $\langle i, j\rangle$ denotes sum over all lattice sites i and nearest-neighbor sites j for each i. To explore the electronic properties of a Penrose QC, the DOS of the tight-binding model on a QC with N vertices [94],

$$\rho(\omega) = \frac{1}{N}\sum_{\nu}\delta(\omega - \epsilon_\nu), \tag{4.11}$$

for a 3571-site Penrose approximant is shown in Fig. 4.6. By diagonalizing Eq. (4.10), a set of eigenenergies $\{\epsilon_\nu\}$ is obtained and the delta function $\delta(\omega - \epsilon_\nu)$ in the DOS is numerically calculated as the Lorentzian with smoothing width of $0.1/t$ to plot the DOS.

The pronounced peak at $\omega/t = 0$ corresponds to strictly localized zero-energy states [95]. There are six types of such strictly localized states [96, 97, 98], as illustrated in Fig. 4.7. Each number on the lattice sites represent the probability amplitude at each site, where the positive and negative phases of the wave function are distinguished by red and blue, respectively. In a system of N lattice sites, a strictly localized state $|\mathrm{loc}\rangle$ is a complex vector of length N whose ith element is the value written on the ith lattice site in Fig. 4.7 devided by a normalization constant. Also, $\mathcal{H}_0$ in Eq.(4.10) is a $N \times N$ matrix, and $\mathcal{H}_0 |\mathrm{loc}\rangle$ is a complex vector of length N. The ith element of $\mathcal{H}_0 |\mathrm{loc}\rangle$ is $-t$ times the sum of jth elements of $|\mathrm{loc}\rangle$ over nearest-neighbor sites j for i. However, for any given site i where the probability amplitude of $|\mathrm{loc}\rangle$ is nonzero, the probability amplitude is zero at all of its nearest-neighbor

sites $\{j\}$. Therefore, for any strictly localized state $|\mathrm{loc}\rangle$,

$$\mathcal{H}_0 \, |\mathrm{loc}\rangle = 0 \, |\mathrm{loc}\rangle \, . \tag{4.12}$$

This means that all localized states in Fig. 4.7 are zero-energy states.

4.4.2 Perpendicular Space of Penrose Quasicrystal and Approximant

In this subsection, the perpendicular-space representation is introduced by taking Penrose QC and approximant as an example. Perpendicular space refers to the remainder of the hyperspace after the periodic lattice structure (' hypercubic lattice ') is projected onto lower dimensions to form a QC. The properties of the QC can be studied in terms of projection of the hypercubic lattice onto the perpendicular space, called the perpendicular-space representation.

The physical-space representation of Penrose QC can be obtained by projection of a five-dimensional hypercubic lattice onto the two-dimensional physical space. The same Penrose QC can be represented by projecting the five-dimensional hypercubic lattice onto the three-dimensional perpendicular space. The perpendicular-space representation of Penrose QC consists of four two-dimensional planes in the three-dimensional perpendicular space. There are no lattice points other than on these four planes. Accordingly, the perpendicular-space representation of Penrose QC can be illustrated in four two-dimensional spaces. An example of the perpendicular-space representation of Penrose QC is shown in Fig. 4.8. By definition, there is one-to-one correspondence between a point in the physical space and a point in the perpendicular space. That is, a point in the hyperspace generates a set of two points, one in the physical space and another in the perpendicular space, and the total number of points is the same in the physical space and the perpendicular space.

There are mainly two advantages of using the perpendicular-space representation. Firstly, the effect of local or global environment is well visualized in the perpendicular-space representation. A distance in the perpendicular space is associated with the local environment. Here, the environment means the lattice points' distribution around a certain lattice point. The local environment with the minimum length scale is represented by given the coordination

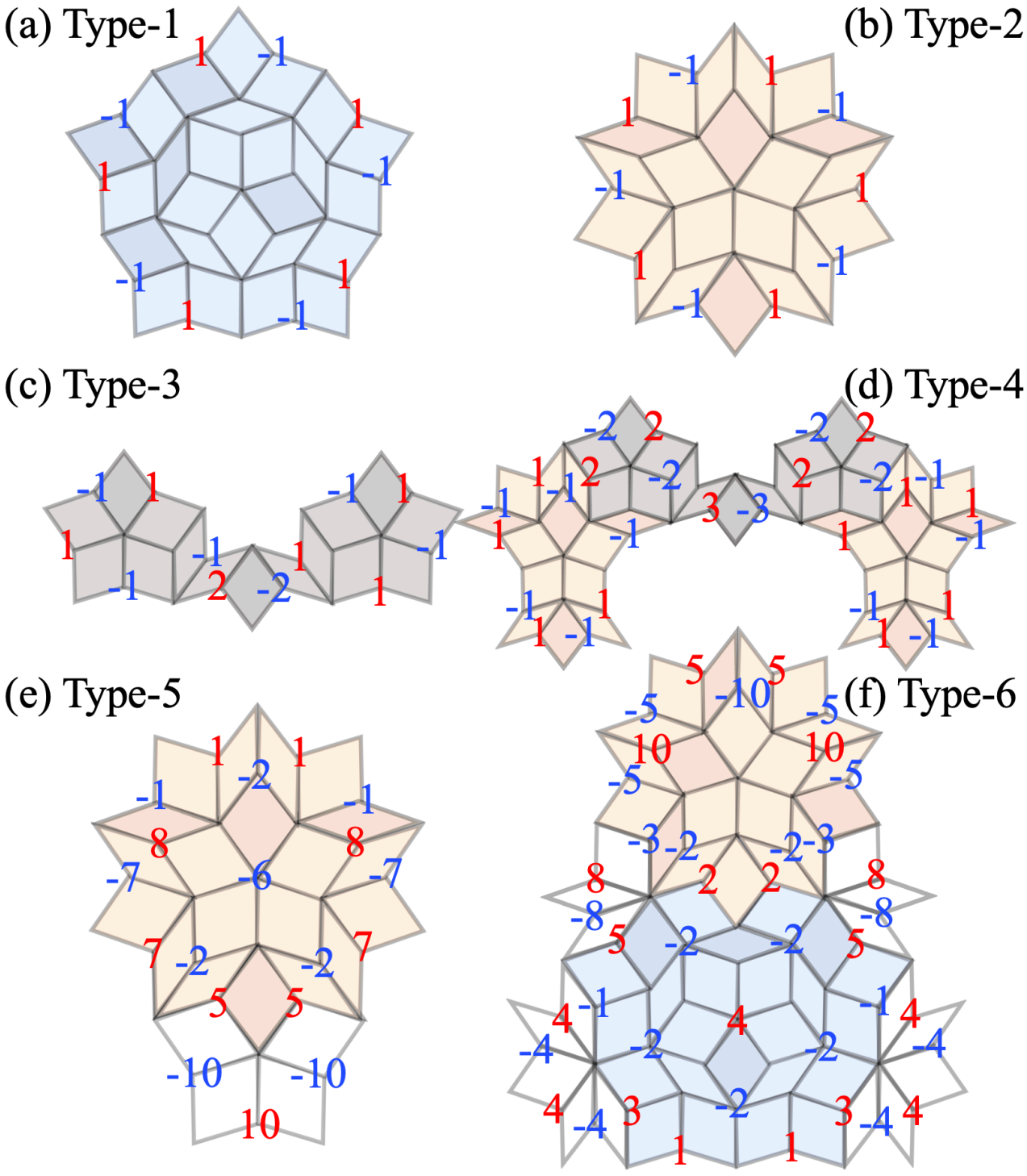

Figure 4.7: Six types of strictly localized zero-energy states in a Penrose QC [96, 97, 98].

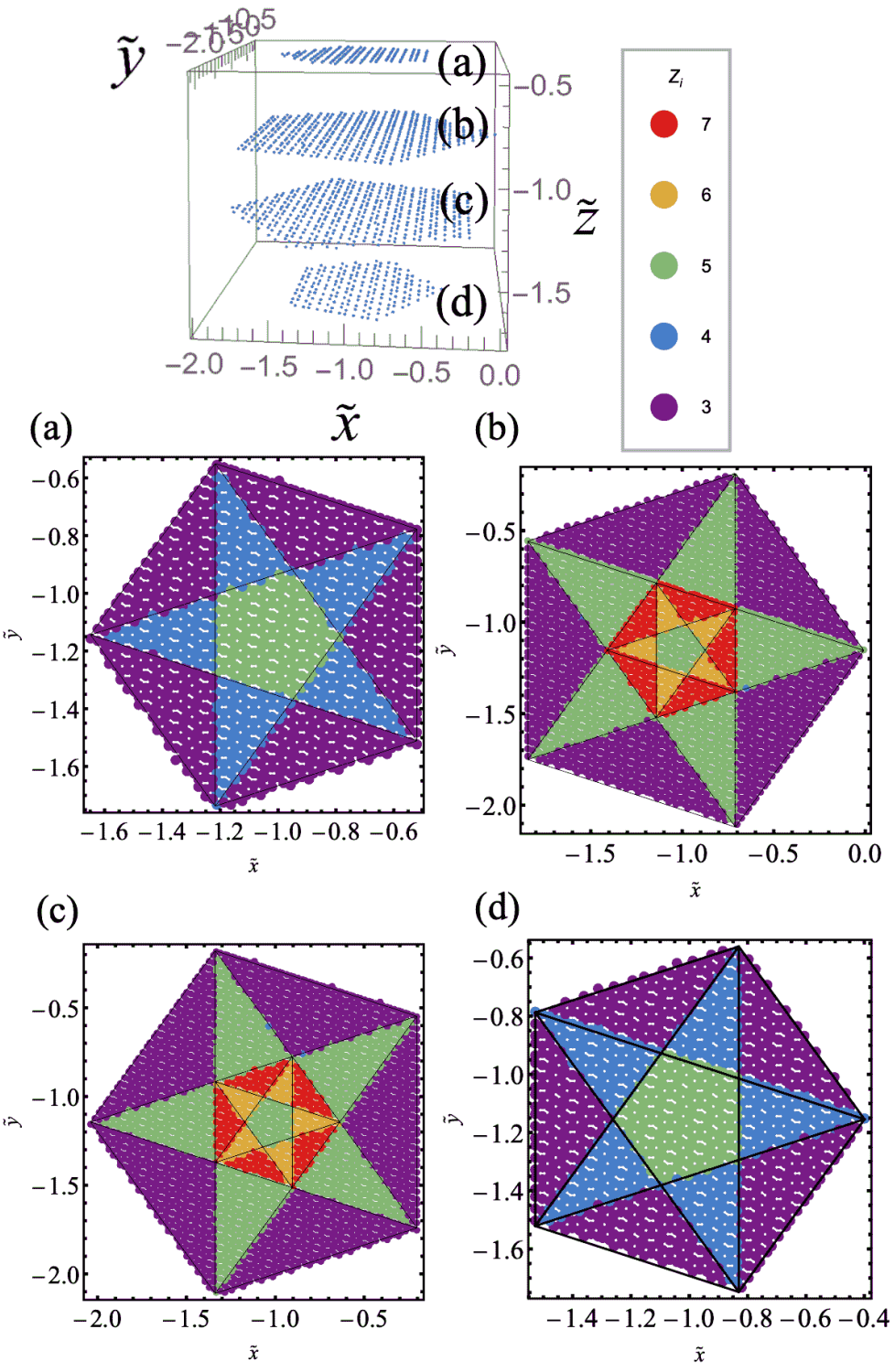

Figure 4.8: Perpendicular-space representation of Penrose QC. The three-dimensional perpendicular space consists of four planes (a)-(d). The $\tilde{z}$ element of each subspace is (a) -0.447214, (b) -0.894427, (c) -1.34164, and (d) -1.78885.

number. In the perpendicular space of Penrose QC in Fig. 4.8, coordination numbers are represented by colors and points with the same coordination number gather and form sectors in each of the four planes. As the coordination number determines the local environment of each lattice site, this means that points with the same local environment are gathered in the perpendicular-space representation in Fig. 4.8. Thus, effects of the local environment of all vertices in Penrose QC in the physical space can be studied in the perpendicular space. If the distribution of a certain physical quantity is not uniform in each sector in the perpendicular space, it follows that the distribution of the physical quantity is not governed by the local environment such as the number of nearest-neighbor sites, but may be affected by more distant sites.

Secondly, self-similarity can be well visualized in the perpendicular space. The procedure associated with self-similarity of Penrose QC is illustrated in Fig. 4.9. Figures 4.9 (a-d) are the perpendicular-space representation of Penrose QC shown in Fig. 4.8 with added thick black lines outlining a pentagonal sector at the center in each plane. The lattice points located inside (outside) these pentagonal sectors are shown in Fig. 4.9 (e) by red (gray) in the physical space. By connecting the red points in Fig. 4.9 (e), another Penrose QC with a larger lattice constant and fewer vertices can be generated.

A histogram of coordination numbers of the larger Penrose QC in Fig. 4.9 (e) is shown in Fig. 4.10. Coordination numbers in this Penrose QC also range from 3 to 7 and the average coordination number is almost four. The most frequently appearing coordination number is three, while there are much fewer lattice sites with highest coordination numbers such as six and seven. These coordination numbers are represented by colors in the physical space in Fig. 4.11. The distribution of coordination numbers has fivefold rotational symmetry whose rotational center is represented as a black dot at $(x, y) = (53.1418, -36.9852)$. This shows that the red points in Fig. 4.9 (e) indeed form another Penrose QC. These coordination numbers represented by colors are also shown in the perpendicular space in Fig. 4.12. Within each of the pentagons outlined with the thick black lines in Figs. 4.9 (a, d) and within the smaller pentagon inside the thick-lined pentagon in Figs. 4.9 (b, c), now we see sectors formed by different coordination numbers. Note that Figs. 4.12 (a), (b), (c), and (d) (inside the pentagons which were outlined with the thick lines in Figs. 4.9(a-d)) have the same

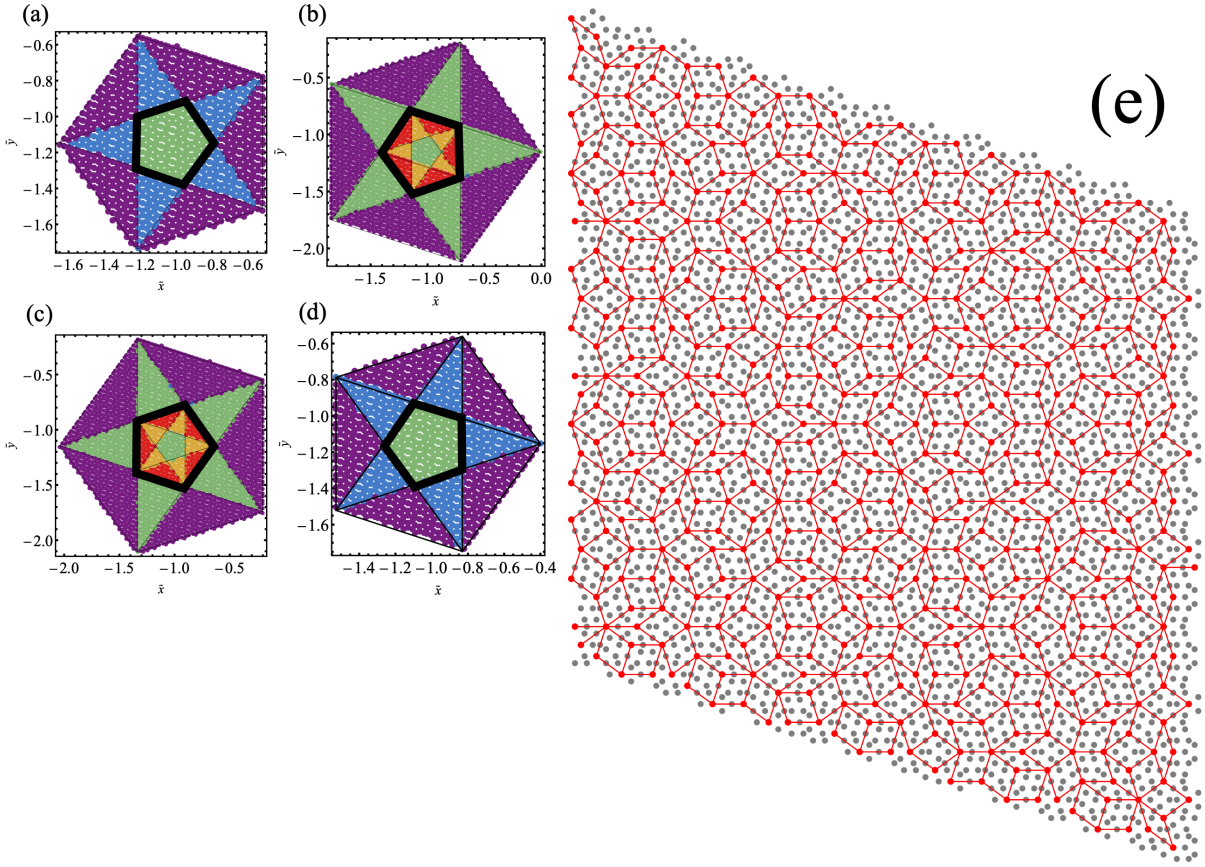

Figure 4.9: (a-d) Perpendicular-space representation of Penrose QC shown in Fig. 4.8 with the outline (thick black lines) of a pentagonal sector at the center in each plane. (e) The lattice points located inside (outside) each of the pentagonal sectors in the perpendicular space are colored by red (gray) in the physical space. The red vertices form a larger Penrose QC.

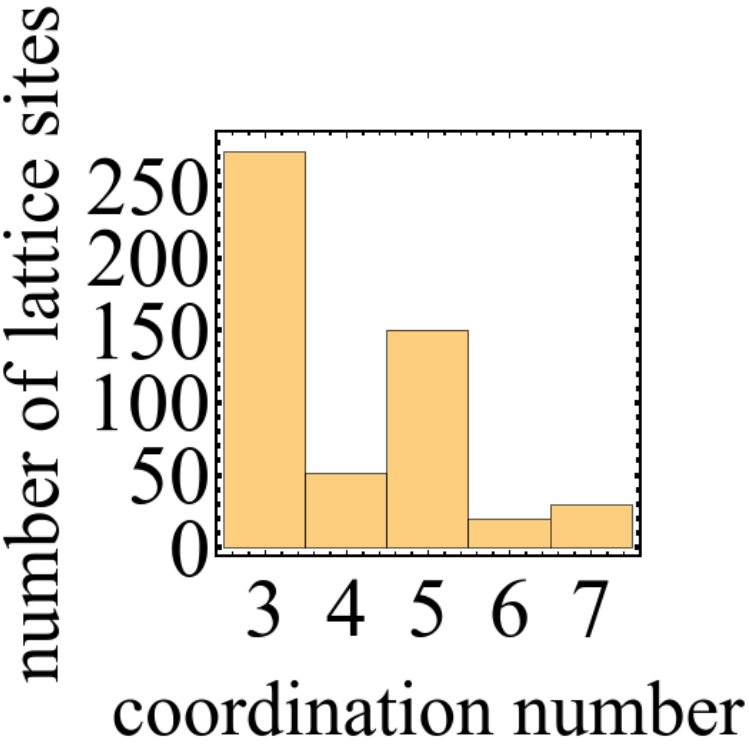

Figure 4.10: Histogram of coordination numbers of the larger Penrose QC connecting the red vertices in Fig. 4.9 (e).

structure as Figs. 4.9 (d), (c), (b), and (a), respectively.

This procedure can be repeated as illustrated in Fig. 4.13. Figures 4.13 (a-d) show the perpendicular-space representation shown in Figs. 4.12 (a-d) with added thick black lines outlining a pentagonal sector at the center in each plane. The lattice points located inside these pentagonal sectors are shown in Fig. 4.13 (e) as blue vertices in the physical space, in addition to the gray and red lattice points in Fig. 4.9 (e). By connecting the blue points in Fig. 4.13 (e), another Penrose QC with a larger lattice constant can be generated.

This procedure which generates another, larger Penrose QC by extracting some lattice points in Penrose QC can be repeatedly performed to Penrose QC with enough number of lattice points, and this property is called self-similarity. Although it is difficult to find a set of lattice points which form another Penrose QC in the physical space, such lattice points gather inside a center pentagon in each subspace of the perpendicular space, as illustrated in Figs. 4.9 (a-d) and Figs.4.13 (a-d). It follows that, for example, if the distribution of the magnitude of a superconducting order parameter which is rescaled so that the minimum value

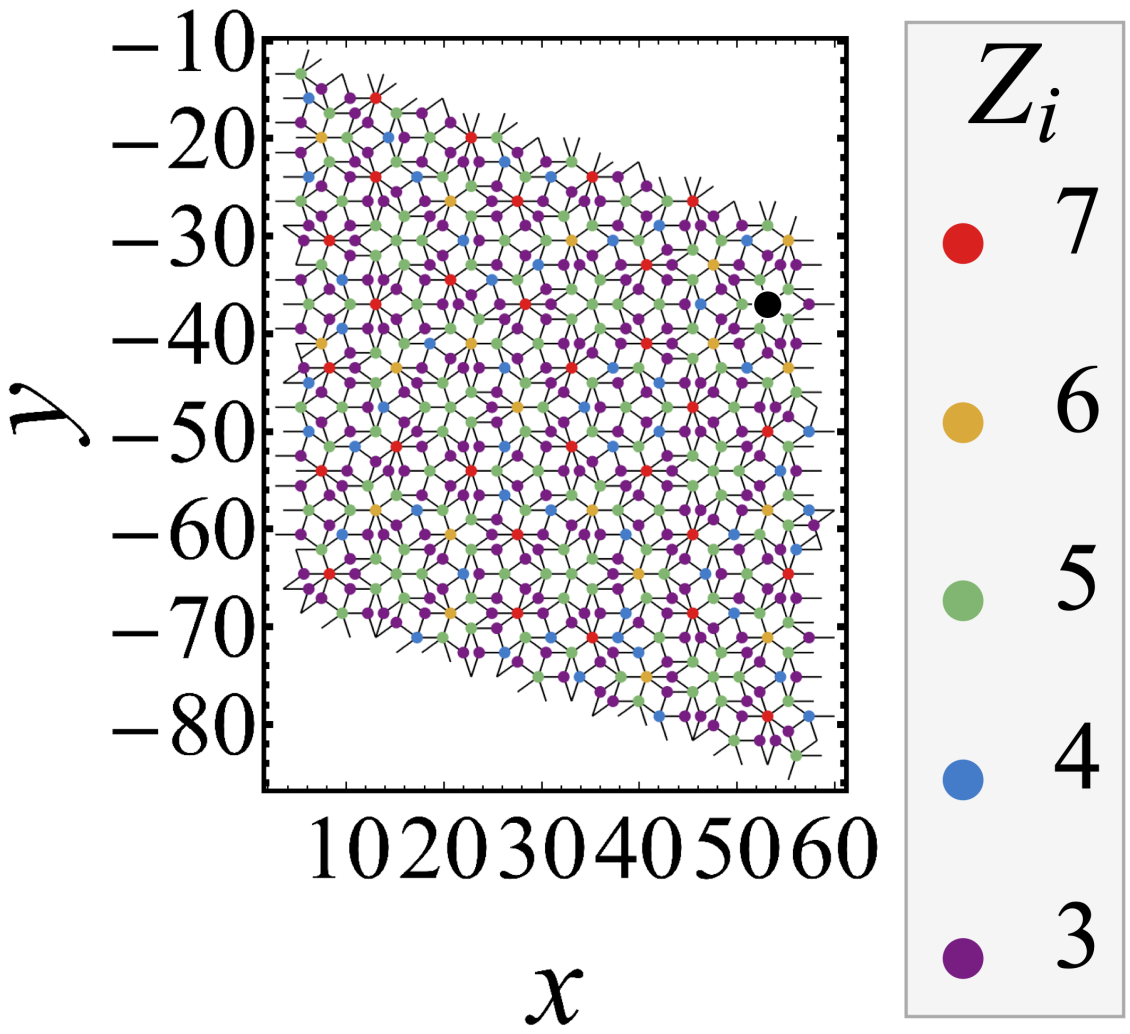

Figure 4.11: Coordination numbers of the larger Penrose QC that consists of the red vertices in Fig. 4.9 (e) in the physical space.

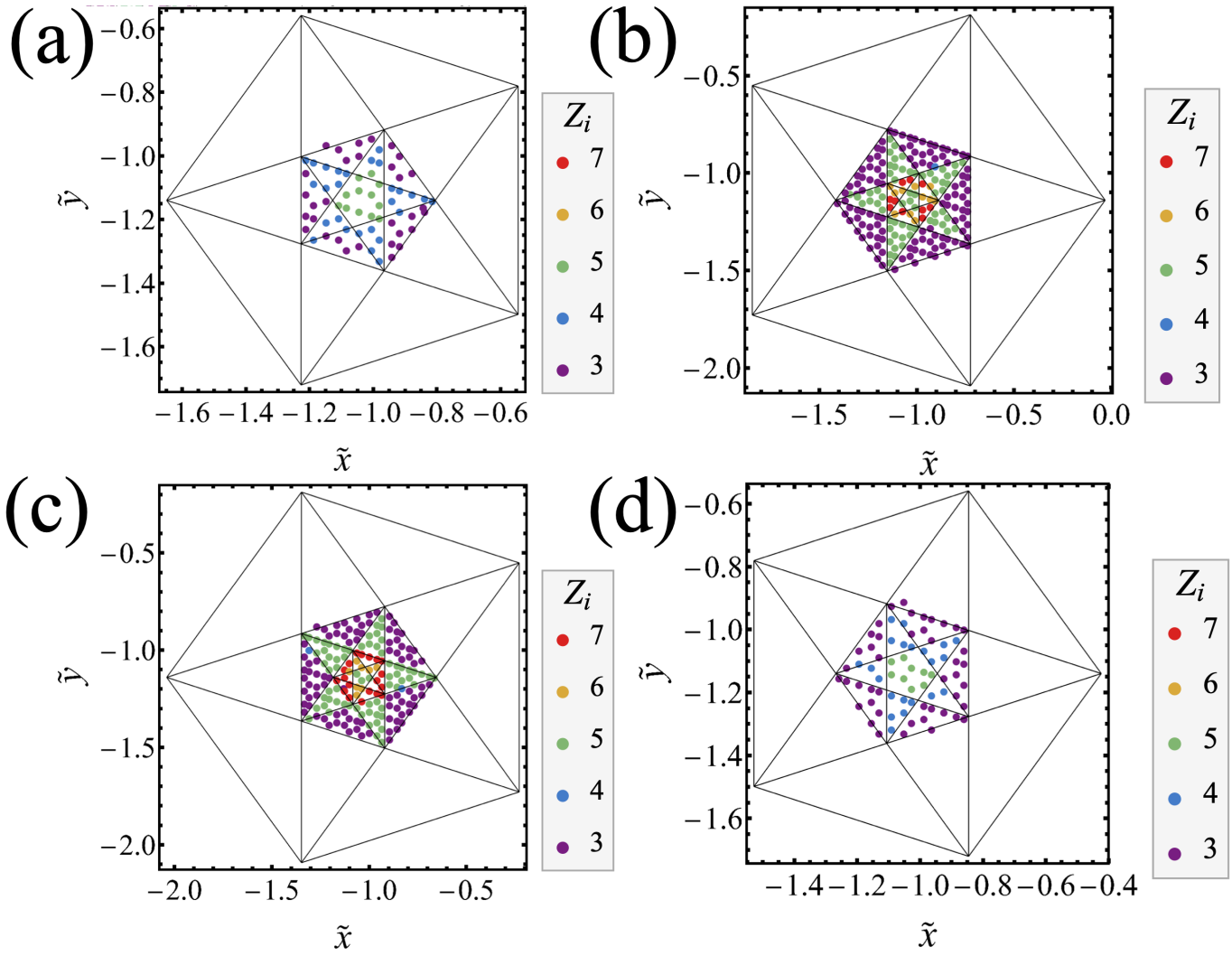

Figure 4.12: Coordination numbers of Penrose QC formed by the red vertices in Fig. 4.9 (e) in the perpendicular space. The $\tilde{z}$ element of each plane is (a) -0.447214, (b) -0.894427, (c) -1.34164, and (d) -1.78885.

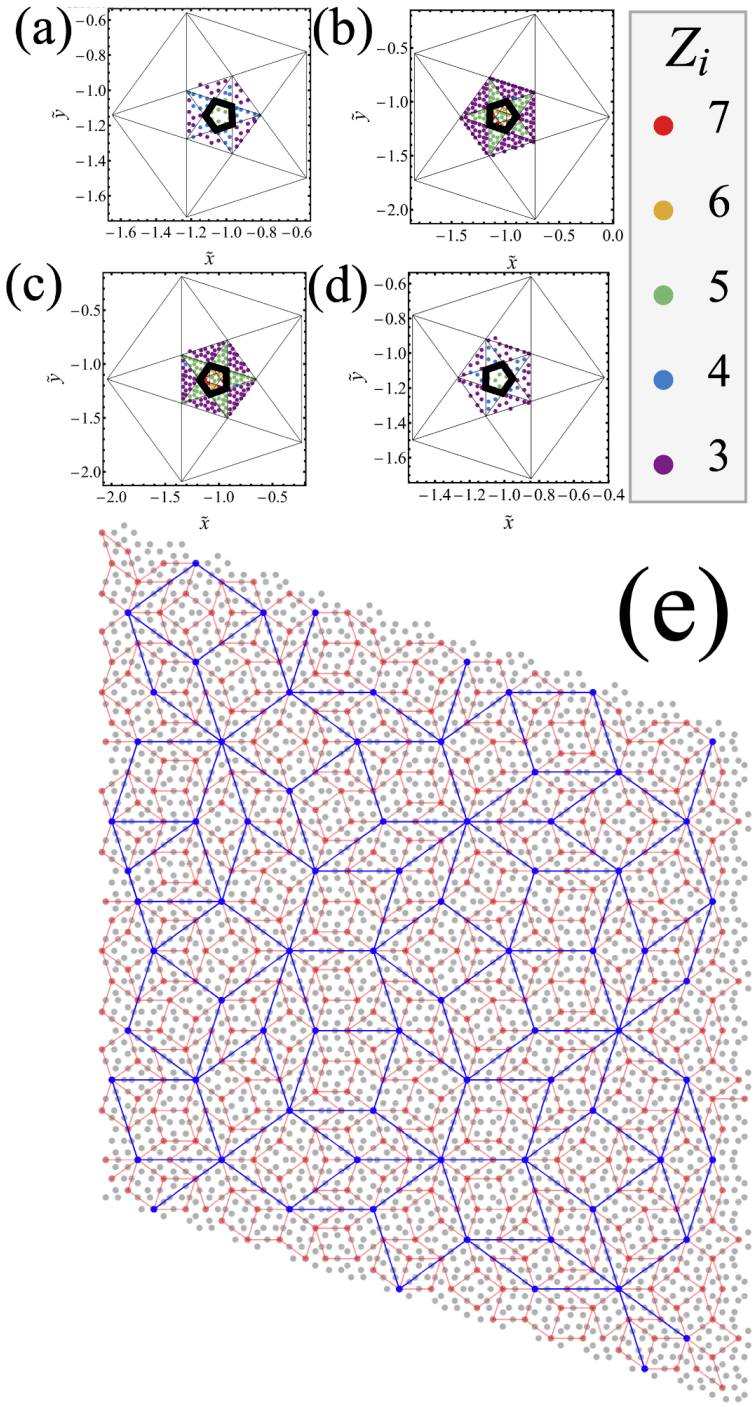

Figure 4.13: (a-d) Perpendicular-space representation of Penrose QC shown in Fig. 4.12 with added thick black lines outlining a pentagonal sector at the centre in each plane. (e) The lattice points located inside each of the pentagonal sectors in the perpendicular space are colored by blue in the physical space.

is zero and the maximum value is one in the entire perpendicular space is the same as that of the distribution of the magnitude of the superconducting order parameter rescaled inside the thick-lined pentagons in Figs. 4.9 (a-d), then the distribution of the superconducting order parameter also shows the self-similarity that Penrose QC has.

4.5 Ammann-Beenker Quasicrystal and Approximant

In this section, another famous example of two-dimensional QCs, AB QC is introduced.

4.5.1 Basics of Ammann-Beenker Quasicrystal and Approximant

An example of AB QC is shown in Fig. 4.14. Similarly to Penrose tiling, AB tiling can be constructed with two tiles. AB tiling can be composed of a rhombus with angles of 45 degrees and 135 degrees, and a square with the same side length as that of the rhombus. The area ratio of the rhombus and the square is $1 + \sqrt{2}$, and this ratio is the well-known silver ratio. The silver ratio is one of the roots of the quadratic equation $x^2 - 2x - 1 = 0$. A histogram of coordination numbers of AB QC shown in Fig. 4.14 is presented in Fig. 4.15. Coordination numbers in AB QC range from 3 to 8. The most frequently appearing coordination number is three, while there are much fewer vertices with highest coordination numbers such as seven and eight. The average coordination number in AB QC is exactly four, which is the same as that of Penrose QC.

An AB QC consists of the vertices of AB tiling as the lattice sites, and we use the tight-binding vertex model. As in a Penrose QC, the side lengths of rhombus and square are all the same, so all links connecting lattice sites are of the same length. Following the algebraic approach of de Brujin's work for Penrose tiling, Beenker proposed the cut and project method for producing AB QCs in 1982 [99]. However, Ammann is the one who first invented AB tiling [100], and the lattice is named after the two researchers Ammann and Beenker. We generate AB approximants using inflation mapping [101, 68].

To explore the electronic properties of an AB QC, the DOS in Eq. (4.11) of the tight-binding model on a 8119-site AB QC is shown in Fig. 4.16 [66]. The DOS is calculated with the tight-binding vertex model Hamiltonian in Eq. (4.10), where the sum is over lattice sites

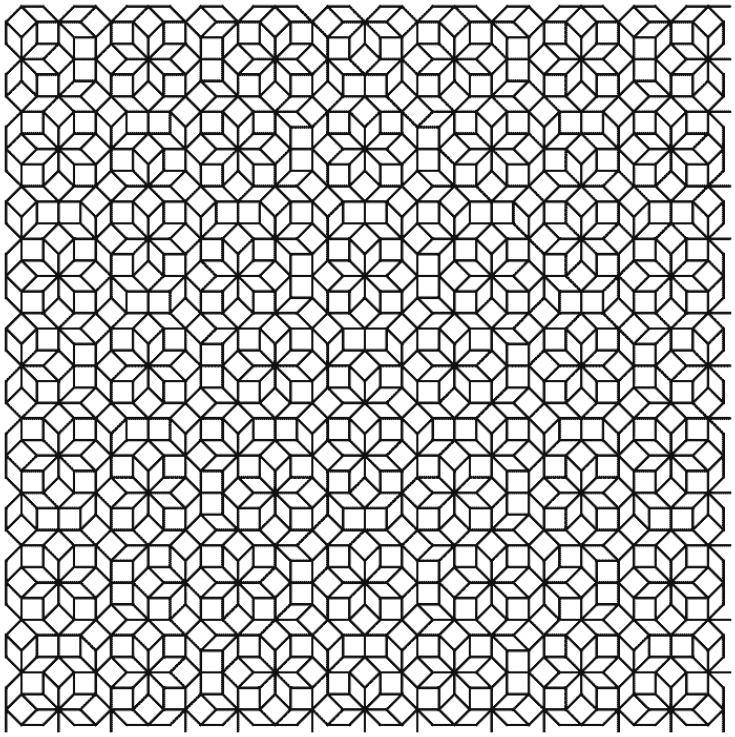

Figure 4.14: AB QC with 1393 lattice points.

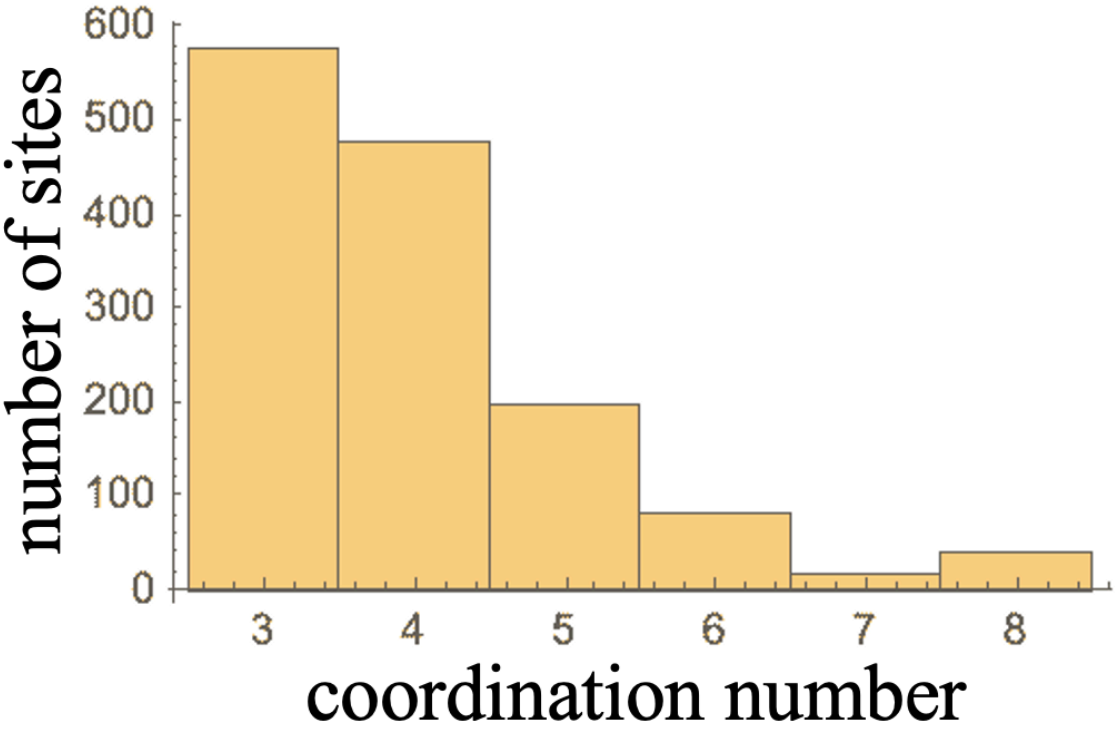

Figure 4.15: Histogram of coordination numbers in AB QC shown in Fig. 4.14.

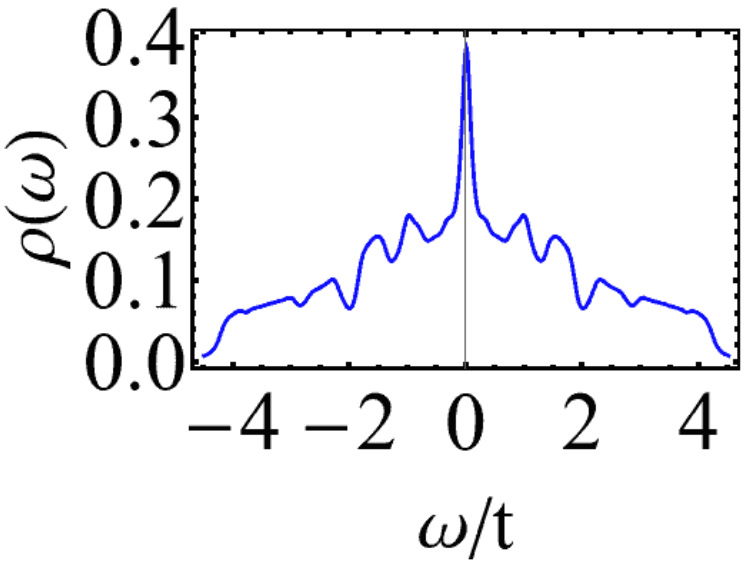

Figure 4.16: The DOS of AB QC with 8119 lattice points.

$\{i\}$ and nearest-neighbor sites for each i along links shown in Fig. 4.14. The filling factor $n(\mu)$ is defined as $n(\mu) = \int_{-\infty}^{\mu} \mathrm{d}\omega\rho(\omega)$. As in Penrose QC case, there is a large peak at $\omega = 0$ in Fig. 4.16. This is a key character related with the local topology of the octagonal tiling. There is a pseudogap at $\omega \approx -1.9t$, corresponding to the filling $\frac{2}{s^2}$, where s is the silver ratio $s = 1 + \sqrt{2}$. The corresponding filling factor is plotted as a function of the chemical potential μ in Fig. 4.17. The black line indicates half filling $n(\mu) = 1.000$, while the red line indicates $n(\mu) = \frac{2}{s^2}$. Reflecting the peak at $\omega = 0$ in the DOS, the filling factor jumps at $\mu = 0$. Also, reflecting the pseudogap at $\omega \approx -1.9t$ in the DOS, the filling factor jumps at the corresponding μ.

4.5.2 Perpendicular Space of Ammann-Beenker Quasicrystal and Approximant

In this subsection, the perpendicular space of AB QC and approximant is introduced. Similarly to the case of Penrose QC, the physical-space representation of AB QC can be obtained by projection of a four-dimensional hypercubic lattice onto the two-dimensional physical space, and the corresponding perpendicular space is two-dimensional. The perpendicular-space representation of AB QC is illustrated in Fig. 4.18, whose coordination numbers are

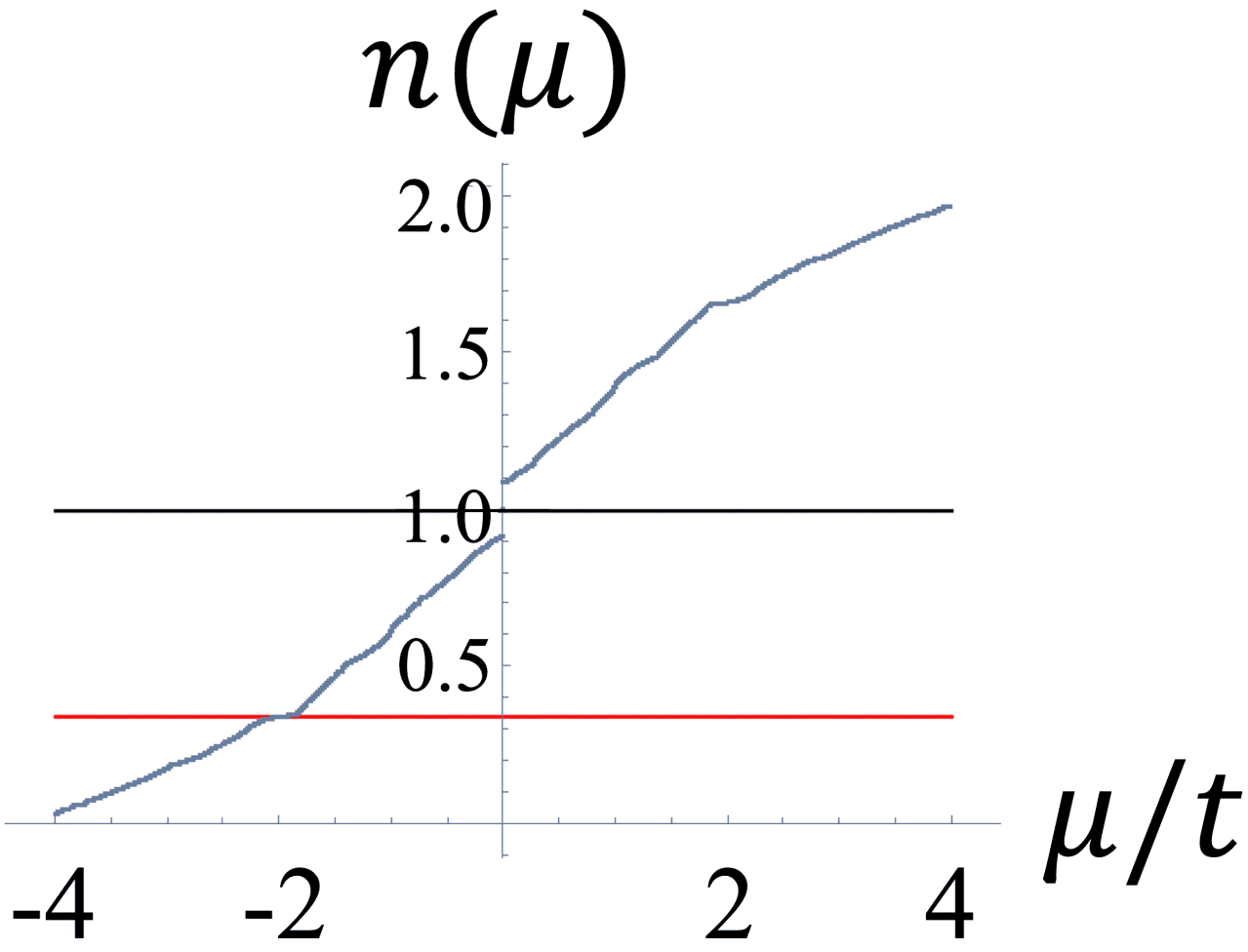

Figure 4.17: The filling factor of AB QC with 8119 sites as a function of the chemical potential μ.

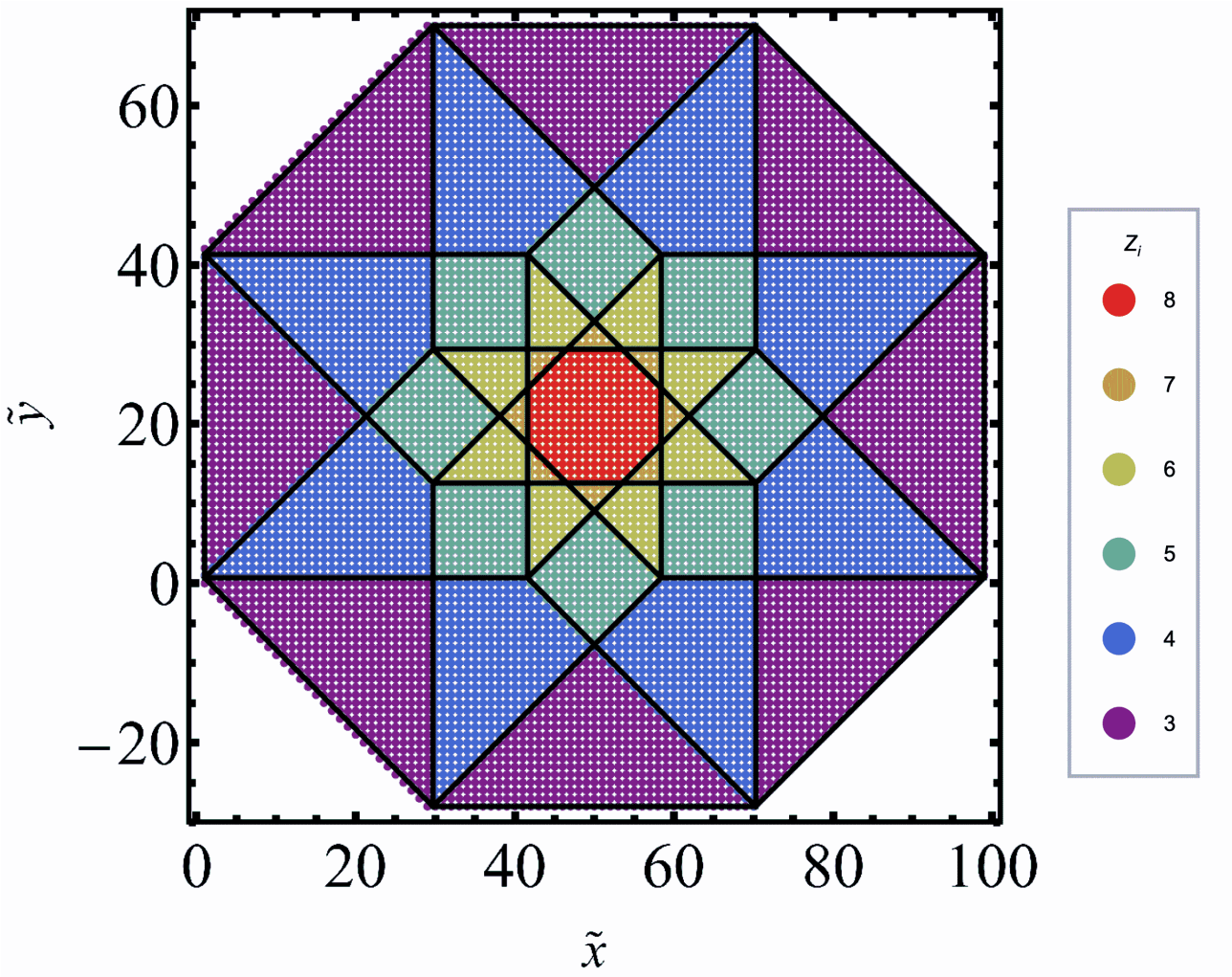

Figure 4.18: The perpendicular-space representation of an AB QC, where lattice points with different coordination numbers form different sectors.

represented by colors. Similarly to Penrose QC, points with the same coordination number form sectors in the perpendicular space and thus, the perpendicular-space representation is useful also in AB QC.

Self-similarity of AB QC is illustrated in Fig. 4.19. Figure 4.19 (a) is the perpendicular-space representation of AB QC shown in Fig. 4.18 with added thick black lines outlining the octagonal sector at the center. The lattice points located inside (outside) the octagonal sector are shown in Fig. 4.19 (b) by red (gray) in the physical-space representation. By connecting the red points in Fig. 4.19 (b), another AB QC with a larger lattice constant can be generated. Although it is difficult to find the set of lattice points which generates this larger AB QC in the physical space, those lattice points can be seen clearly in the perpendicular space as

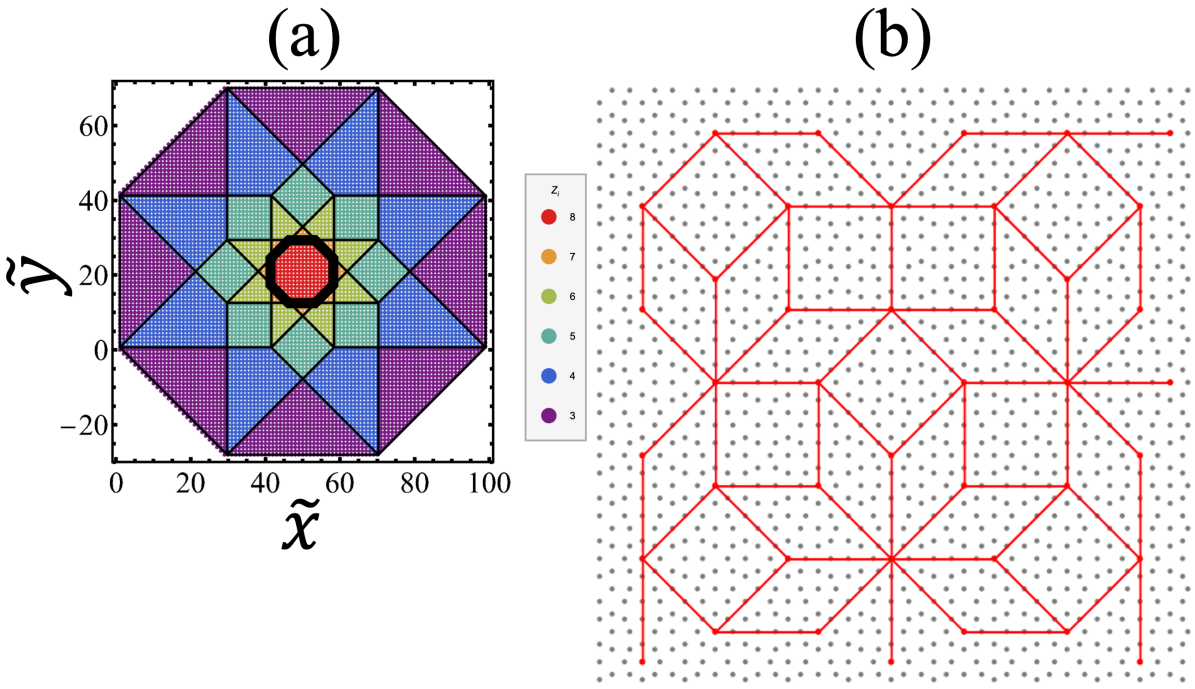

Figure 4.19: (a) The perpendicular-space representation of AB QC shown in Fig. 4.18 with added thick black lines outlining the octagonal sector at the center. (b) The lattice points located inside (outside) the octagonal sector are colored by red (gray) in the physical space.

they gather inside the thick-lined octagon in Fig. 4.19 (a). It follows that, for example, if the distribution of the magnitude of a superconducting order parameter which is rescaled so that the minimum value is zero and the maximum value is one in the entire perpendicular space is the same as that of the distribution of the magnitude of the superconducting order parameter rescaled inside the thick-lined octagon in Figs. 4.19 (a), then the distribution of the superconducting order parameter also shows the same self-similarity as that of AB QC.

4.6 Conventional s-wave Superconductivity in Ammann-Beenker QC

Experimentally, SC was found in QC approximants before that of QCs. In 1987, SC in icosahedral approximants was examined with $Mg_3Zn_3Al_2$ [63]. Also, in 2015, Au-Ge-Yb approximants with Tsai-type clusters were found to show SC [102]. Following this observation of SC in approximants, SC in a QC was confirmed with Al-Zn-Mg QC in 2018 [49]. The

BCS theory can explain the observed thermodynamic properties of SC in Al-Zn-Mg QC, indicating that it is weak-coupling s-wave SC. Among the few theoretical studies of SC in QCs [64, 65, 66], the BdG equations were solved self-consistently for conventional s-wave SC in AB QCs in Ref. [66], with results compatible with the experimental findings of Ref. [49]. In this section, a preliminary study of conventional s-wave SC in AB QCs, reproducing some results of Ref. [66], is briefly summarized.

Fixing the electronic filling $n = \frac{1}{N}\sum_i \left(\left\langle c_{i\uparrow}^\dagger c_{i\uparrow}\right\rangle + \left\langle c_{i\downarrow}^\dagger c_{i\downarrow}\right\rangle\right)$, the mean-field attractive Hubbard Hamiltonian in Eq. (2.24) on a finite AB QC has been solved self-consistently to obtain the mean fields $V_{ii}^{(\mathrm{H})}$ and $\Delta_{ii}^{\downarrow\uparrow}$. Here, the chemical potential μ is adjusted so that the desired filling factor n is realized. For $n = 0.25$ and $U = 1.5t$ at zero temperature, the mean value and standard deviation of the magnitude of the self-consistently obtained superconducting order parameter whose coordination number is z, $|\Delta_z/t|$, are plotted in Fig. 4.20. The average value of $|\Delta_z/t|$ depends on the coordination number, and the larger the coordination number, the larger the mean value, except for $z = 8$. The standard deviation for each coordination number is small, and thus the magnitude of the superconducting order parameter is mainly determined by local environment. The average and standard deviation of $|\Delta_z/t|$ for half filling, $n = 1.00$, are plotted in Fig. 4.21. In this case, the larger the coordination number, the smaller the average $|\Delta_z/t|$.

In Ref. [66], the temperature dependence of the superconducting order parameter was calculated and compared with the prediction of the BCS theory. The temperature dependence of the superconducting order parameter for $n = 0.25$ is consistent with the BCS theory; however, the results for $n = 1.00$ are different from what the BCS theory predicts. This implies that superconductivity in AB QC at half filling is fundamentally different from conventional SC in periodic systems, possibly due to the presence of localized states.

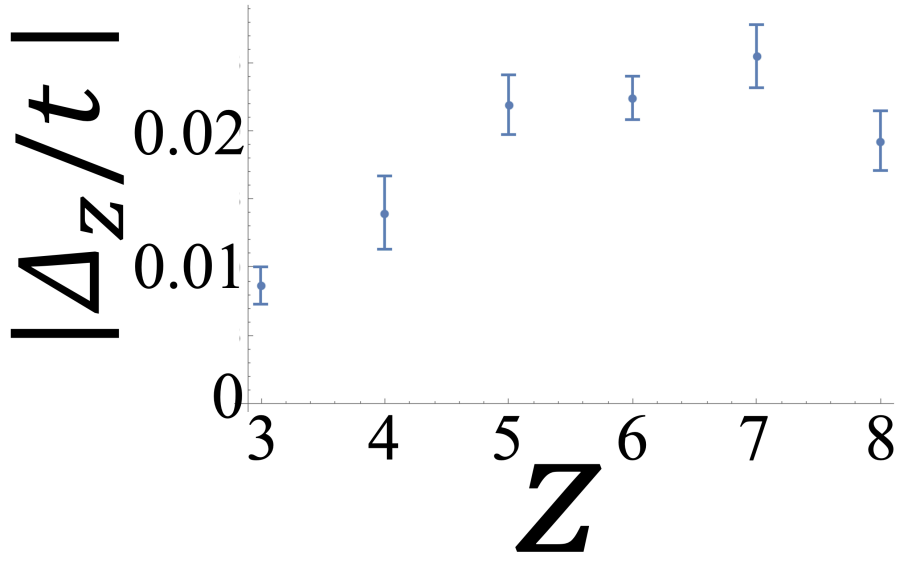

Figure 4.20: The mean and standard deviation of the magnitude of the self-consistently obtained superconducting order parameter in units of the hopping amplitude t whose coordination number is z for $n = 0.25$.

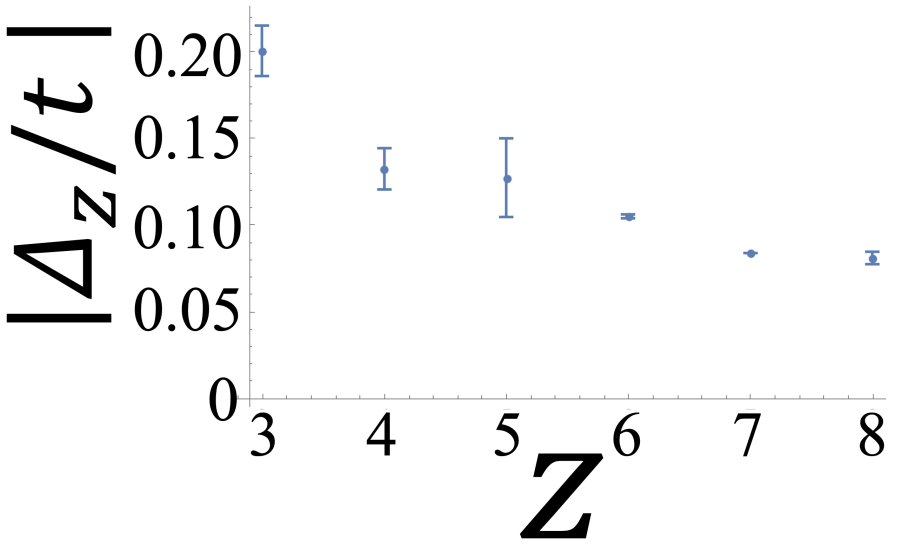

Figure 4.21: The mean and standard deviation of the magnitude of the self-consistently obtained superconducting order parameter in units of the hopping amplitude t whose coordination number is z at half filling, for $n = 1.00$.

5 Topological Superconductivity in Penrose and Ammann-Beenker Quasicrystals

In this chapter, the model Hamiltonian for TSC in two-dimensional systems is introduced and solved numerically. Due to the inhomogeneity of quasicrystals, momentum-space analysis is not applicable, and the BdG equations are solved self-consistently for the mean fields. Two parameter sets are selected for the calculation, corresponding to the nontrivial topological phase and trivial phase.

5.1 Topological Superconductivity Model for Periodic Systems

In this section, the tight-binding model for s-wave TSC with broken time-reversal symmetry in a two-dimensional system is introduced. The model is described for a square lattice as proposed originally [72], which has translational symmetry and enables analytical formulation. The model can be generalized to aperiodic systems such as Penrose and AB QCs, as shown in the next section.

5.1.1 Model Hamiltonian and Topological Phase Boundaries for Square Lattice

The model Hamiltonian for TSC in a square lattice with the lattice constant set to unity can be expressed in momentum space as

$$\mathcal{H} = \sum_{\boldsymbol{k},\sigma} \epsilon(\boldsymbol{k}) c^\dagger_{\boldsymbol{k}\sigma} c_{\boldsymbol{k}\sigma} - \mu_{\mathrm{B}} H_z \sum_{\boldsymbol{k},\sigma,\sigma'} (\sigma_z)_{\sigma,\sigma'} c^\dagger_{\boldsymbol{k}\sigma} c_{\boldsymbol{k}\sigma'} + \alpha \sum_{\boldsymbol{k},\sigma,\sigma'} \mathcal{L}_0(\boldsymbol{k}) \cdot \boldsymbol{\sigma}_{\sigma\sigma'} c^\dagger_{\boldsymbol{k}\sigma} c_{\boldsymbol{k}\sigma'} + \frac{1}{2} \sum_{\boldsymbol{k},\sigma,\sigma'} \Delta_{\sigma\sigma'}(\boldsymbol{k}) c^\dagger_{\boldsymbol{k}\sigma} c^\dagger_{-\boldsymbol{k}\sigma'} + \frac{1}{2} \sum_{\boldsymbol{k},\sigma,\sigma'} \Delta^*_{\sigma'\sigma}(\boldsymbol{k}) c_{-\boldsymbol{k}\sigma} c_{\boldsymbol{k}\sigma'}, \tag{5.1}$$

where $c^\dagger_{\boldsymbol{k}\sigma}$ ($c_{\boldsymbol{k}\sigma}$) is a creation (an annihilation) operator for an electron with momentum $\boldsymbol{k} = (k_x, k_y)$ and spin σ. The Pauli matrices are expressed as σ_i for $i = x, y, z$, whose components are written as $(\sigma_i)_{\sigma\sigma'}$. For example, $\sigma_z = \begin{pmatrix} 1 & 0 \\ 0 & -1 \end{pmatrix}$ is the z component of the Pauli matrices, and $(\sigma_z)_{\uparrow\uparrow} = 1$, $(\sigma_z)_{\downarrow\downarrow} = -1$, $(\sigma_z)_{\uparrow\downarrow} = (\sigma_z)_{\downarrow\uparrow} = 0$. The first term in the model Hamiltonian is a kinetic term with the energy-band dispersion $\epsilon(\boldsymbol{k}) = -2t(\cos(k_x) + \cos(k_y)) - \mu$, where t is the uniform hopping amplitude between nearest-neighbor sites and μ is the chemical potential. The second term is the Zeeman coupling which separates up spin and down spin, with the strength $\mu_B H_z$. The Rashba spin-orbit coupling is introduced in the third term with $\alpha\mathcal{L}_0(\boldsymbol{k}) = \alpha(\sin(k_y), -\sin(k_x))$, where $\alpha > 0$ is the coupling strength. The fourth term and its Hermitian conjugate, the fifth term, are for spin-singlet SC, where the order parameter components are

$$\Delta_{\sigma\sigma'}(\boldsymbol{k}) = \imath\Delta(\boldsymbol{k})(\sigma_y)_{\sigma\sigma'}. \tag{5.2}$$

Especially, for isotropic s-wave pairing, $\Delta(\boldsymbol{k}) = \Delta_s$ (constant). The Hamiltonian in coordinate space can be obtained by Fourier transform,

$$c^\dagger_{\mathbf{i}\sigma} = \frac{1}{\sqrt{N}} \sum_{\boldsymbol{k}} e^{\imath \boldsymbol{k}\cdot\mathbf{i}} c^\dagger_{\boldsymbol{k}\sigma}, \tag{5.3}$$

for a square lattice of N sites. The lattice version of Eq. (5.1) is then given by

$$\mathcal{H} = \mathcal{H}_{\mathrm{kin}} + \mathcal{H}_{\mathrm{SO}} + \mathcal{H}_s, \tag{5.4}$$

$$\mathcal{H}_{\text{kin}} = -t \sum_{\langle \mathbf{i},\mathbf{j}\rangle,\sigma} c^{\dagger}_{\mathbf{i}\sigma} c_{\mathbf{j}\sigma} - \mu \sum_{\mathbf{i},\sigma} c^{\dagger}_{\mathbf{i}\sigma} c_{\mathbf{i}\sigma} - \mu_{\text{B}} H_z \sum_{\mathbf{i},\sigma,\sigma'} (\sigma_z)_{\sigma\sigma'} c^{\dagger}_{\mathbf{i}\sigma} c_{\mathbf{i}\sigma'}, \tag{5.5}$$

$$\mathcal{H}_{\text{SO}} = -\lambda \sum_{\mathbf{i}} \left[\left(c^{\dagger}_{\mathbf{i}-\hat{x}\downarrow} c_{\mathbf{i}\uparrow} - c^{\dagger}_{\mathbf{i}+\hat{x}\downarrow} c_{\mathbf{i}\uparrow} \right) + \imath \left(c^{\dagger}_{\mathbf{i}-\hat{y}\downarrow} c_{\mathbf{i}\uparrow} - c^{\dagger}_{\mathbf{i}+\hat{y}\downarrow} c_{\mathbf{i}\uparrow} \right) + \text{H.c.} \right], \tag{5.6}$$

$$\mathcal{H}_{\text{s}} = \Delta_s \left(c^{\dagger}_{\mathbf{i}\uparrow} c^{\dagger}_{\mathbf{i}\downarrow} + \text{H.c.} \right), \tag{5.7}$$

where $\mathbf{i} = (i_x, i_y)$ is a set of x and y coordinates of a site on the square lattice, $\lambda = \dfrac{\alpha}{2}$, and $c^{\dagger}_{\mathbf{i}\sigma}$ and $c_{\mathbf{i}\sigma}$ are creation and annihilation operators for an electron at site $\mathbf{i}$ with spin σ. The notation $\langle \mathbf{i},\mathbf{j}\rangle$ means that the sum is over all lattice sites $\{\mathbf{i}\}$ and only nearest-neighbor sites $\{\mathbf{j}\}$ for each $\mathbf{i}$. We will generalize this real-space Hamiltonian for quasicrystalline systems in the next section.

In Ref. [72], the order parameter Δ_s was assumed to be a constant and was not solved for self-consistently. This assumption is reasonable for square lattice systems because of the translational symmetry of the system. Moreover, $\alpha|\mathcal{L}_0(\boldsymbol{k})| \gg \mu_{\text{B}} H_z$ was assumed in Ref. [72]. This is because the supercoducting state would be unstable and TSC would not be realized in the limit of large Zeeman coupling. The momentum-space Hamiltonian in Eq. (5.1) can be rewritten in the 'BdG form' as

$$\mathcal{H} = \frac{1}{2} \sum_{\boldsymbol{k},\sigma,\sigma'} \begin{pmatrix} c^{\dagger}_{\boldsymbol{k}\sigma} & c_{-\boldsymbol{k}\sigma} \end{pmatrix} \mathcal{H}(\boldsymbol{k}) \begin{pmatrix} c_{\boldsymbol{k}\sigma'} \\ c^{\dagger}_{-\boldsymbol{k}\sigma'} \end{pmatrix}, \tag{5.8}$$

where the corresponding BdG Hamiltonian $\mathcal{H}(\boldsymbol{k})$ is

$$\mathcal{H}(\boldsymbol{k}) = \begin{pmatrix} \epsilon(\boldsymbol{k}) - \mu_{\text{B}} H_z \sigma_z + \alpha \mathcal{L}_0(\boldsymbol{k}) \cdot \boldsymbol{\sigma} & \imath \Delta(\boldsymbol{k}) \sigma_y \\ -\imath \Delta(\boldsymbol{k})^* \sigma_y & -\epsilon(\boldsymbol{k}) + \mu_{\text{B}} H_z \sigma_z + \alpha \mathcal{L}_0(\boldsymbol{k}) \cdot \boldsymbol{\sigma}^* \end{pmatrix}. \tag{5.9}$$

Thus, by diagonalizing the BdG Hamiltonian, the energy at the momentum $\boldsymbol{k}$ can be obtained analytically as

$$E(\boldsymbol{k}) = \sqrt{\epsilon(\boldsymbol{k})^2 + \alpha^2 \mathcal{L}_0(\boldsymbol{k})^2 + \mu_{\text{B}}^2 H_z^2 + |\Delta(\boldsymbol{k})|^2 \pm 2\sqrt{\epsilon(\boldsymbol{k})^2 \alpha^2 \mathcal{L}_0(\boldsymbol{k})^2 + \left[\epsilon(\boldsymbol{k})^2 + |\Delta(\boldsymbol{k})|^2\right] \mu_{\text{B}}^2 H_z^2}}. \tag{5.10}$$

One can solve $E(\boldsymbol{k}) = 0$ to find the condition for vanishing energy gap as

$$\epsilon(\boldsymbol{k})^2 + |\Delta(\boldsymbol{k})|^2 = \mu_{\mathrm{B}}^2 H_z^2 + \alpha^2 \mathcal{L}_0(\boldsymbol{k})^2, \quad |\Delta(\boldsymbol{k})|\alpha\mathcal{L}_0(\boldsymbol{k}) = 0. \tag{5.11}$$

A topological phase transition can occur only when the energy gap vanishes, and the above condition yields the phase boundaries in the topological phase diagram. For s-wave pairing, $|\Delta(\boldsymbol{k})|\alpha = \Delta_s\alpha \neq 0$. Thus the second condition of 5.11 is reduced to $\mathcal{L}_0(\boldsymbol{k}) = 0$, and this is satisfied at the high-symmetry points of the first Brillouin zone, $\boldsymbol{k} = (0,0), (0,\pi), (\pi,0), (\pi,\pi)$. Accordingly, three phase boundaries for the s-wave pairing are

$$(4t+\mu)^2 + \Delta_s^2 = (\mu_{\mathrm{B}} H_z)^2, \quad \mu^2 + \Delta_s^2 = (\mu_{\mathrm{B}} H_z)^2, \quad (4t-\mu)^2 + \Delta_s^2 = (\mu_{\mathrm{B}} H_z)^2, \tag{5.12}$$

or equivalently,

$$\left(\frac{\mu_{\mathrm{B}} H_z}{t}\right)^2 - \left(\frac{\Delta_s}{t}\right)^2 = \begin{cases} \left(\frac{\mu}{t} + 4\right)^2, \\ \left(\frac{\mu}{t}\right)^2, \\ \left(\frac{\mu}{t} - 4\right)^2. \end{cases} \tag{5.13}$$

These phase boundaries are illustrated in Fig. 5.1. By drawing three phase boundaries, the whole region is devided into seven areas, which are topologically distinct from each other.

5.1.2 Topological Invariant, Abelian and Non-Abelian Phase

The topological nature of the system can be characterized by the TKNN number or the first Chern number. The BdG equations in momentum space can be written as

$$\mathcal{H}(\boldsymbol{k}) \left|\phi_n(\boldsymbol{k})\right\rangle = E_n(\boldsymbol{k}) \left|\phi_n(\boldsymbol{k})\right\rangle \tag{5.14}$$

for a given $\boldsymbol{k}$. Among these normalized eigenstates $\{|\phi_n(\boldsymbol{k})\rangle\}$, those with negative eigenenergies are occupied single-particle states. Using the occupied states, the Berry connection $A_i^{(-)}(\boldsymbol{k})$ is defined as

$$A_i^{(-)}(\boldsymbol{k}) = \imath \sum_{E_n<0} \left\langle \phi_n(\boldsymbol{k}) \,|\, \partial_{k_i} \phi_n(\boldsymbol{k}) \right\rangle, \tag{5.15}$$

where the subscript i indicates k_x, k_y, and k_z directions for $i = 1, 2$, and 3, respectively. The corresponding Berry curvature $\mathcal{F}^{(-)}(\boldsymbol{k})$ in a two-dimensional system is a scalar,

$$\mathcal{F}^{(-)}(\boldsymbol{k}) = \epsilon^{ij} \partial_{k_i} A_j^{(-)}(\boldsymbol{k}), \tag{5.16}$$

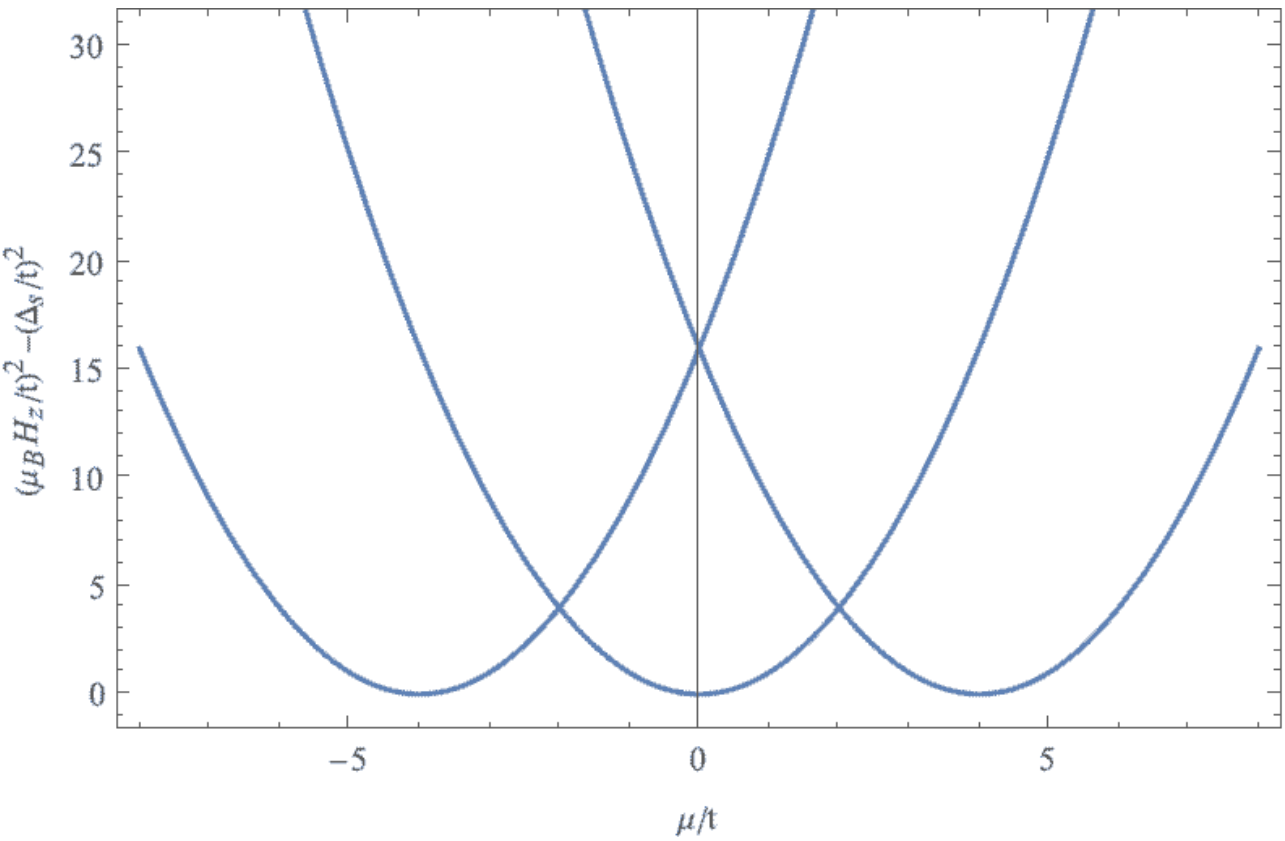

Figure 5.1: Three phase boundaries in the topological phase diagram.

for $i, j = 1, 2$. Here, ϵ^{ij} is the Levi-Civita symbol in two dimensions,

$$\epsilon^{ij} = \begin{cases} +1 & \text{if } (i,j) = (1,2), \\ -1 & \text{if } (i,j) = (2,1), \\ 0 & \text{if } i = j. \end{cases} \tag{5.17}$$

Explicitly written,

$$\mathcal{F}^{(-)}(\boldsymbol{k}) = \partial_{k_1} A_2^{(-)}(\boldsymbol{k}) - \partial_{k_2} A_1^{(-)}(\boldsymbol{k}). \tag{5.18}$$

The corresponding TKNN number I_{TKNN} in this case is defined by integrating the Berry curvature $\mathcal{F}^{(-)}(\boldsymbol{k})$ over the first Brillouin zone T^2,

$$I_{\mathrm{TKNN}} = \frac{1}{2\pi} \int_{T^2} dk_x dk_y \mathcal{F}^{(-)}(\boldsymbol{k}). \tag{5.19}$$

The TKNN number can also be expressed in terms of another topological invariant, the winding number $I(k_y)$, used in the literature [103]. The particle-hole symmetry of the BdG Hamiltonian can be expressed as

$$\Gamma \mathcal{H}(\boldsymbol{k}) \Gamma^\dagger = -\mathcal{H}^*(-\boldsymbol{k}), \tag{5.20}$$

with

$$\Gamma = \begin{pmatrix} 0 & \mathbf{1}_{2\times 2} \\ \mathbf{1}_{2\times 2} & 0 \end{pmatrix}, \tag{5.21}$$

where $\mathbf{1}_{2\times 2}$ is the 2×2 identity matrix. There are two special values of k_y that have $\mathcal{H}(\boldsymbol{k}) = \mathcal{H}^*(-\boldsymbol{k})$. One of them is $k_y = 0$, for which

$$\epsilon(k_x, 0) = -2t(\cos k_x + 1) - \mu, \tag{5.22}$$

$$\epsilon(-k_x, 0)^* = -2t(\cos(-k_x) + 1) - \mu = -2t(\cos k_x + 1) - \mu, \tag{5.23}$$

$$\alpha \mathcal{L}_0(k_x, 0) \cdot \boldsymbol{\sigma} = \alpha \begin{pmatrix} 0 & -\sin k_x \end{pmatrix} \begin{pmatrix} \sigma_x \\ \sigma_y \end{pmatrix} = -\alpha \sigma_y \sin k_x, \tag{5.24}$$

$$\alpha \mathcal{L}_0(-k_x, 0)^* \cdot \boldsymbol{\sigma}^* = \alpha \begin{pmatrix} 0 & -\sin(-k_x) \end{pmatrix} \begin{pmatrix} \sigma_x \\ -\sigma_y \end{pmatrix} = -\alpha \sigma_y \sin k_x. \tag{5.25}$$

Therefore, every element in $\mathcal{H}^*(-\boldsymbol{k})$ coinsides with that of $\mathcal{H}(\boldsymbol{k})$. Similarly, for $k_y = \pi$, $\mathcal{H}(\boldsymbol{k}) = \mathcal{H}^*(-\boldsymbol{k})$. Combining with the particle-hole symmetry, for $k_y = 0, \pi$,

$$\Gamma\mathcal{H}(\boldsymbol{k})\Gamma^\dagger = -\mathcal{H}(\boldsymbol{k}). \tag{5.26}$$

Note that $\Gamma^\dagger\Gamma$ is an identity matrix. Thus, by multiplying the above equation by Γ from the right,

$$\Gamma\mathcal{H}(\boldsymbol{k}) + \mathcal{H}(\boldsymbol{k})\Gamma = [\Gamma, \mathcal{H}(\boldsymbol{k})]_+ = 0. \tag{5.27}$$

Changing the basis so that Γ has the diagonal form,

$$\Gamma = \begin{pmatrix} \mathbf{1}_{2\times 2} & 0 \\ 0 & -\mathbf{1}_{2\times 2} \end{pmatrix}, \tag{5.28}$$

for $k_y = 0, \pi$,

$$\mathcal{H}(\boldsymbol{k}) = \begin{pmatrix} 0 & q(\boldsymbol{k}) \\ q^\dagger(\boldsymbol{k}) & 0 \end{pmatrix}. \tag{5.29}$$

In this basis, the anticommutation relation can be shown as

$$\begin{aligned} [\Gamma, \mathcal{H}(\boldsymbol{k})]_+ &= \begin{pmatrix} \mathbf{1}_{2\times 2} & 0 \\ 0 & -\mathbf{1}_{2\times 2} \end{pmatrix} \begin{pmatrix} 0 & q(\boldsymbol{k}) \\ q^\dagger(\boldsymbol{k}) & 0 \end{pmatrix} + \begin{pmatrix} 0 & q(\boldsymbol{k}) \\ q^\dagger(\boldsymbol{k}) & 0 \end{pmatrix} \begin{pmatrix} \mathbf{1}_{2\times 2} & 0 \\ 0 & -\mathbf{1}_{2\times 2} \end{pmatrix} \\ &= \begin{pmatrix} 0 & q(\boldsymbol{k}) \\ -q^\dagger(\boldsymbol{k}) & 0 \end{pmatrix} + \begin{pmatrix} 0 & -q(\boldsymbol{k}) \\ q^\dagger(\boldsymbol{k}) & 0 \end{pmatrix} \\ &= 0. \end{aligned} \tag{5.30}$$

The winding number for a given k_y is defined by

$$I(k_y) = \frac{1}{4\pi\imath} \int_{-\pi}^{\pi} dk_x \, \mathrm{Tr}\left[q^{-1}(\boldsymbol{k})\partial_{k_x} q(\boldsymbol{k}) - q^{\dagger -1}(\boldsymbol{k})\partial_{k_x} q^\dagger(\boldsymbol{k})\right], \tag{5.31}$$

or equivalently,

$$\begin{aligned} I(k_y) &= -\frac{1}{2\pi\imath} \int_{-\pi}^{\pi} dk_x \, \mathrm{Tr}\left[q(\boldsymbol{k})\partial_{k_i} q^{-1}(\boldsymbol{k})\right] \\ &= \frac{1}{2\pi\imath} \int_{-\pi}^{\pi} dk_x \, \partial_{k_i} \ln\left[\det q(\boldsymbol{k})\right]. \end{aligned} \tag{5.32}$$

This winding number is related with the TKNN number by [72]

$$(-1)^{I_{\mathrm{TKNN}}} = (-1)^{I(0) - I(\pi)}. \tag{5.33}$$

This relation assures that $(-1)^{I_{\mathrm{TKNN}}}$ can be obtained by calculating the winding number at two specific wave numbers $k_y = 0, \pi$. The value of $(-1)^{I_{\mathrm{TKNN}}}$ determines whether the system is in the trivial, Abelian topological, or non-Abelian topological phase. When at least one of them is nonzero, we have either Abelian or non-Abelian topological phase:

$$(-1)^{I_{\mathrm{TKNN}}} = \begin{cases} +1, \text{Abelian}, \\ -1, \text{non-Abelian}. \end{cases} \tag{5.34}$$

In this TSC model, $I(0)$ and $I(\pi)$ can be -1, 0, or $+1$. When both $I(0)$ and $I(\pi)$ are zero, the system is in the topologically trivial phase. When $I(0) - I(\pi) = \pm 1$, $(-1)^{I_{\mathrm{TKNN}}} = -1$, there is a single Majorana fermion on a surface boundary or in a vortex [72, 104, 73]. This topological phase is said to be non-Abelian, as Majorana fermions obey the non-Abelian exchange statistics. Unlike its continuum-model counterpart [104], this tight-binding TSC model also has the possibility of $I(0) = -1$ and $I(\pi) = 1$, so that $I_{\mathrm{TKNN}} = -2$ and $(-1)^{I_{\mathrm{TKNN}}} = +1$, which is topologically non-trivial and called the Abelian phase. According to the bulk-edge correspondence [13, 14], the magnitude of I_{TKNN} equals the number of zero-energy modes per surface boundary. So in the Abelian phase, there are two Majorana fermions per surface [74]. The index theorem [104] for a vortex in the Abelian phase has recently been derived, showing the possible existence of two Majorana fermions per vortex, although numerically it has been found that those two Majorana fermions annihilate each other due to overlap of their wave functions in a vortex [105]. In summary, Table 5.1 shows the value of $(-1)^{I_{\mathrm{TKNN}}}$ as an indicator of Abelian or non-Abelian topological phase and the winding numbers at two specific wave numbers $k_y = 0, \pi$, for various regions of the chemical potential and Zeeman coupling.

Table 5.1: List of the values of $(-1)^{I_{\text{TKNN}}}$ and the winding numbers as an indicator of trivial, Abelian or non-Abelian topological phase for various regions of the chemical potential and Zeeman coupling.

(a) $\mu \leq -2t$			
$(\mu_B H_z)^2$	$(-1)^{I_{\text{TKNN}}}$	$I(0)$	$I(\pi)$
$0 < (\mu_B H_z)^2 < (4t+\mu)^2 + \Delta_s^2$	1	0	0
$(4t+\mu)^2 + \Delta_s^2 < (\mu_B H_z)^2 < \mu^2 + \Delta_s^2$	-1	1	0
$\mu^2 + \Delta_s^2 < (\mu_B H_z)^2 < (4t-\mu)^2 + \Delta_s^2$	-1	0	1
$(4t-\mu)^2 + \Delta_s^2 < (\mu_B H_z)^2$	1	0	0
(b) $-2t < \mu \leq 0$			
$(\mu_B H_z)^2$	$(-1)^{I_{\text{TKNN}}}$	$I(0)$	$I(\pi)$
$0 < (\mu_B H_z)^2 < \mu^2 + \Delta_s^2$	1	0	0
$\mu^2 + \Delta_s^2 < (\mu_B H_z)^2 < (4t+\mu)^2 + \Delta_s^2$	1	-1	1
$(4t+\mu)^2 + \Delta_s^2 < (\mu_B H_z)^2 < (4t-\mu)^2 + \Delta_s^2$	-1	0	1
$(4t-\mu)^2 + \Delta_s^2 < (\mu_B H_z)^2$	1	0	0
(c) $0 < \mu \leq 2t$			
$(\mu_B H_z)^2$	$(-1)^{I_{\text{TKNN}}}$	$I(0)$	$I(\pi)$
$0 < (\mu_B H_z)^2 < \mu^2 + \Delta_s^2$	1	0	0
$\mu^2 + \Delta_s^2 < (\mu_B H_z)^2 < (4t-\mu)^2 + \Delta_s^2$	1	-1	1
$(4t-\mu)^2 + \Delta_s^2 < (\mu_B H_z)^2 < (4t+\mu)^2 + \Delta_s^2$	-1	-1	0
$(4t+\mu)^2 + \Delta_s^2 < (\mu_B H_z)^2$	1	0	0
(d) $2t < \mu$			
$(\mu_B H_z)^2$	$(-1)^{I_{\text{TKNN}}}$	$I(0)$	$I(\pi)$
$0 < (\mu_B H_z)^2 < (4t-\mu)^2 + \Delta_s^2$	1	0	0
$(4t-\mu)^2 + \Delta_s^2 < (\mu_B H_z)^2 < \mu^2 + \Delta_s^2$	-1	0	-1
$\mu^2 + \Delta_s^2 < (\mu_B H_z)^2 < (4t+\mu)^2 + \Delta_s^2$	-1	-1	0
$(4t+\mu)^2 + \Delta_s^2 < (\mu_B H_z)^2$	1	0	0

5.1.3 Majorana Chiral Edge State with the Ribbon Boundary Condition

When a system with a surface or edge boundary is in topological phase with a nonzero topological invariant, the existence of zero-energy edge mode(s) along the boundary is guaranteed by the bulk-edge correspondence [13, 14]. The Hamiltonian described in the momentum space in Eq. (5.1) is applicable only for a square lattice with PBC, and accordingly, never yields edge modes. For a square lattice of N sites, the lattice version of Eq. (5.1) is given by Eq. (5.4). The model in Eq. (5.4) presents the Majorana chiral edge mode(s) with the ribbon boundary condition [72]. For example, with the ribbon boundary condition, a square-lattice system can have PBC in the y direction and two edges at $x = 0$ and $x = N_x - 1$, where N_x is the number of lattice sites in the x direction.

The energy spectrum of Eq. (5.4) with the ribbon boundary condition for $N_x = 15$ is shown in Fig. 5.2. The horizontal axis represents the wave number in the y direction which ranges between $-\pi$ and π, and the vertical axis represents the energy in units of $t \equiv 1$. The parameters used are $\mu = -2.5, \alpha = 1.0 (\lambda = 0.5), \Delta_s = 1.0$ and each panel corresponds to different values of $\mu_{\rm B} H_z$: (a) $\mu_{\rm B} H_z = 0.0$ ($(\mu_{\rm B} H_z)^2 = 0.0$), (b) $\mu_{\rm B} H_z = 2.0$ ($(\mu_{\rm B} H_z)^2 = 4.0$), (c) $\mu_{\rm B} H_z = 3.0$ ($(\mu_{\rm B} H_z)^2 = 9.0$), and (d) $\mu_{\rm B} H_z = 7.0$ ($(\mu_{\rm B} H_z)^2 = 49.0$).

The region in Table 5.1 (a) for $\mu \leq -2.0t$ along with the used set of parameters is shown in Table 5.2. According to Table 5.2, the topological phases of the four panels in Fig. 5.2 are (a) Abelian, (b) non-Abelian, (c) non-Abelian, and (d) Abelian. When the system is in the non-Abelian topological phase, the energy spectrum has a zero-energy band crossing in the first Brillouin zone, which corresponds to two Majorana chiral edge modes. To show these band crossings clearer, the low-energy region of the energy spectra of the non-Abelian topological phase in Fig. 5.2 (b) and (c) is magnified in Fig. 5.3. Two energy bands cross zero energy at $k_y = 0$ for $\mu_{\rm B} H_z = 2.0$ in Fig. 5.3 (b) and at the Brillouin zone boundary, $k_y = \pm\pi$, for $\mu_{\rm B} H_z = 3.0$ in Fig. 5.3 (c). At these values of k_y, $I(k_y) \neq 0$. The winding numbers at these band-crossing wave numbers are (b) $I(0) = 1$ and (c) $I(\pi) = 1$. In each case, one Majorana zero mode appears along each of the two surfaces.

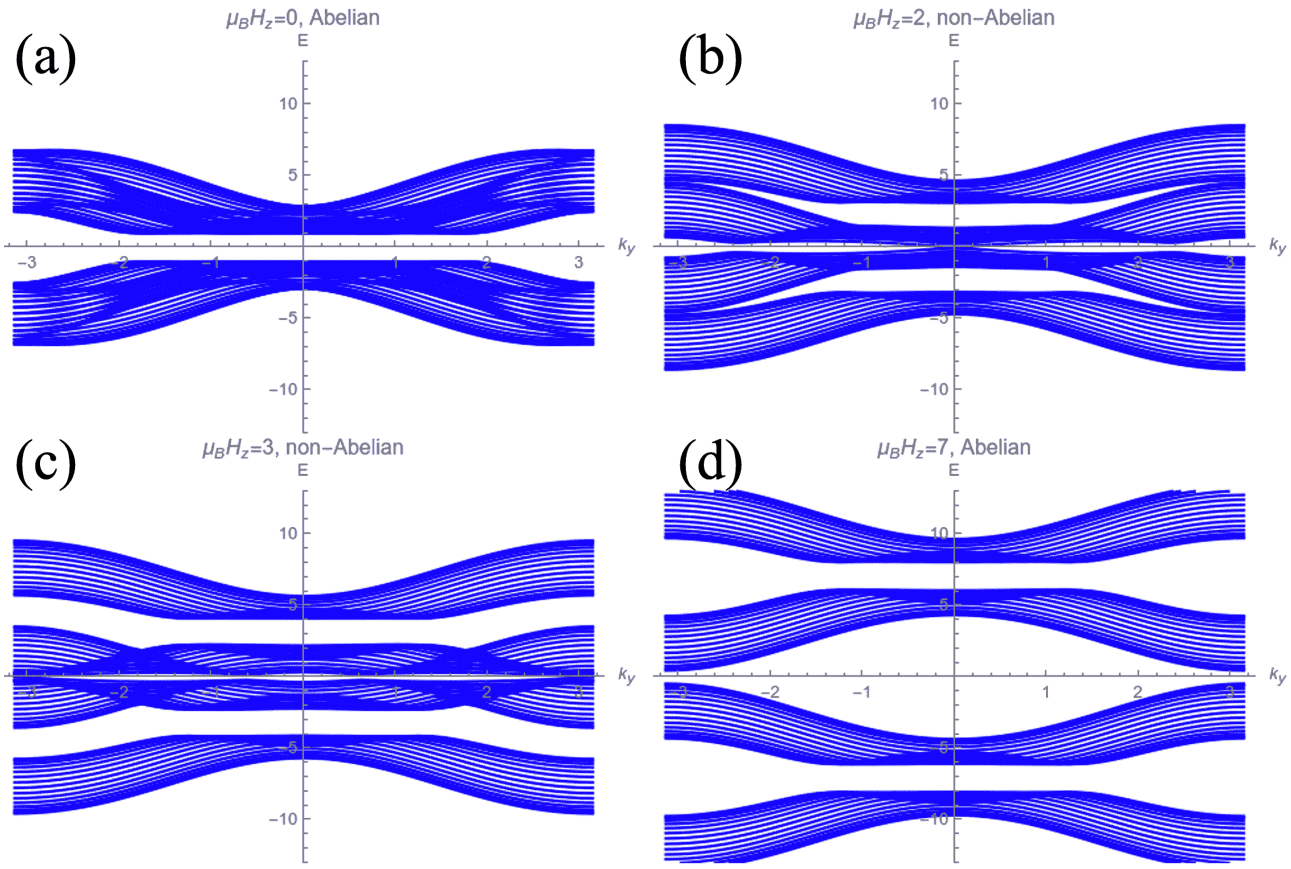

Figure 5.2: The eigenspectrum of Eq. (5.4) in units of t as a function of k_y in the first Brillouin zone with the ribbon boundary condition for $N_x = 15$. The parameters used are $\mu = -2.5, \alpha = 1.0, \Delta_s = 1.0$, and (a) $\mu_{\rm B} H_z = 0.0$, (b) $\mu_{\rm B} H_z = 2.0$, (c) $\mu_{\rm B} H_z = 3.0$, and (d) $\mu_{\rm B} H_z = 7.0$. The topological phases are (a) Abelian, (b) non-Abelian, (c) non-Abelian, and (d) Abelian.

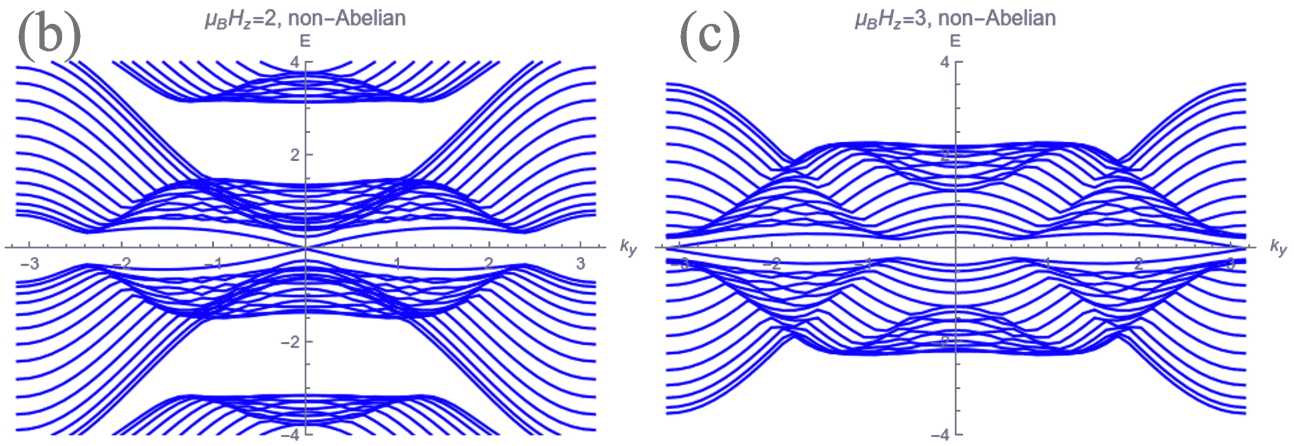

Figure 5.3: Low-energy region of the eigenspectrum of the non-Abelian topological phase in Fig. 5.2 (b) and (c), showing two Majorana fermions at $k_y = 0$ and $k_y = \pi$, respectively.

Table 5.2: Table 5.1 (a) for $\mu \leq -2.0t$, with $\mu = -2.5, \alpha = 1.0$, and $\Delta_s = 1.0$.

$(\mu_{\rm B} H_z)^2$	$(-1)^{I_{\rm TKNN}}$	$I(0)$	$I(\pi)$
$0 < (\mu_{\rm B} H_z)^2 < 3.25$	1	0	0
$3.25 < (\mu_{\rm B} H_z)^2 < 7.25$	-1	1	0
$7.25 < (\mu_{\rm B} H_z)^2 < 43.25$	-1	0	1
$43.25 < (\mu_{\rm B} H_z)^2$	1	0	0

In contrast, two Majorana chiral edge states appear per surface boundary when the system is in the Abelian topological phase. The low-energy region of the energy spectrum of Eq. (5.4) with the ribbon boundary condition for $N_x = 15$, in the case of $\mu = -1.0, \alpha = 1.0(\lambda = 0.5)$, and $\Delta_s = 1.0$ is shown in Fig. 5.4. The system is in the Abelian topological phase with this parameter set, according to Table 5.1. There are two band crossings at $k_y = 0$ and π at zero energy, each of which corresponds to two Majorana zero modes per surface, and both of the winding numbers at these wave numbers are nonzero: $I(0) = -1$, $I(\pi) = 1$.

In this subsection, it has been demonstrated that zero-energy Majorana modes appear along surface boundaries and the number of Majorana zero modes per surface is given by $|I_{TKNN}|= 1$ and 2, respectively, in the non-Abelian and Abelian phase.

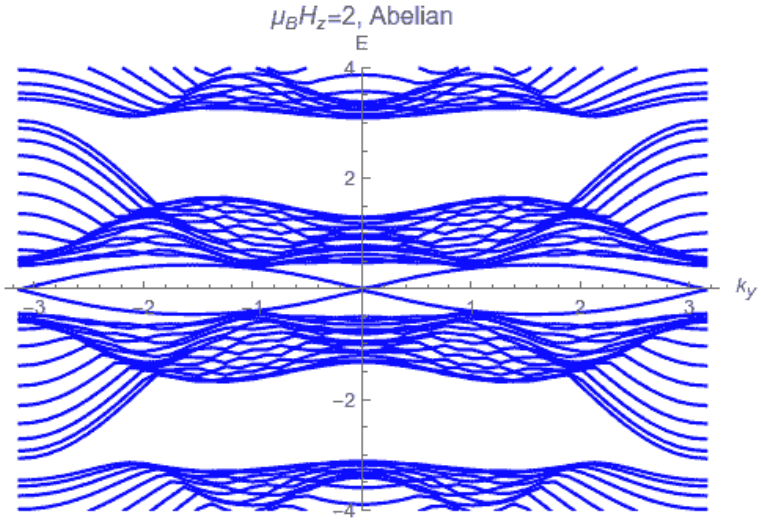

Figure 5.4: Low-energy region of the energy spectrum of Eq. (5.4) with the ribbon boundary condition for $N_x = 15$, $\mu = -1.0, \alpha = 1.0(\lambda = 0.5)$, and $\Delta_s = 1.0$

5.2 Topological Superconductivity Model for Two-Dimensional Quasicrystals

5.2.1 Topological Invariant for Quasicrystals: Bott Index

The Bott index is one of the topological invariants which can be used also for a system without periodicity and is equivalent to the first Chern number in a periodic system [106, 107]. The first Chern number is defined in momentum space and not applicable to systems that lack periodicity. In this subsection, the definition of the Bott index is provided [69, 68]. First, let P be the projector onto the states below the Fermi energy,

$$P = \sum_{E_n<0} |\phi_n\rangle \langle\phi_n| . \tag{5.35}$$

Then the projection operator onto its complementary space is

$$Q = I - P, \tag{5.36}$$

where I is the identity operator. The projected position operator for coordinate x is difined as

$$U_X = Pe^{i2\pi X}P + Q. \tag{5.37}$$

Here, X is a diagonal matrix defined as

$$X = \mathrm{Diag}\left(x_1, x_1, \ldots, x_N, x_N, x_1, x_1, \ldots, x_N, x_N\right), \tag{5.38}$$

where x_i is the x coordinate of the ith vertex rescaled to $[0, 1)$. Similarly, the projected position operator for coordinate y is difined as

$$U_Y = Pe^{\imath 2\pi Y}P + Q, \tag{5.39}$$

where Y is a diagonal matrix defined as

$$Y = \mathrm{Diag}\left(y_1, y_1, \ldots, y_N, y_N, y_1, y_1, \ldots, y_N, y_N\right), \tag{5.40}$$

and y_i is the y coordinate of the ith vertex rescaled to $[0, 1)$. The Bott index in a two-dimensional system is defined as

$$B = \frac{1}{2\pi}\mathrm{Im}\,\mathrm{Tr}\log\left(U_Y U_X U_Y^\dagger U_X^\dagger\right). \tag{5.41}$$

The matrices U_X and U_Y are known to be almost unitary and commute with each other, and they can be approximated by exactly commuting matrices through the techniques of C^*-algebras [69]. The Bott index satisfies

$$\mathrm{Tr}\,\log\left(U_Y U_X U_Y^\dagger U_X^\dagger\right) = 2\pi\imath B + r, \tag{5.42}$$

namely,

$$\det\left(U_Y U_X U_Y^\dagger U_X^\dagger\right) = \exp\left(2\pi\imath B + r\right), \tag{5.43}$$

where r is a real number. Since $\det\left(U_X\right) = \left(\det\left(U_X^\dagger\right)\right)^*$ and $\det\left(U_Y U_X U_Y^\dagger U_X^\dagger\right) > 0$, the Bott index is quantized to be an integer.

When U_X and U_Y are unitary and mutually commute, $\det\left(U_Y U_X U_Y^\dagger U_X^\dagger\right) = 1 = \exp(0)$, and thus $B = r = 0$. It is known that if and only if $B = 0$, U_X and U_Y exactly commute with each other [108]. The Bott index is an integer quantity which is nonzero (zero) in a topologically nontrivial (trivial) phase [68].

The chemical potential and Zeeman coupling dependence of the Bott index, calculated for the BdG Hamiltonian given by Eq. (5.9) for a 20×20 square lattice system with PBC, $\alpha = 1.0t$ and $\Delta_s = 0.34t$, is shown in Fig. 5.5. The three parabolic curves in Fig. 5.5 are

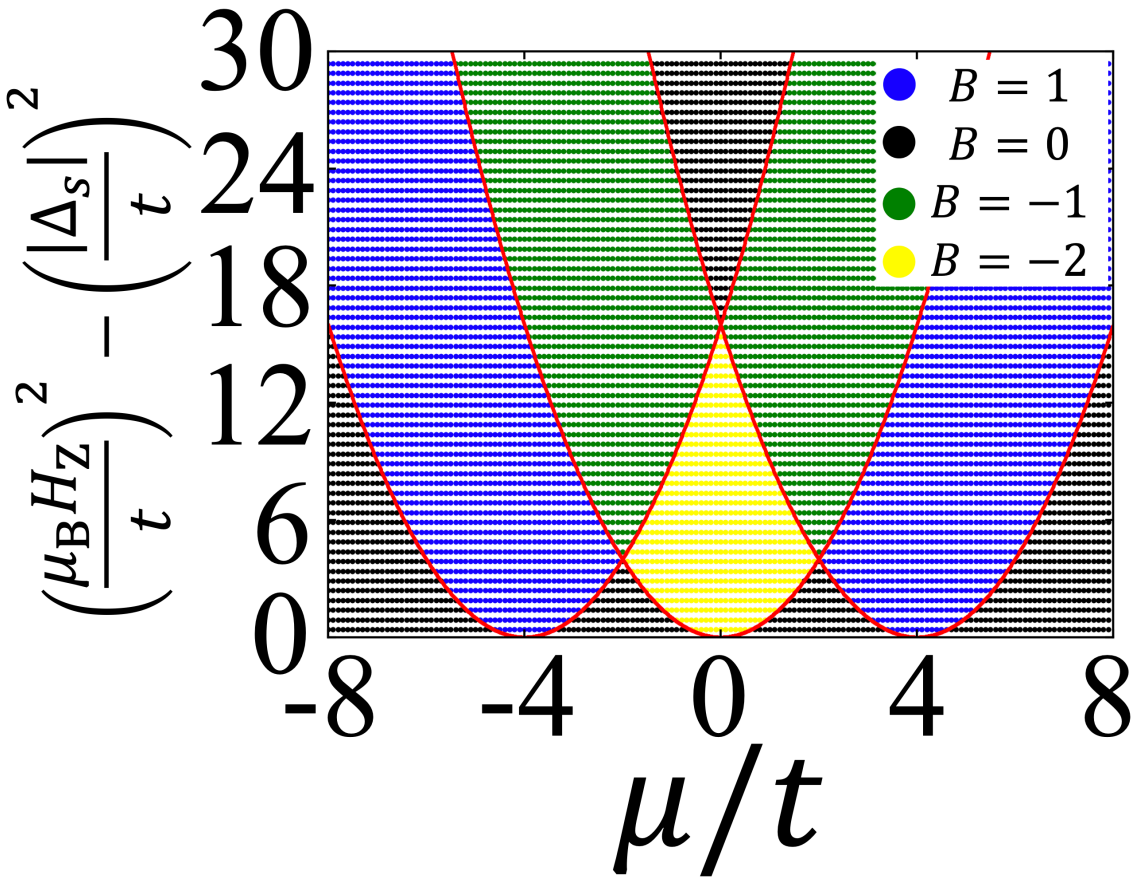

Figure 5.5: The chemical potential and Zeeman coupling dependence of the Bott index for a 20×20 square lattice system with PBC, $\alpha = 1.0t$, and $\Delta_s = 0.34t$.

the topological phase boundaries in Eq. (5.13). Comparing the numerically calculated Bott index in Fig. 5.5 with the analytically derived winding numbers shown in Table 5.1, we find $B = I(0) - I(\pi)$ for translation-invariant systems. Therefore, the Bott index is an alternative topological invariant, which does not require translational symmetry, and B is zero (nonzero) for topologically trivial (nontrivial) phase.

5.2.2 Model Hamiltonian for Two-Dimensional Quasicrystals

Translational symmetry can be utilized in the case of square lattice systems; however, for QCs, due to the lack of translational symmetry Bloch's theorem does not hold. Accordingly, the Hamiltonian of the TSC model should be generalized in coordinate space [68]:

$$\mathcal{H} = \frac{1}{2} \sum_{ij} \begin{pmatrix} c_i^\dagger & c_i \end{pmatrix} H \begin{pmatrix} c_j \\ c_j^\dagger \end{pmatrix}, \tag{5.44}$$

$$H = \begin{pmatrix} \mathbf{h} & \mathbf{\Delta} \\ \mathbf{\Delta}^\dagger & -\mathbf{h}^* \end{pmatrix}, \tag{5.45}$$

where $c_i = (c_{1\uparrow} c_{1\downarrow} \ldots)$ is the spinor annihilation operator for electrons. The components of H are

$$[\mathbf{h}]_{i\alpha,j\beta} = \left[(t_{ij} - \mu\delta_{ij})\sigma_0 + h_z \delta_{ij}\sigma_3 + \imath V_{ij} \vec{e_z} \cdot \vec{\sigma} \times \hat{\vec{R}}_{ij} \right]_{\alpha\beta}, \tag{5.46}$$

$$[\mathbf{\Delta}]_{i\alpha,j\beta} = [\delta_{ij} \Delta \imath \sigma_2]_{\alpha\beta}. \tag{5.47}$$

The Pauli matrices are $\vec{\sigma} = \begin{pmatrix} \sigma_1 & \sigma_2 & \sigma_3 \end{pmatrix}$ which act in spin space, and σ_0 is the 2×2 identity matrix. The unit vector connecting sites i and j is $\hat{\vec{R}}_{ij}$. The hopping and the Rashba spin-orbit coupling are considered only for nearest-neighbors with $t_{ij} = t_{\langle ij \rangle} = -t$ and $V_{ij} = V_{\langle ij \rangle} = V$, respectively. The Rashba spin-orbit coupling term is

$$\begin{aligned} \imath V_{ij} \vec{e_z} \cdot \vec{\sigma} \times \hat{\vec{R}}_{ij} &= \imath V \begin{pmatrix} 0 \\ 0 \\ 1 \end{pmatrix} \cdot \begin{pmatrix} \sigma_1 & \sigma_2 & \sigma_3 \end{pmatrix} \times \begin{pmatrix} x_{ij} \\ y_{ij} \\ z_{ij} \end{pmatrix} \\ &= \imath V_{ij} \left(y_{ij}\sigma_1 - x_{ij}\sigma_2 \right) \\ &= \imath V_{ij} \begin{pmatrix} 0 & \imath x_{ij} + y_{ij} \\ -\imath x_{ij} + y_{ij} & 0 \end{pmatrix}. \end{aligned} \tag{5.48}$$

It can be confirmed readily that Eq. (5.44) coinsides with Eq. (5.4) in the case of square lattice systems, considering that the four displacement vectors for every lattice point in a square lattice in units of the lattice constant are

$$\vec{R}_{ij} = \left(1, 0\right), \left(0, 1\right), \left(-1, 0\right), \left(0, -1\right). \tag{5.49}$$

Also for Penrose or AB QC, the lengths of the displacement vectors are uniform. Let the common length of the displacement vectors be $|\vec{R}_{ij}| = |\vec{R}|$, which is analogous to the lattice constant in a square lattice. In the case of Penrose QC, displacement vectors of a given site are some of

$$\begin{aligned} \vec{R}_{ij} = |\vec{R}|\Big(\cos 0^\circ, \sin 0^\circ\Big), |\vec{R}|\Big(\cos 72^\circ, \sin 72^\circ\Big), |\vec{R}|\Big(\cos 144^\circ, \sin 144^\circ\Big), \\ |\vec{R}|\Big(\cos 216^\circ, \sin 216^\circ\Big), |\vec{R}|\Big(\cos 288^\circ, \sin 288^\circ\Big). \end{aligned} \tag{5.50}$$

In the case of AB QC, displacement vectors of a certain site are some of

$$\begin{aligned}\vec{R}_{ij} = &|\vec{R}|\Big(\cos 0^\circ, \sin 0^\circ\Big), |\vec{R}|\Big(\cos 45^\circ, \sin 45^\circ\Big), |\vec{R}|\Big(\cos 90^\circ, \sin 90^\circ\Big), \\ &|\vec{R}|\Big(\cos 135^\circ, \sin 135^\circ\Big), |\vec{R}|\Big(\cos 180^\circ, \sin 180^\circ\Big), |\vec{R}|\Big(\cos 225^\circ, \sin 225^\circ\Big), \\ &|\vec{R}|\Big(\cos 270^\circ, \sin 270^\circ\Big), |\vec{R}|\Big(\cos 315^\circ, \sin 315^\circ\Big).\end{aligned} \tag{5.51}$$

In both Penrose and AB QC, the unit vector is given by $\hat{\vec{R}}_{ij} = \dfrac{\vec{R}_{ij}}{|\vec{R}|}$. The number of displacement vectors for a given site is equal to its coordination number, which depends on the local geometry of the site. In the case of AB QC, there are six possible values for the coordination number Z_i which ranges from $Z_i = 3$ to $Z_i = 8$, as illustrated in Fig. 5.6. For instance, the lattice point whose coordination number is $Z_i = 8$ is connected with eight neighboring lattice points, and its corresponding displacement vectors are all of Eq. (5.51).

5.3 Self-consistent Study of Topological Superconductivity in Quasicrystals

In this section, the results of self-consistent calculations for the TSC Hamiltonian in Penrose and AB QCs are shown. For both systems, not only the superconducting order parameter, but also the spin-dependent Hartree potential are obtained self-consistently.

5.3.1 Topological Superconductivity in Penrose Quasicrystals

We have solved the BdG equations self-consistently for the superconducting order parameter and Hartree potential in Penrose QCs with PBC. In converged solutions, both mean fields are found to be spatially non-uniform and vary from site to site; however, they are nonzero at all sites. To characterize the topological nature of the system, we have calculated the Bott index in Eq. (5.41). The magnitude of the self-consistently obtained order parameter Δ_i/t is presented in Fig. 5.7 for the trivial ($B = 0$) and topological ($B = 1$) phase for part of the QC around a high-symmetry point in real space (upper panel) and the perpendicular space (lower panel). The high symmetry point in the upper panel is represented by a black dot.

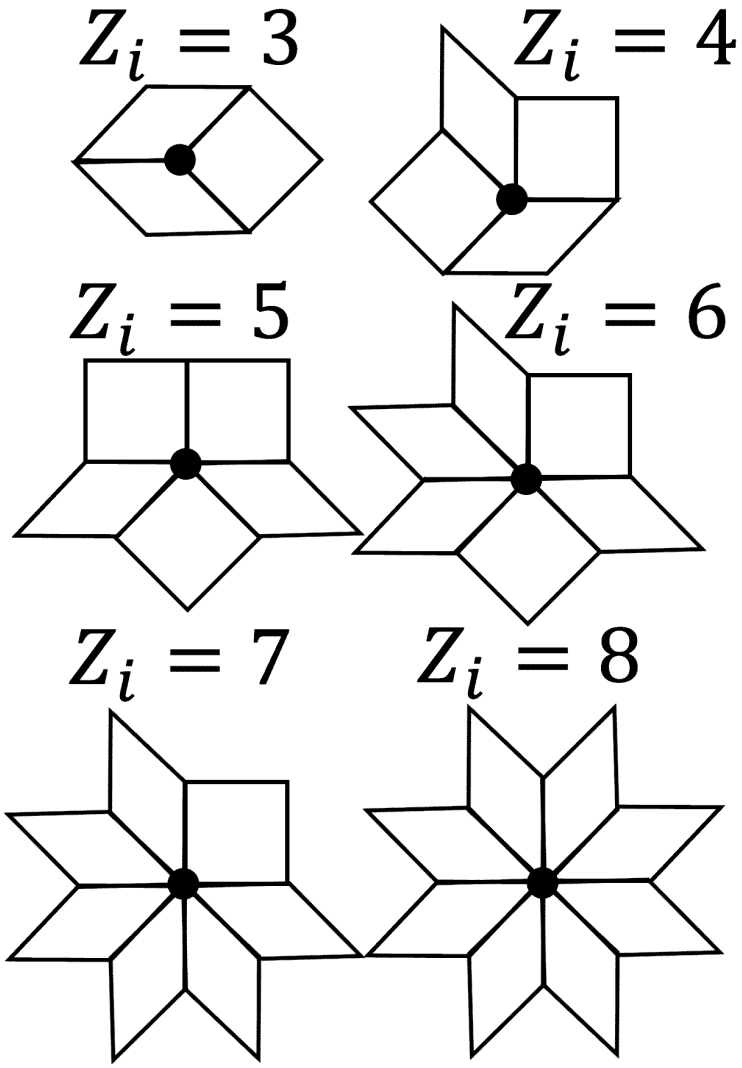

Figure 5.6: Coordination number of a certain site and its nearest-neighbor sites in AB QC.

Among the four planes in the perpendicular space of a Penrose QC shown in Fig. 4.8, the plane at $\tilde{z} = -1.34164$ in Fig. 4.8 (c) is selected for illustration. In the perpendicular space (lower panel), each sector separated by the black solid lines is formed by points with the same coordination number. The parameters used are $h/t = 1.0, \alpha/t = 1.0, U/t = -5.2$, and $\tilde{\mu}/t = 3.7(3.8)$ for the Bott index $B = 0(1)$. The number of lattice points in the used Penrose QC is 3571, and Eq. (2.28) is used for the convergence criteria. The zero (nonzero) Bott index indicates that the system is in a trivial (topological) phase. Figure 5.7 demonstrates that despite the spatial variation of the order parameter, TSC can exist stably in Penrose QC. It can be seen clearly that $|\Delta_i/t|$ has fivefold rotational symmetry whose center of rotation is the black point in Fig. 5.7 and mirror symmetry whose axes of reflection are the black dashed lines in Fig. 5.7 in both real space and the perpendicular space. While it is difficult to see this in real space, the plot in the perpendicular space in Fig. 5.7 illustrates that the magnitude of the order parameter at a given site is mostly determined by its coordination number, i.e., the number of nearest-neighbor sites. And the higher the coordination number, the larger the $|\Delta_i|/t$.

Arg (Δ_i/t) is presented in Fig. 5.8 for the trivial $(B = 0)$ and topological $(B = 1)$ phase for part of the QC around the high-symmetry point (black dot) in real space (upper panel) and the perpendicular space (lower panel). Even though we start from a real initial guess for the order parameter, the converged order parameter in a QC is always complex. It can be seen that Arg (Δ_i/t) has fivefold rotational symmetry whose center of rotation is the black point in Fig. 5.8; however, the mirror symmetry whose axes of reflection are the black dashed lines in Fig. 5.8 is broken in both real space and the perpendicular space. To be accurate, fivefold rotational symmetry is broken near the system boundaries (not shown). Except this effect of finite system size, Arg (Δ_i/t) at a given site and its reflection through any one of the black dashed lines are equal in magnitude and have opposite signs, which we call "anti-mirror symmetry". This "anti-mirror symmetry" also guarantees that Arg $(\Delta_i/t) = 0$ for any lattice site i on the black dashed lines. The spatially varying imaginary part of the superconducting order parameter implies the occurrence of supercurrents.

In Fig. 5.7, $|\Delta_i/t|$ is uniformly distributed in the given scale in each sector for a given coordination number, while Arg (Δ_i/t) is not correlated with the coordination number as can

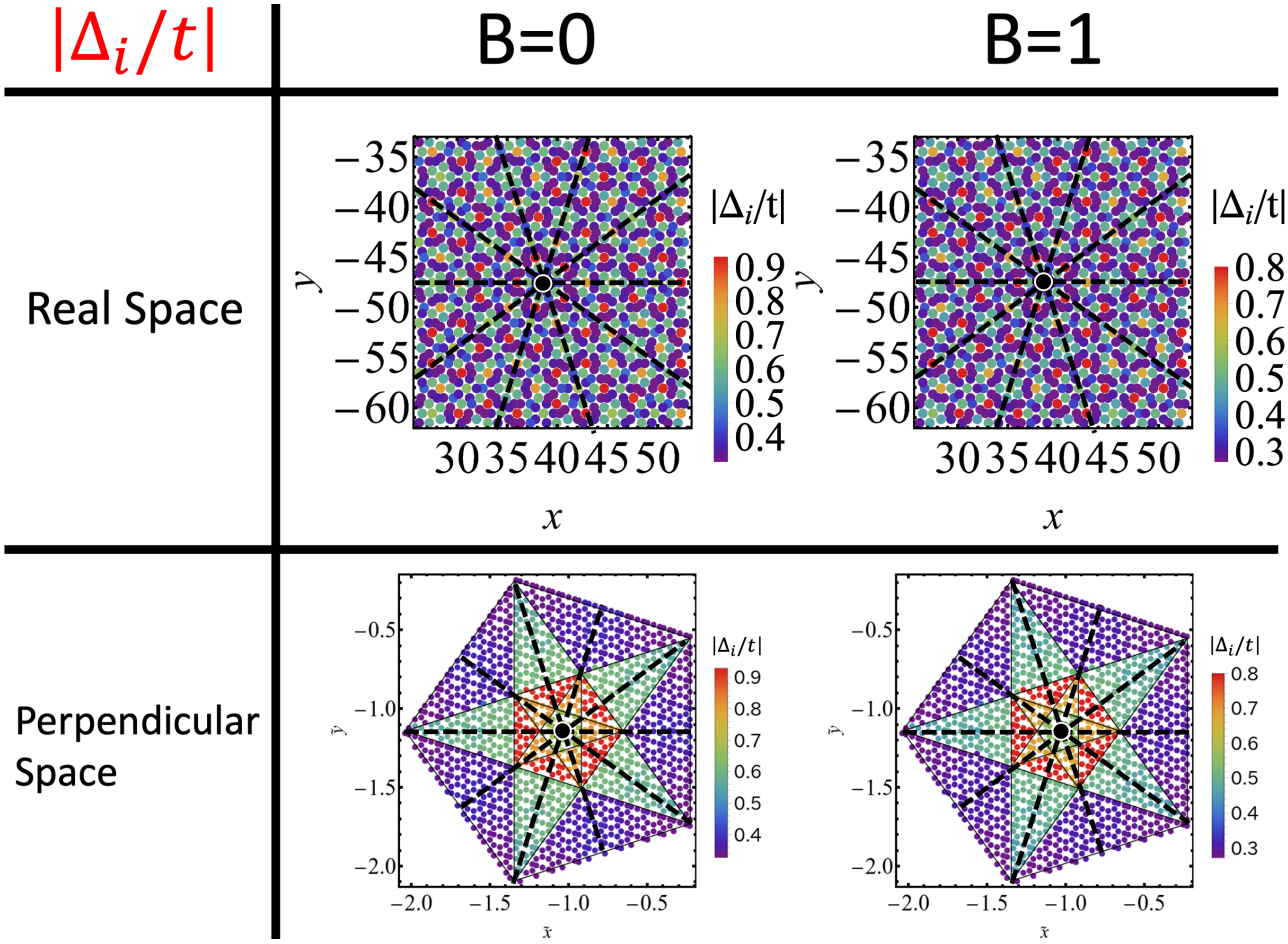

Figure 5.7: The magnitude of Δ_i/t for the trivial ($B = 0$) and topological ($B = 1$) phase in Penrose QC in real space (upper panel) and the perpendicular space (lower panel). The parameters used are $h/t = 1.0, \alpha/t = 1.0, U/t = -5.2$, and $\tilde{\mu}/t = 3.7(3.8)$ for the Bott index $B = 0(1)$, $N = 3571$.

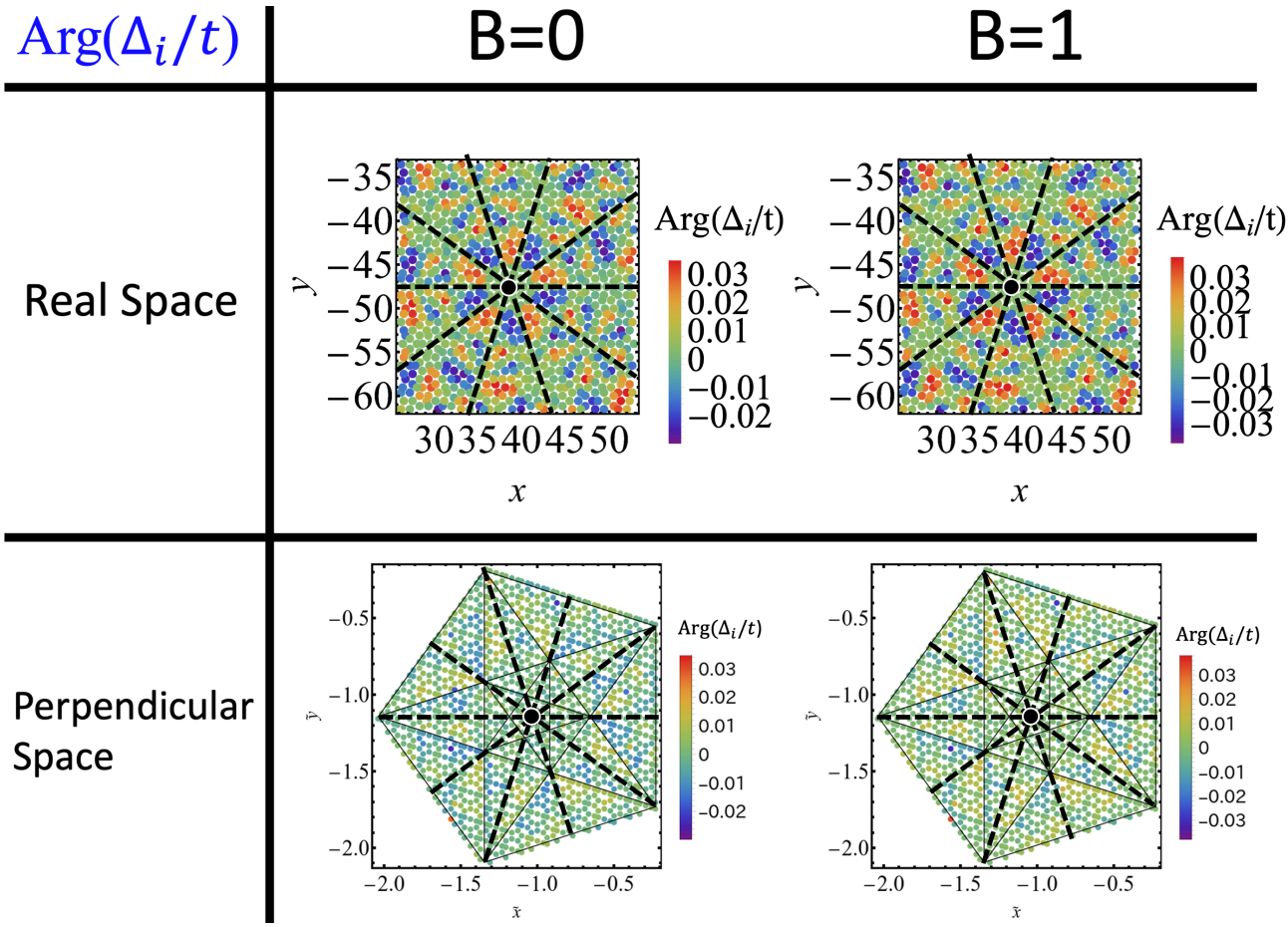

Figure 5.8: Arg (Δ_i/t) for the trivial $(B = 0)$ and topological $(B = 1)$ phase in real space (upper panel) and the perpendicular space (lower panel) for the same systems as shown in Fig. 5.7.

be seen in Fig. 5.8. To examine the dependence of $|\Delta_i/t|$ and Arg (Δ_i/t) on coordination numbers in more detail, $|\Delta_i/t|$ (upper panel) and Arg (Δ_i/t) (lower panel) are plotted as a function of coordination number for the trivial ($B = 0$) and topological ($B = 1$) phase in Fig.5.9. The red dots and the error bars in the dependence of $|\Delta_i/t|$ on coordination numbers represent the mean value and standard deviation for each coordination number, respectively. The black dashed line in the upper (lower) panel represents the mean value of $|\Delta_i/t|$ (Arg (Δ_i/t)) for the entire lattice. Because the standard deviation of $|\Delta_i/t|$ is small, the most dominant factor affecting the value of $|\Delta_i/t|$ is the coordination number. Within the mean-field approximation, it makes sense that the coordination number, i.e., the number of adjacent lattice points governs the strength of the mean fields for a given lattice point. Meanwhile, the standard deviation of $|\Delta_i/t|$ is not exactly zero. This means that not only the local environment but also the global environment may affect $|\Delta_i/t|$. The mean value of Arg (Δ_i/t) for the entire lattice is found to be almost zero, 9.8861×10^{-7} and -2.3989×10^{-6}, in the trivial ($B = 0$) and topological ($B = 1$) phase, respectively. Figure 5.9 clearly shows that Arg (Δ_i/t) does not depend on the coordination number. The strength of the Hartree potential for each spin, which is proportional to the electron density and hence always real, is also governed by the coordination number for each lattice site (not shown).

Comparing the cases of the trivial ($B = 0$) and topological ($B = 1$) phase in Figs. 5.7–5.9, it can be seen that with PBC, the topology of the system does not affect the distribution of the superconducting order parameter. The major difference between trivial and topological phases manifests itself in the presence of an edge (open boundary), as shown below.

The system size dependence of the lowest absolute value of the eigenenergies is shown in Fig. 5.10 for the two parameter sets for $B = 0$ and 1 with the ribbon boundary condition. The numbers of lattice points N of the used Penrose QCs are $N = 199, 1364$, and 3571. The horizontal axis of Fig. 5.10 is the inverse of the square root of the number of lattice points. The blue circles (red squares) represent the results for $B = 0$ ($B = 1$). By linearly fitting these data points for different system sizes, the lowest eigenvalue is found to approach zero in the limit $N \to \infty$ for $B = 1$, while it apparently approaches a finite (nonzero) value for $B = 0$.

In Fig. 5.11, the first (red circle), second (green circle), third (blue circle), and fourth

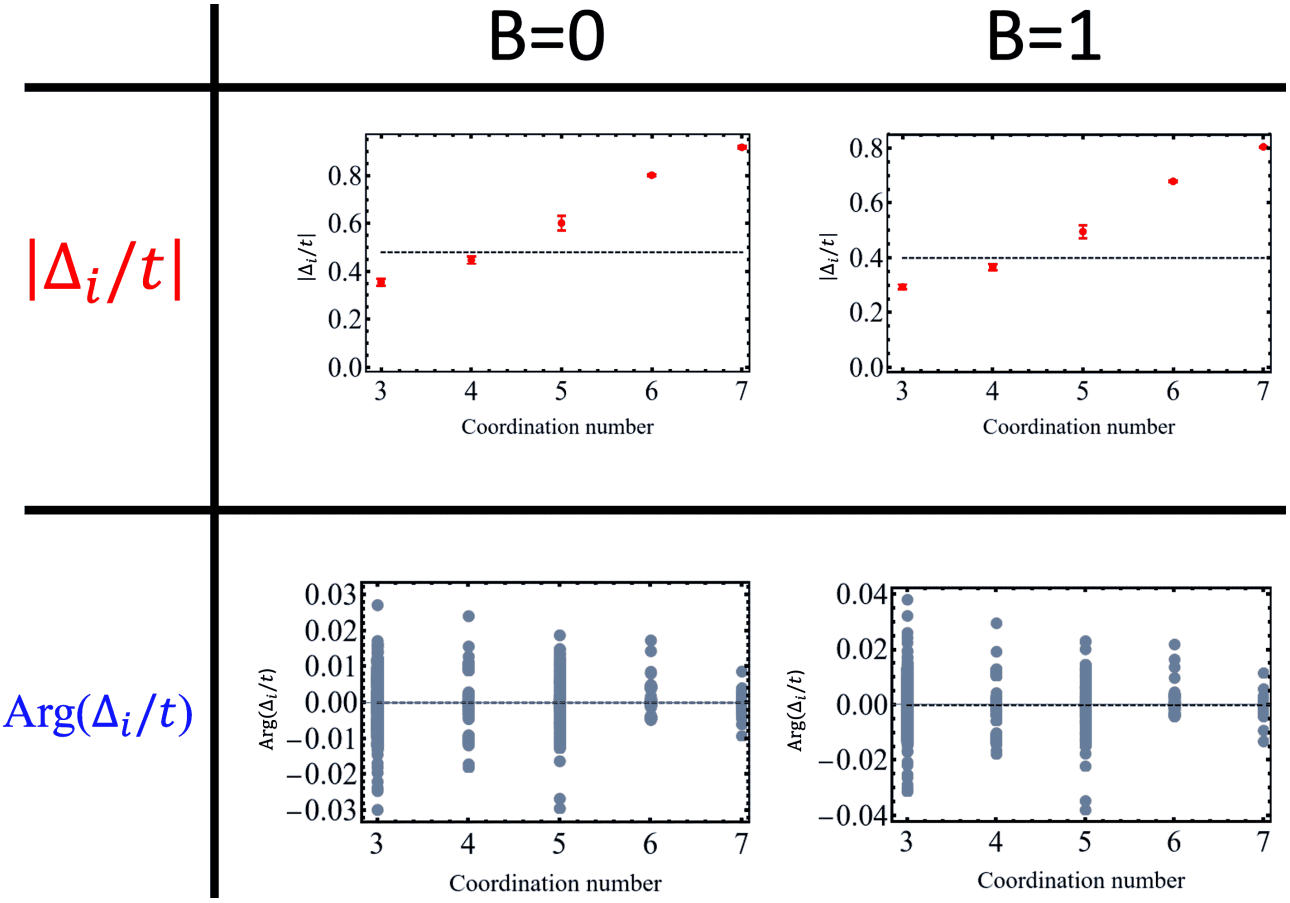

Figure 5.9: $|\Delta_i/t|$ (upper panel) and Arg (Δ_i/t) (lower panel) as a function of coordination number for the trivial ($B = 0$) and topological ($B = 1$) phase for the systems shown in Figs. 5.7 and 5.8.

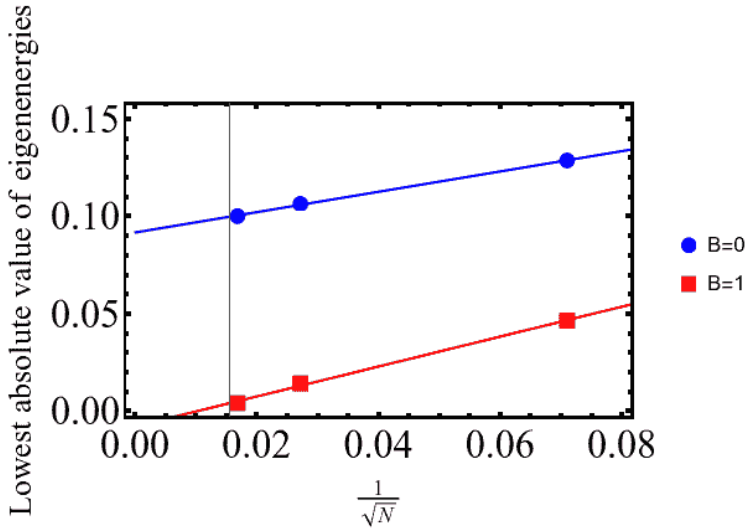

Figure 5.10: The system size dependence of the lowest absolute value of the eigenenergies in Penrose QC for the two parameter sets for $B = 0$ and 1 with the ribbon boundary condition, for $N = 199, 1364$, and 3571.

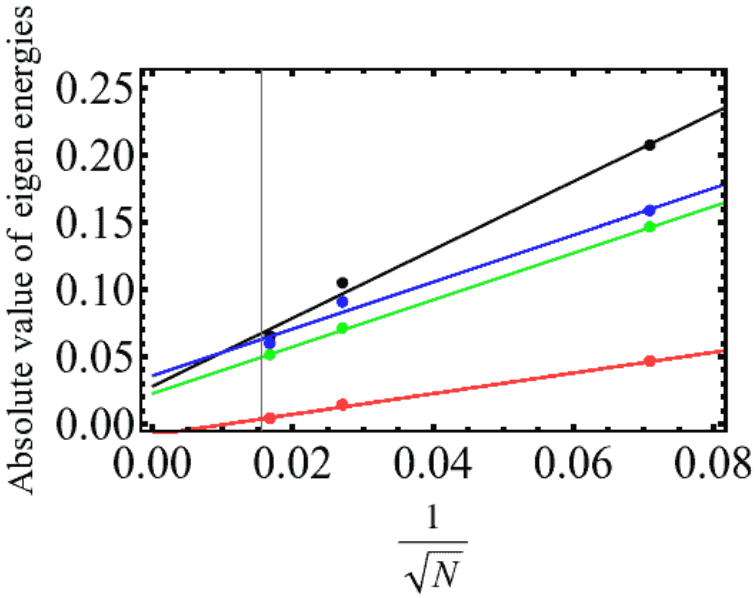

Figure 5.11: The first (red circle), second (green circle), third (blue circle), and fourth (black circle) lowest absolute value of the eigenenergies in Penrose QC as a function of $1/\sqrt{N}$ for $N = 199$, 1364, and 3571, for $B = 1$ with the ribbon boundary condition.

(black circle) lowest absolute value of the eigenenergies are plotted as a function of $1/\sqrt{N}$ for the number of lattice sites $N = 199$, 1364, and 3571, for $B = 1$ with the ribbon boundary condition. By linearly fitting these data points for different system sizes, the second, third, and fourth lowest eigenvalues are found to approach a finite (nonzero) value in the limit $N \to \infty$. It is clear from Fig. 5.11 that there is one zero-energy mode, whose energy ϵ approaches zero from the positive side in the thermodynamic limit. Consistently with the particle-hole symmetry of the BdG equations, there is another state with energy $-\epsilon$, which approaches zero from the negative side in the limit $N \to \infty$.

The (a) electron and (b) hole amplitudes (probability amplitude magnitude squared) of this zero-energy mode are shown in Fig. 5.12 for $N = 3571$ with the ribbon boundary condition and $B = 1$. Both electron and hole amplitudes are large along and near the edges and so this is clearly an edge mode. The electron and hole amplitudes are almost the same for each lattice site. They are not exactly the same due to the relatively small system size, which allows slight overlap of the wave functions of the two edge modes in the middle of the system. However, the difference between them is a decreasing function of the number of lattice sites N. This implies that the electron and hole amplitudes are the same in the

limit that $N \to \infty$, where the two edge modes do not overlap. This confirms that the two zero-energy edge modes are Majorana zero modes, one per surface, consistently with the bulk-edge correspondence and $B = 1$ as the topological invariant of the system.

5.3.2 Topological Superconductivity in Ammann-Beenker Quasicrystal

We have also solved the BdG equations self-consistently for the superconducting order parameter and Hartree potential in AB QCs with PBC. As in Penrose QC, the converged mean fields are nonzero at all sites, but vary from site to site. The magnitude of the converged order parameter Δ_i/t is presented in Fig. 5.13 for the trivial ($B = 0$) and topological ($B = 1$) phase for part of the QC around a high-symmetry point in real space (upper panel) and the perpendicular space (lower panel). The high symmetry point in the upper panel is represented by a black dot. The parameters used are $h/t = 1.0, \alpha/t = 1.0, U/t = -5.2$, and $\tilde{\mu}/t = 3.7(3.8)$ for the Bott index $B = 0(1)$. The number of lattice points of the used AB QC is 1393, and Eq. (2.28) is used for the convergence criteria. Figure 5.13 demonstrates that despite the spatial variation of the order parameter, TSC can exist stably in AB QC as well. Clearly, $|\Delta_i/t|$ has eightfold rotational symmetry whose center of rotation is the black point in Fig. 5.13 and mirror symmetry whose axes of reflection are the black dashed lines in Fig. 5.13 in both real space and the perpendicular space. The plot in the perpendicular space in Fig. 5.13 shows that the magnitude of the order parameter at a given site is mostly determined by its coordination number, i.e., the number of nearest-neighbor sites. And the higher the coordination number, the larger the $|\Delta_i|/t$.

Arg (Δ_i/t) is presented in Fig. 5.14 for the trivial ($B = 0$) and topological ($B = 1$) phase for part of the QC around the high-symmetry point (black dot) in real space (upper panel) and the perpendicular space (lower panel). Consistently with the case of Penrose QC, the converged order parameter is always complex even for a real initial guess. It can be seen that Arg (Δ_i/t) has eightfold rotational symmetry whose center of rotation is the black point in Fig. 5.14 but the mirror symmetry whose axes of reflection are the black dashed lines in Fig. 5.14 is broken in both real space and the perpendicular space.

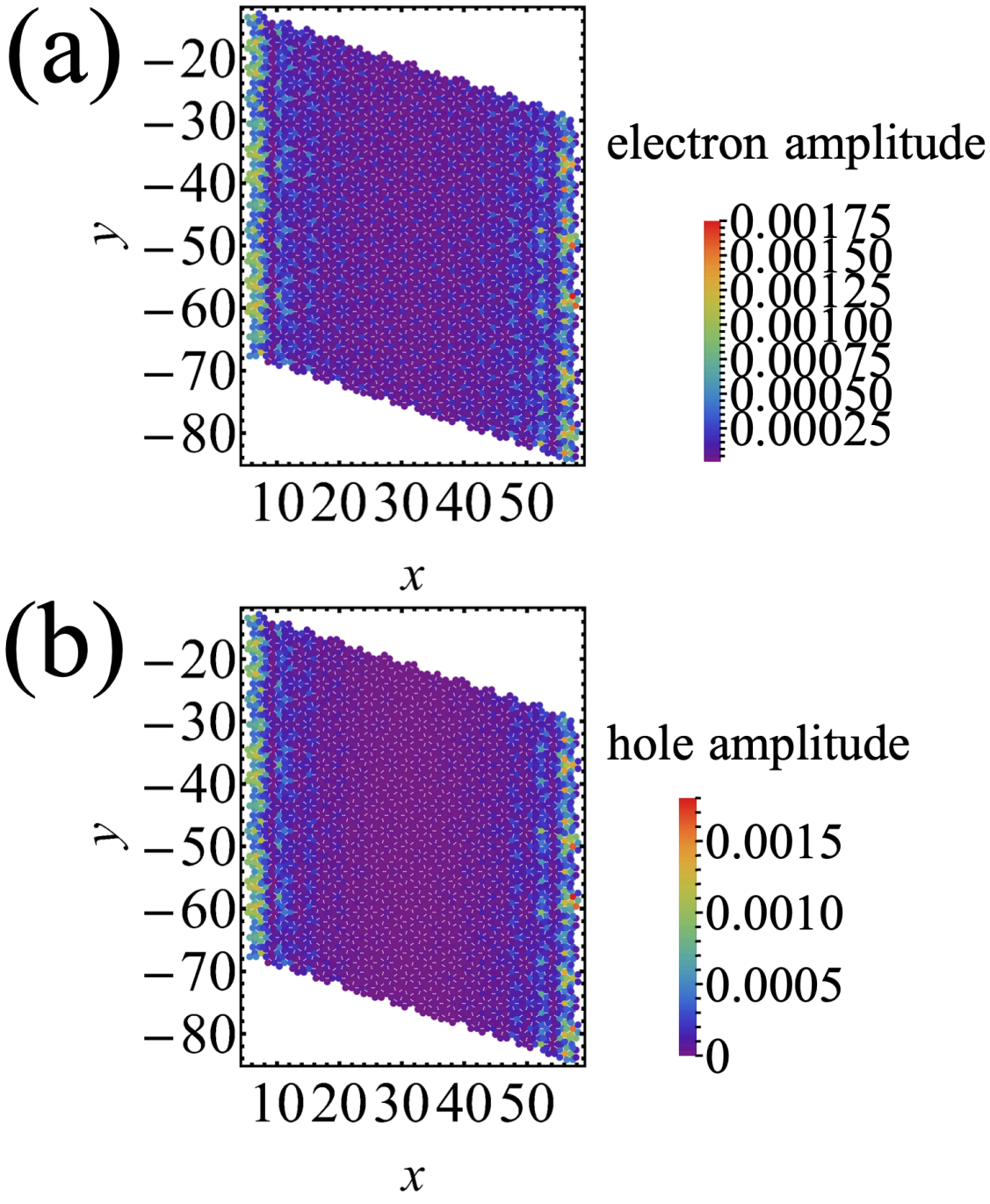

Figure 5.12: (a) Electron and (b) hole amplitudes of the lowest-energy quasiparticle excitation in the 3571-site Penrose QC with the ribbon boundary condition and $B = 1$.

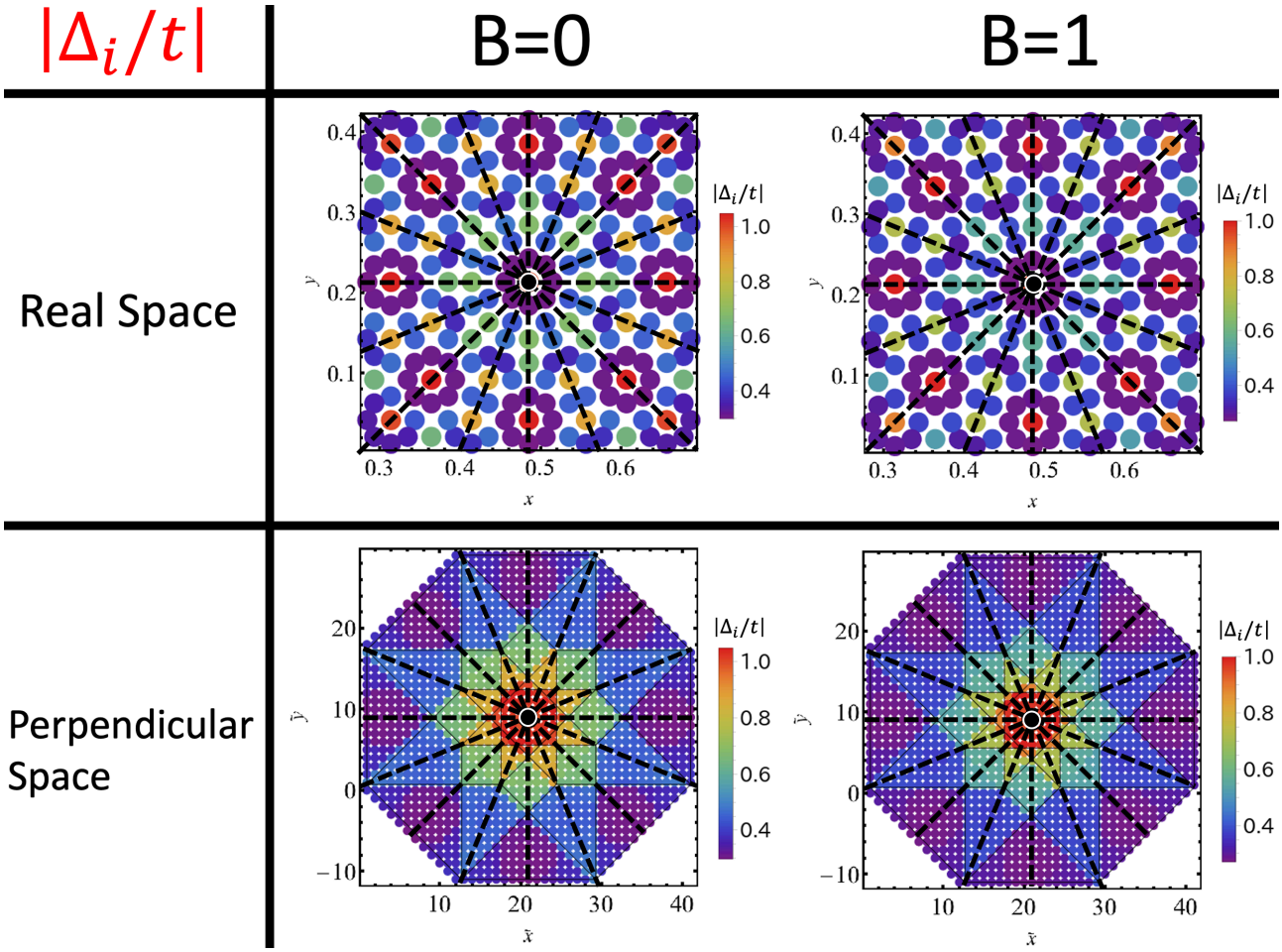

Figure 5.13: The magnitude of Δ_i/t for the trivial ($B = 0$) and topological ($B = 1$) phase in real space (upper panel) and the perpendicular space (lower panel) in AB QC. The parameters used are $h/t = 1.0, \alpha/t = 1.0, U/t = -5.2$, and $\tilde{\mu}/t = 3.7(3.8)$ for the Bott index $B = 0(1)$, and $N = 1393$.

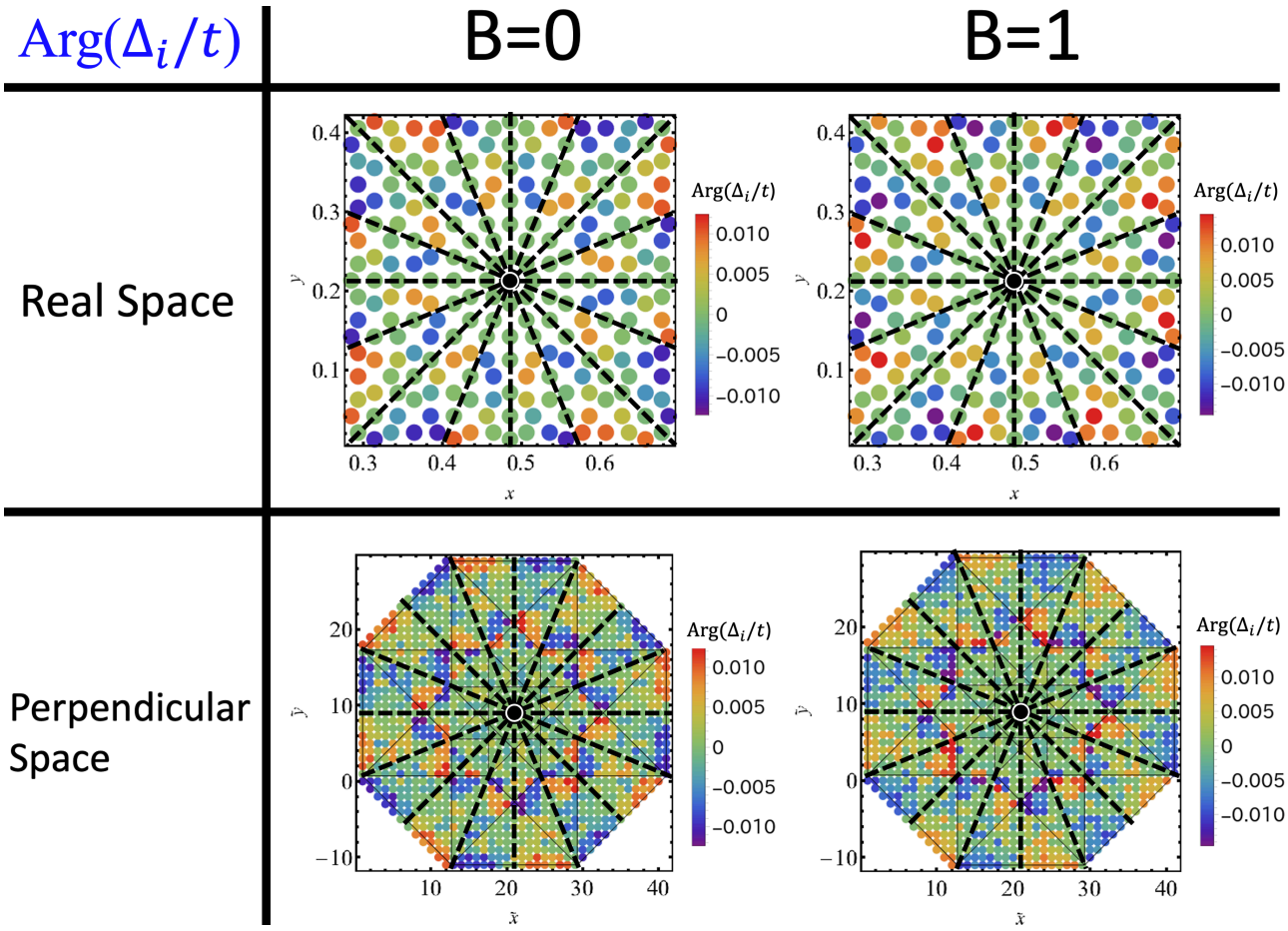

Figure 5.14: Arg (Δ_i/t) for the trivial $(B = 0)$ and topological $(B = 1)$ phase in real space (upper panel) and the perpendicular space (lower panel), for the same systems as shown in Fig. 5.13.

In Fig. 5.13, $|\Delta_i/t|$ is uniformly distributed in the given scale in each sector for a given coordination number, while there is no correlation with the coordination number in Arg (Δ_i/t) in Fig. 5.14. In Fig.5.15, $|\Delta_i/t|$ (upper panel) and Arg (Δ_i/t) (lower panel) are plotted as a function of coordination number for the trivial ($B = 0$) and topological ($B = 1$) phase. The red dots and the error bars represent, respectively, the mean value and standard deviation of $|\Delta_i/t|$ for each coordination number. The black dashed line in the upper (lower) panel represents the mean value of $|\Delta_i/t|$ (Arg (Δ_i/t)) for the entire lattice. The small standard deviation of $|\Delta_i/t|$ indicates that the value of $|\Delta_i/t|$ at any given site is mostly determined by its coordination number. The mean value of Arg (Δ_i/t) for the entire lattice is found to be almost zero, 4.0766×10^{-16} and 1.6565×10^{-16}, in the trivial ($B = 0$) and topological ($B = 1$) phase, respectively. In contrast, to the magnitude, the phase Arg(Δ_i/t) is independent of the coordination number, as can be seen in Fig.5.15. The strength of the Hartree potential for each spin is also governed by the coordination number for each lattice site (not shown).

Figures 5.13-5.15 show that with PBC, the distribution of the superconducting order parameter is not affected by the topological nature of the system, i.e., whether $B = 0$ or 1.

The lowest absolute value of the eigenenergies is plotted as a function of $1/\sqrt{N}$ in Fig. 5.16 for the two parameter sets for $B = 0$ and 1 with the ribbon boundary condition, for the number of lattice points $N = 41, 239, 1393$, and 8119. The blue circles (red squares) represent the results for $B = 0$ ($B = 1$). By linearly fitting these data points for different system sizes, the lowest eigenvalue is found to approach zero and a nonzero value, respectively, for $B = 1$ and 0, in the limit $N \to \infty$. Consistently with the case of Penrose QC, this zero-energy excitation when $B = 1$ is expected to be a Majorana zero mode per surface in the thermodynamic limit, in accordance with the bulk-edge correspondence. The electron and hole probability amplitudes (magnitude squared) of the zero-energy edge mode have indeed been confirmed to be almost identical for $N = 8119$ (not shown).

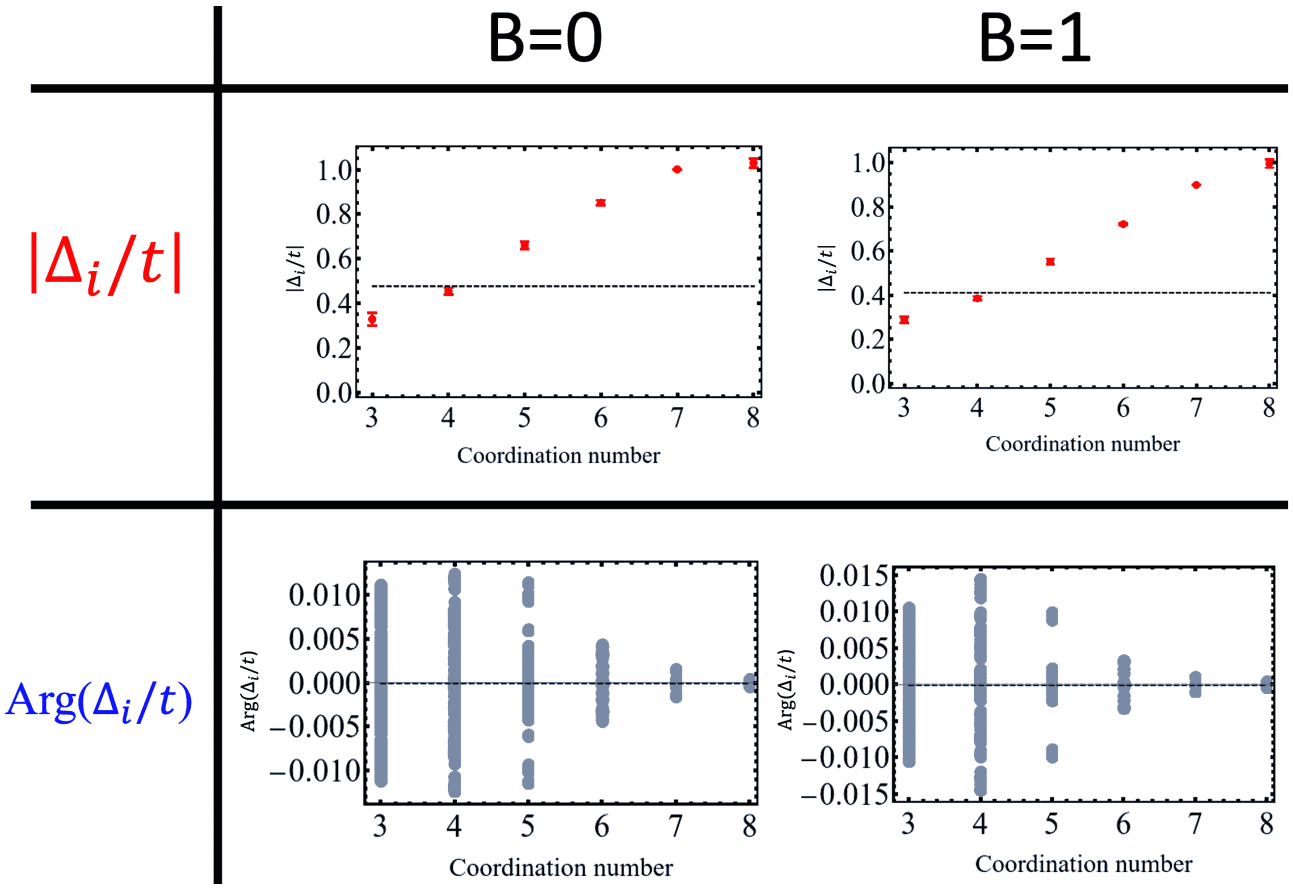

Figure 5.15: $|\Delta_i/t|$ (upper panel) and Arg (Δ_i/t) (lower panel) as a function of coordination number for the trivial $(B = 0)$ and topological $(B = 1)$ phase for the systems shown in Figs. 5.13 and 5.14.

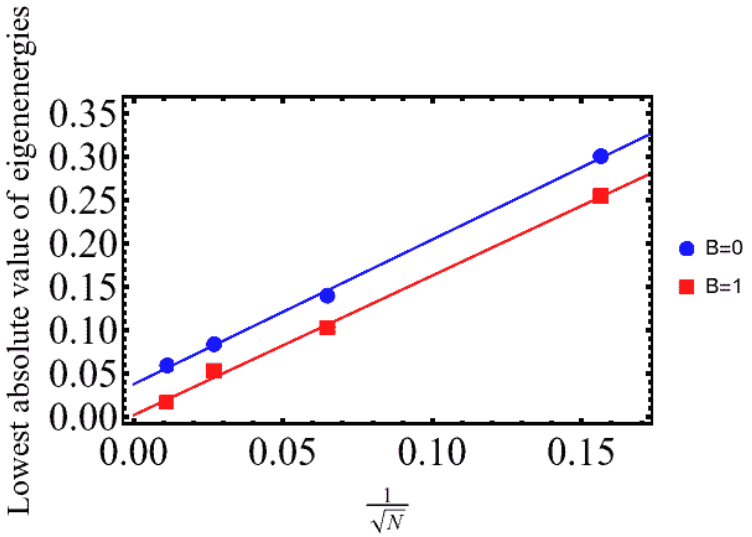

Figure 5.16: The system size dependence of the lowest absolute value of the eigenenergies in AB QC for the two parameter sets for $B = 0$ and 1 with the ribbon boundary condition for $N = 41, 239, 1393$, and 8119.

6 Conclusion

In this thesis, mean field theory has been applied to the model Hamiltonian for two-dimensional TSC with broken time-reversal symmetry, and the superconducting order parameter and spin-dependent Hartree potential have been self-consistently obtained. The TSC model [72], which was originally proposed for periodic square-lattice systems, has been generalized for quasicrystalline systems. As prototype examples, two-dimensional Penrose and AB QCs have been studied. Due to the aperiodicity of QCs, Bloch's theorem is not applicable, and the BdG equations formulated in coordinate space have been solved directly and numerically.

The self-consistently obtained superconducting order parameter has been examined for two parameter sets with different topological invariants. The used topological invariant is the Bott index B, which corresponds to the first Chern number in periodic systems. When B is zero (nonzero), the system is in a topologically trivial (nontrivial) phase. With PBC, reflecting the geometry of the QC, the absolute value of the superconducting order parameter in both real space and the perpendicular space presents fivefold and eightfold rotational symmetry, respectively, in Penrose and AB QCs, along with their inherent mirror symmetries. The distribution of the superconducting order parameter is found to be independent of the value of B. The major effect of the topology of the system manifests itself in the presence of a surface boundary. With the ribbon boundary condition, the lowest absolute value of the eigenenergies in the thermodynamic limit is estimated to be zero, whereas it approaches a finite nonzero value when $B = 0$. The zero-energy excitation in the topological phase with $B = 1$ has been shown to be a Majorana zero mode per surface, consistently with the bulk-edge correspondence.

Future work could introduce wave-vector or momentum space analysis. Due to aperiodicity, there is no Brillouin zone in momentum space. On the other hand, x-ray diffraction of

QCs clearly shows Bragg peaks, which motivate a study of TSC in QCs in momentum space. In a periodic system, a topological phase transition occurs when the energy gap vanishes at one of the high-symmetry points in the first Brillouin zone. Thus, a topological phase transition in a QC is expected to be associated with a wave vector(s) related to self-similarity of QCs. The self-similarity inherent in a QC is tied to an irrational number, which is the golden ratio and the silver ratio, respectively, in Penrose and AB QCs. Therefore, the wave vector(s) associated with a topological phase transition may be described in terms of the irrational number. It is also interesting to examine possible fractal structure in topological phase diagrams and investigate how self-similarity of a QC affects the topological nature of TSC states. Finally, the existence of a Majorana fermion in a QC with $B = 1$ can also be confirmed by introducing a vortex at the center of the system with OBC all around.

References

[1] Y. Ando. Topological Insulator Materials. *J. Phys. Soc. Jpn.*, 82:102001, 2013.

[2] Y. Ando and L. Fu. Topological Crystalline Insulators and Topological Superconductors: From Concepts to Materials. *Annu. Rev. Condens. Matter Phys.*, 6:361, 2015.

[3] M. Sato and Y. Ando. Topological superconductors: a review. *Rep. Prog. Phys.*, 80:076501, 2017.

[4] THE NOBEL PRIZE. Press release: The Nobel Prize in Physics 2016. https://www.nobelprize.org/prizes/physics/2016/press-release/.

[5] D. Hsieh, D. Qian, L. Wray, Y. Xia, Y. S. Hor, R. J. Cava, and M. Z. Hasan. A topological Dirac insulator in a quantum spin Hall phase. *Nature*, 452:970, 2008.

[6] Y. Xia, D. Qian, D. Hsieh, L. Wray, A. Pal, H. Lin, A. Bansil, D. Grauer, Y. S. Hor, R. J. Cava, and M. Z. Hasan. Observation of a large-gap topological-insulator class with a single Dirac cone on the surface. *Nat. Phys.*, 5:398, 2009.

[7] R. Yoshimi, A. Tsukazaki, Y. Kozuka, J. Falson, K. S. Takahashi, J. G. Checkelsky, N. Nagaosa, M. Kawasaki, and Y. Tokura. Quantum Hall effect on top and bottom surface states of topological insulator $(Bi_{1-x}Sb_x)_2Te_3$ films. *Nat. Commun.*, 6:6627, 2015.

[8] L. Fu, C. L. Kane, and E. J. Mele. Topological insulators in three dimensions. *Phys. Rev. Lett.*, 98:106803, 2007.

[9] Q. Niu, D. J. Thouless, and Y.-S. Wu. Quantized Hall conductance as a topological invariant. *Phys. Rev. B*, 31:3372, 1985.

[10] S. Nadj-Perge, I. K. Drozdov, J. Li, H. Chen, S. Jeon, J. Seo, A. H. MacDonald, B. A. Bernevig, and A. Yazdani. Observation of Majorana fermions in ferromagnetic atomic chains on a superconductor. *Science*, 346:602, 2014.

[11] G. C. Ménard, S. Guissart, C. Brun, R. T. Leriche, M. Trif, F. Debontridder, D. Demaille, D. Roditchev, P. Simon, and T. Cren. Two-dimensional topological superconductivity in Pb/Co/Si(111). *Nat. Commun.*, 8:2040, 2017.

[12] T. Machida, Y. Sun, S. Pyon, S. Takeda, Y. Kohsaka, T. Hanaguri, T. Sasagawa, and T. Tamegai. Zero-energy vortex bound state in the superconducting topological surface state of Fe(Se,Te). *Nat. Mater.*, 18:811, 2019.

[13] Y. Hatsugai. Chern number and edge states in the integer quantum Hall effect. *Phys. Rev. Lett.*, 71:3697, 1993.

[14] Y. Hatsugai. Edge states in the integer quantum Hall effect and the Riemann surface of the Bloch function. *Phys. Rev. B*, 48:11851, 1993.

[15] N. Read and D. Green. Paired states of fermions in two dimensions with breaking of parity and time-reversal symmetries and the fractional quantum Hall effect. *Phys. Rev. B*, 61:10267, 2000.

[16] E. Majorana. Teoria simmetrica dell'elettrone e del positrone. *Il Nuovo Cimento*, 14:171, 1937.

[17] C. Nayak, S. H. Simon, A. Stern, M. Freedman, and S. D. Sarma. Non-Abelian anyons and topological quantum computation. *Rev. Mod. Phys.*, 80:1083, 2008.

[18] A. Stern. Non-Abelian states of matter. *Nature*, 464:187, 2010.

[19] K. Asano. *Quantum Theory of Electrons in Solids*. UTP, 2019.

[20] G. Collins. Computing with quantum knots. *Sci. Am.*, 294:56, 2006.

[21] A. P. Schnyder, S. Ryu, A. Furusaki, and A. W. W. Ludwig. Classification of topological insulators and superconductors in three spatial dimensions. *Phys. Rev. B*, 78:195125, 2008.

[22] A. Furusaki. Classification of Topological Insulators and Superconductors. *J. Surf. Sci. Soc. Jpn.*, 32:209, 2011.

[23] D. J. Thouless, M. Kohmoto, M. P. Nightingale, and M. den Nijs. Quantized Hall Conductance in a Two-Dimensional Periodic Potential. *Phys. Rev. Lett.*, 49:405, 1982.

[24] S.-S. Chern. Characteristic Classes of Hermitian Manifolds. *Ann. Math.*, 47:85, 1946.

[25] H. K. Onnes. The Superconductivity of Mercury. *Commun. Phys. Lab. Univ. Leiden*, 119b, 1911.

[26] H. Fröhlich. Theory of the Superconducting State. I. The Ground State at the Absolute Zero of Temperature. *Phys. Rev.*, 79:845, 1950.

[27] L. N. Cooper. Bound Electron Pairs in a Degenerate Fermi Gas. *Phys. Rev.*, 104:1189, 1956.

[28] N. N. Bogoliubov. On a new method in the theory of superconductivity. *Il Nuovo Cimento*, 7:794, 1958.

[29] J. G. Valatin. Comments on the Theory of Superconductivity. *Il Nuovo Cimento*, 7:843, 1958.

[30] G. M. Eliashberg. Interactions between electrons and lattice vibrations in a superconductor. *Sov. Phys. JETP*, 11:696, 1960.

[31] D. J. Thouless. Perturbation theory in statistical mechanics and the theory of superconductivity. *Ann. Phys.*, 10:553, 1960.

[32] J. Bardeen, L. N. Cooper, and J. R. Schrieffer. Theory of superconductivity. *Phys. Rev.*, 108:1175, 1957.

[33] E. C. Stoner. Collective electron ferromagnetism. *Proc. R. Soc. Lond. A*, 165:372, 1938.

[34] J. Kanamori. Electron Correlation and Ferromagnetism of Transition Metals. *Prog. Theor. Phys.*, 30:275, 1963.

[35] T. Moriya and A. Kawabata. Effect of Spin Fluctuations on Itinerant Electron Ferromagnetism. *J. Phys. Soc. Jpn.*, 34:639, 1973.

[36] P. W. Anderson. Plasmons, Gauge Invariance, and Mass. *Phys. Rev.*, 130:439, 1963.

[37] P. W. Higgs. Broken Symmetries and the Masses of Gauge Bosons. *Phys. Rev. Lett.*, 13:508, 1964.

[38] P. W. Higgs. Broken symmetries, massless particles and gauge fields. *Phys. Lett.*, 12:132, 1964.

[39] Y. Nambu. Quasi-Particles and Gauge Invariance in the Theory of Superconductivity. *Phys. Rev.*, 117:648, 1960.

[40] J. Goldstone. Field theories with $\langle\langle$ Superconductor $\rangle\rangle$ solutions. *Il Nuovo Cimento*, 19:154, 1961.

[41] F. Bloch. Zur Theorie des Ferromagnetismus. *Z. Phys.*, 61:206, 1930.

[42] T. Izuyama, D.-J. Kim, and R. Kubo. Band Theoretical Interpretation of Neutron Diffraction Phenomena in Ferromagnetic Metals. *J. Phys. Soc. Jpn.*, 18:1025, 1963.

[43] V. B. Michael. Quantal phase factors accompanying adiabatic changes. *Proc. R. Soc. Lond. A*, 392:45, 1984.

[44] F. Bloch. Über die Quantenmechanik der Elektronen in Kristallgittern. *Z. Phys.*, 52:555, 1929.

[45] D. Shechtman, I. Blech, D. Gratias, and J. W. Cahn. Metallic Phase with Long-Range Orientational Order and No Translational Symmetry. *Phys. Rev. Lett.*, 53:1951, 1984.

[46] D. Levine and P. J. Steinhardt. Quasicrystals: A New Class of Ordered Structures. *Phys. Rev. Lett.*, 53:2477, 1984.

[47] K. Nagao, T. Inuzuka, K. Nishimoto, and K. Edagawa. Experimental Observation of Quasicrystal Growth. *Phys. Rev. Lett.*, 115:075501, 2015.

[48] T. Dotera, S. Bekku, and P. Ziherl. Bronze-mean hexagonal quasicrystal. *Nat. Mater.*, 16:987, 2017.

[49] K. Kamiya, T. Takeuchi, N. Kabeya, N. Wada, T. Ishimasa, A. Ochiai, K. Deguchi, K. Imura, and N. K. Sato. Discovery of superconductivity in quasicrystal. *Nat. Commun.*, 9:154, 2018.

[50] S. Yoshida, S. Suzuki, T. Yamada, T. Fujii, A. Ishikawa, and R. Tamura. Antiferromagnetic order survives in the higher-order quasicrystal approximant. *Phys. Rev. B*, 100:180409, 2019.

[51] R. Tamura, A. Ishikawa, S. Suzuki, T. Kotajima, Y. Tanaka, T. Seki, N. Shibata, T. Yamada, T. Fujii, C.-W. Wang, M. Avdeev, K. Nawa, D. Okuyama, and T. J. Sato. Experimental Observation of Long-Range Magnetic Order in Icosahedral Quasicrystals. *J. Am. Chem. Soc.*, 143:19938, 2021.

[52] L. Chang, F. Erina, K. Yukari, I. Yuki, I. Asuka, T. Ryuji, K. Kaoru, and Y. Ryo. Machine Learning to Predict Quasicrystals from Chemical Compositions. *Adv. Mater.*, 33:2102507, 2021.

[53] J. N. Lalena. From Quartz to Quasicrystals: Probing Nature's Geometric Patterns in Crystalline Substances. *Crystallogr. Rev.*, 12:125, 2006.

[54] A. Yamamoto. Crystallography of Quasiperiodic Crystals. *Acta Crystallogr. A*, A52:509, 1996.

[55] W. Steurer. Quasicrystals: What do we know? What do we want to know? What can we know? *Acta Crystallogr. A*, 74:1, 2018.

[56] THE NOBEL PRIZE. The Nobel Prize in Chemistry 2011. https://www.nobelprize.org/prizes/chemistry/2011/summary/.

[57] C. Janot. The Properties and Applications of Quasicrystals. *Europhys. News*, 27:60, 1996.

[58] P. Archambault and C. Janot. Thermal Conductivity of Quasicrystals and Associated Processes. *MRS Bulletin*, 22:48, 1997.

[59] T. P. Yadav and N. K. Mukhopadhyay. Quasicrystal: a low-frictional novel material. *Curr. Opin. Chem. Eng.*, 19:163, 2018.

[60] D. A. Rabson. Toward theories of friction and adhesion on quasicrystals. *Prog. Surf. Sci.*, 87:253, 2012.

[61] B. Persson. *Contact Mechanics, Friction and Adhesion with Application to Quasicrystals. In: E. Gnecco, E. Meyer Fundamentals of Friction and Wear on the Nanoscale.* Springer, 2015.

[62] Sputtering technique forms versatile quasicrystalline coatings. *MRS Bulletin*, 36:581, 2011.

[63] J. E. Graebner and H. S. Chen. Specific Heat of an Icosahedral Superconductor, $Mg_3Zn_3Al_2$. *Phys. Rev. Lett.*, 58:1945, 1987.

[64] S. Sakai, N. Takemori, A. Koga, and R. Arita. Superconductivity on a quasiperiodic lattice: Extended-to-localized crossover of Cooper pairs. *Phys. Rev. B*, 95:024509, 2017.

[65] S. Sakai and R. Arita. Exotic pairing state in quasicrystalline superconductors under a magnetic field. *Phys. Rev. Res.*, 1:022002, 2019.

[66] R. N. Araújo and E. C. Andrade. Conventional superconductivity in quasicrystals. *Phys. Rev. B*, 100:014510, 2019.

[67] R. Ghadimi, T. Sugimoto, and T. Tohyama. Majorana Zero-Energy Mode and Fractal Structure in Fibonacci-Kitaev Chain. *J. Phys. Soc. Jpn.*, 86:114707, 2017.

[68] R. Ghadimi, T. Sugimoto, K. Tanaka, and T. Tohyama. Topological superconductivity in quasicrystals. *Phys. Rev. B*, 104:144511, 2021.

[69] T. A. Loring and M. B. Hastings. Disordered topological insulators via C^*-algebras. *Europhys. Lett.*, 92:67004, 2010.

[70] T. A. Loring. Bulk spectrum and K-theory for infinite-area topological quasicrystals. *J. Math. Phys.*, 60:081903, 2019.

[71] P. G. de Gennes. *Superconductivity of Metals and Alloys*. W. A. Benjamin, 1966.

[72] M. Sato, Y. Takahashi, and S. Fujimoto. Non-Abelian topological orders and Majorana fermions in spin-singlet superconductors. *Phys. Rev. B*, 82:134521, 2010.

[73] E. D. B. Smith, K. Tanaka, and Y. Nagai. Manifestation of chirality in the vortex lattice in a two-dimensional topological superconductor. *Phys. Rev. B*, 94:064515, 2016.

[74] S. L. Goertzen, K. Tanaka, and Y. Nagai. Self-consistent study of Abelian and non-Abelian order in a two-dimensional topological superconductor. *Phys. Rev. B*, 95:064509, 2017.

[75] THE NOBEL PRIZE. The Nobel Prize in Physics 1972. https://www.nobelprize.org/prizes/physics/1972/summary/.

[76] L. D. Landau. Theory of a Fermi-Liquids. *Sov. Phys. JETP*, 3:920, 1956.

[77] L. D. Landau. Oscillations in a Fermi-Liquid. *Sov. Phys. JETP*, 5:101, 1957.

[78] J. R. Schrieffer. *Theory of Superconductivity*. Westview Press, 1999.

[79] R. Meservey and B. B. Schwartz. *Equilibrium Properties: Comparison of Experimental Results with Predictions of the BCS Theory, Chapter 3 in Superconductivity (edited by R. D. Parks)*. CRC Press, 1969.

[80] National Astronomical Observatory of Japan. *Chronological Scientific Tables*. MARUZEN-YUSHODO Co., Ltd., 2021.

[81] T. Ando, Y. Matsumoto, and Y. Uemura. Theory of Hall Effect in a Two-Dimensional Electron System. *J. Phys. Soc. Jpn.*, 39(2):279, 1975.

[82] L. Smřka and P. Středa. Transport coefficients in strong magnetic fields. *J. Phys. C*, 10:2153, 1977.

[83] K. von Klitzing, G. Dorda, and M. Pepper. New Method for High-Accuracy Determination of the Fine-Structure Constant Based on Quantized Hall Resistance. *Phys. Rev. Lett.*, 45:494, 1980.

[84] H. Aoki and T. Ando. Effect of localization on the hall conductivity in the two-dimensional system in strong magnetic fields. *Solid State Commun.*, 38(11):1079, 1981.

[85] A. Widom. Thermodynamic derivation of the Hall effect current. *Phys. Lett. A*, 90(9):474, 1982.

[86] F. D. M. Haldane. Model for a Quantum Hall Effect without Landau Levels: Condensed-Matter Realization of the "Parity Anomaly". *Phys. Rev. Lett.*, 61:2015, 1988.

[87] A. Y. Kitaev. Unpaired Majorana fermions in quantum wires. *Phys. Usp.*, 44:131, 2001.

[88] P. A. M. Dirac. Quantised singularities in the electromagnetic field. *Proc. R. Soc. Lond. A*, 133:60, 1931.

[89] T. Fukui, Y. Hatsugai, and H. Suzuki. Chern Numbers in Discretized Brillouin Zone: Efficient Method of Computing (Spin) Hall Conductances. *J. Phys. Soc. Jpn.*, 74:1674, 2005.

[90] R. Penrose. The role of aesthetics in pure and applied mathematical research. *Bull. Inst. Math. Appl.*, 10:266, 1974.

[91] N. G. de Brujin. Algebraic theory of Penrose's non-periodic tilings of the plane. I. *Indag. Math.*, 84:39, 1981.

[92] H. Tsunetsugu, T. Fujiwara, K. Ueda, and T. Tokihiro. Electronic properties of the Penrose lattice. I. Energy spectrum and wave functions. *Phys. Rev. B*, 43:8879, 1991.

[93] F. V. Babalievski. Percolation conductivity of Penrose lattices by the transfer-matrix Monte Carlo method. *J. Non-Cryst. Solids*, 153:370, 1993.

[94] E. S. Zijlstra and T. Janssen. Non-spiky density of states of an icosahedral quasicrystal. *Europhys. Lett.*, 52:578, 2000.

[95] T. Rieth and M. Schreiber. Identification of spatially confined states in two-dimensional quasiperiodic lattices. *Phys. Rev. B*, 51:15827, 1995.

[96] M. Arai, T. Tokihiro, T. Fujiwara, and M. Kohmoto. Strictly localized states on a two-dimensional Penrose lattice. *Phys. Rev. B*, 38:1621, 1988.

[97] M. Kohmoto and B. Sutherland. Electronic and vibrational modes on a Penrose lattice: Localized states and band structure. *Phys. Rev. B*, 34:3849, 1986.

[98] A. Koga and H. Tsunetsugu. Antiferromagnetic order in the Hubbard model on the Penrose lattice. *Phys. Rev. B*, 96:214402, 2017.

[99] F. P. M. Beenker. *Algebraic theory of non-periodic tilings of the plane by two simple building blocks : a square and a rhombus*. TU/e, 1982.

[100] B. Grünbaum and G. C. Shephard. *Tilings and Patterns*. W. H. Freeman & Co., 1986.

[101] M. Duneau. Approximants of quasiperiodic structures generated by the inflation mapping. *J. Phys. A*, 22:4549, 1989.

[102] K. Deguchi, M. Nakayama, S. Matsukawa, K. Imura, K. Tanaka, T. Ishimasa, and N. K. Sato. Superconductivity of Au-Ge-Yb Approximants with Tsai-Type Clusters. *J. Phys. Soc. Jpn.*, 84:023705, 2015.

[103] M. Sato and S. Fujimoto. Topological phases of noncentrosymmetric superconductors: Edge states, Majorana fermions, and non-Abelian statistics. *Phys. Rev. B*, 79:094504, 2009.

[104] S. Tewari, J. D. Sau, and S. D. Sarma. A theorem for the existence of Majorana fermion modes in spin-orbit-coupled semiconductors. *Ann. Phys.*, 325:219, 2010.

[105] V. L. Howse. Properties of the Vortex Lattice of an Abelian Topological Superconductor. *Master's thesis, University of Saskatchewan*, 2021.

[106] Y. F. Zhang, Y.Y. Yang, Y. Ju, L. Sheng, R. Shen, D. N. Sheng, and D. Y. Xing. Coupling-matrix approach to the Chern number calculation in disordered systems. *Chin. Phys. B*, 22:117312, 2013.

[107] R. Bianco and R. Resta. Mapping topological order in coordinate space. *Phys. Rev. B*, 84:241106, 2011.

[108] M. B. Hastings and T. A. Loring. Almost commuting matrices, localized Wannier functions, and the quantum Hall effect. *J. Math. Phys.*, 51:015214, 2010.